Characterisation of organic fuel tracers for laser-based quantitative diagnostics of fuel concentration, temperature, and equivalence ratio in practical combustion processes

Von der Fakultät für Ingenieurwissenschaften, Abteilung Maschinenbau und Verfahrenstechnik der

Universität Duisburg-Essen

zur Erlangung des akademischen Grades

eines

Doktors der Ingenieurwissenschaften

Dr.-Ing.

genehmigte Dissertation

von

Stephan Martin Faust

aus

Köln

Gutachter: Univ.-Prof. Dr. rer. nat. Christof Schulz
Univ.-Prof. Dr. rer. nat. Volker Sick
Tag der mündlichen Prüfung: 29.4.2013

Summary

In the present work the fluorescence properties of commonly used fluorescence tracers for laser-induced fluorescence (LIF) applications in the gas phase are investigated as a function of temperature, pressure, and bath gas composition. Such data provide valuable information for quantitative LIF diagnostics in practical systems like gas flows, e.g., in internal combustion (IC) engines. For this purpose a high-pressure high-temperature cell was built to reach temperatures from room temperature up to 1400 K and pressures ranging from 1 to 10 bar for varying bath gas compositions. This range of conditions is of utmost importance for in-cylinder IC engine diagnostics as well as gas flow mixing.

In this thesis fluorescence lifetimes and spectra of toluene and naphthalene were recorded experimentally. These species are typical representatives of aromatic tracers. In the experiment, temperature ranged from 296–1200 K and pressure from 1 to 10 bar with varying buffer gases of N_2, air, and CO_2. A novel aromatic species, so far not investigated in detail as a tracer substance, is anisole. It is a promising alternative delivering up to 100 times stronger signals compared to toluene under otherwise identical conditions (i.e., temperature, pressure, bath gas composition). Thus, anisole fluorescence spectra and lifetimes were recorded in the 296–1000 K range with pressure ranging from 1–10 bar in N_2 as bath gas. Systematic investigations of collisional quenching by O_2 for all three mentioned aromatics complete the study. The temperature dependence of the fluorescence lifetimes of acetone and 3-pentanone as representatives of the ketone tracer group were investigated. For all investigated aromatic tracers existing (toluene) phenomenological fluorescence models were expanded or new ones developed (naphthalene, anisole).

Due to the high achievable temperatures in the measurement cell, investigations of the pyrolysis of the used tracer species were also performed. In addition to the expected loss of the tracer signal fluorescing spectra originating from pyrolysis products were observed. These in-situ formed species may lead to new diagnostics strategies.

For demonstration purposes the investigated aromatic tracers were used in a LIF imaging experiment in a housed fuel injector. The performance of the respective tracer species with respect to the achievable signal-to-noise ratios and signal intensity per molecule is discussed.

Zusammenfassung

In der vorliegenden Dissertation wurden die Gasphasen-Fluoreszenzeigenschaften von häufig verwendeten Tracer-Molekülen für Laser-induzierte Fluoreszenz (LIF) als Funktion von Temperatur, Druck und Stoßgaszusammensetzung untersucht. Diese Daten sind unerlässlich für quantitative LIF-Messungen zur Untersuchung von Gasphasen-Mischungsprozessen, beispielsweise in Verbrennungsmotoren. Dazu wurde eine Hochdruck-Hochtemperatur-Zelle aufgebaut für Experimente im Temperaturbereich von Raumtemperatur bis 1400 K bei Drücken von 1–10 bar und variabler Stoßgaszusammensetzung. Diese Messbedingungen sind von höchster Wichtigkeit für Diagnostik in Verbrennungsmotoren und Gasmischprozessen.

In dieser Arbeit wurden Fluoreszenzlebensdauern und -spektren der häufig verwendeten Tracer-Spezies Toluol und Naphthalin als Vertreter der aromatischen Tracer im Bereich 296–1200 K bei Drücken von 1–10 bar für N_2, Luft und CO_2 als Stoßgas untersucht. Eine systematische Untersuchung der Stoßlöschung (Quenching) der Fluoreszenz von aromatischen Tracern durch O_2 vervollständigt das Bild. Bisher eher selten als Tracer eingesetzt, ist Anisol eine verheißungsvolle Alternative, die in typischen Systemen ein bis zu 100fach stärkeres Signal als Toluol liefern kann. Daher wurden von Anisol Fluoreszenzspektren und -lebensdauern bei Temperaturen von 296–1000 K bei 1–10 bar in N_2 und der Stoßlösch-Einfluss von O_2 bei 1 bar Gesamtdruck untersucht. Für die häufig verwendeten ketonischen Tracer Aceton und 3-Pentanon wurden Fluoreszenz-Lebensdauern in Abhängigkeit von der Temperatur bestimmt. Für alle hier untersuchten aromatischen Tracer wurden vorhandene (Toluol) phänomenologische Modelle erweitert bzw. neue entwickelt (Naphthalin, Anisol).

Durch die hohen erreichbaren Temperaturen in der Messzelle konnten an den untersuchten Tracern Messungen zu deren Pyrolyseverhalten durchgeführt werden. Neben dem erwarteten Verschwinden des Fluoreszenzsignals der ursprünglichen Tracer konnten fluoreszierende Pyrolyse-Produkte beobachtet werden. Diese in-situ gebildeten Spezies eröffnen möglicherweise neue diagnostische Möglichkeiten.

Die untersuchten aromatischen Tracer wurden zu Demonstrationsmessungen in einem Experiment mit einer Kraftstoff-Einspritzdüse eingesetzt. Eine Diskussion über die Anwendbarkeit der jeweiligen Tracer-Substanz in Bezug auf das zu erreichendes Signal-Rausch-Verhältnis und die Signalintensität pro Molekül rundet diese Arbeit ab.

Table of Contents

1. Introduction

In the last decade the reduction of fuel consumption and pollutant emission of combustors in general and internal combustion engines in particular has become a key task due to the limited resources of oil and coal and an increasingly polluted environment. Alternatives like solar or wind energy are often less widespread, of lower efficiency, and will need new concepts to ensure a reliable energy supply. Electric cars are still a niche product and far away from mass production. Additionally, the pollutant emission will only truly be reduced when electricity is generated from regenerative energy sources. Thus, it is of great importance to optimise existing combustion technologies as a transitory technology until alternative regenerative sources are abundant and ready for use.

The combustion process can be subdivided into mixture formation, ignition, and the following autonomous combustion with energy release. One main part of optimising combustion performance in the respective facility depends on the detailed knowledge of the mixture formation prior to ignition. Homogeneous mixing improves combustion efficiency and reduces pollutant emission. Quantitative information about the main parameters in mixture formation such as fuel/air-ratio, temperature, and fuel distribution is thus crucial for a better understanding and effective optimisation of combustion.

Many different diagnostics techniques have been developed for the analysis of mixing and combustion processes. Optical measurement techniques have the advantage that information can be obtained without disturbing the system by avoiding intrusive probes or surfaces. Rather simple absorption strategies [1] as well as complicated multi-wavelength arrangements like CARS [2] have been developed, some of these will be discussed in section 2.3.3. During the last decades laser-induced fluorescence (LIF) has become an established measurement technique in combustion and mixing diagnostics [3-4]. Its great advantage is its high sensitivity for species detection, the easy realisation of two-dimensional imaging with high signal intensities, and the high temporal resolution if pulsed laser sources are used [5-7]. While the necessary laser and detection equipment becomes more and more compact, diagnostics are possible even in mobile and industrial devices.

Commercial fuels like gasoline, Diesel, or kerosene usually contain a large number of species that fluoresce upon excitation with UV light. Each component in the mixture exhibits specific fluorescence response depending on environmental parameters like temperature, pressure, or fuel/air ratio. Therefore, the fluorescence signal cannot easily be quantified for, e.g., temperature or concentration values. As detailed knowledge of the composition is usually not available and depends on not-controllable parameters like oil source, refinery, and production company, LIF measurements of commercial fuels are in most cases not suitable for the quantitative optimisation of combustors [7-8]. Qualitative

or semi-quantitative measurement strategies, however, have been developed and demonstrated [9-12].

For quantitative analysis of, e.g., gas-phase mixing or mixture formation prior to ignition, a single fluorescent species (a so-called tracer) added to a non-fluorescing carrier phase under study is preferred to make visible its presence in the probe volume or provide quantitative information on, e.g., temperature or concentration. Therefore, a detailed knowledge of the fluorescence properties of the tracers in the environment of interest is essential. Parameters of most importance are temperature, pressure, and bath gas composition, the latter one is a measure of the fuel/air ratio.

Among alternatives like inorganic molecules (e.g., NO, SO_2) organic species have become a popular tracer group for imaging applications in, e.g., gaseous flows or IC engines during the compression stroke. Among them, the most common subgroups are aromatics and ketones. Aromatics – typical representatives are toluene and naphthalene – are often chosen because of their chemical similarity to commercial fuels, their high fluorescence quantum yield and the strong dependence of the LIF signal intensity on oxygen concentration. On the other hand ketones – typical representatives are acetone and 3-pentanone – are often preferred because of their fluorescence emission in the visible spectral region, their insensitivity with respect to oxygen quenching and their non-toxicity [7]. Section 2.2 details typical tracers and their corresponding photophysical properties.

In numerous studies the (relative) fluorescence quantum yield, ϕ, of typical tracer species was determined depending on temperature, pressure, and bath gas composition (cf., chapter 2). Nevertheless, there still remain unexplored regions in the parameter space of interest, especially at simultaneously elevated temperatures and pressures.

Instead of quantifying fluorescence intensities, an alternative, less common approach is the measurement of the effective fluorescence lifetime, τ_{eff},. As detailed in chapter 3 a relative value for ϕ can easily be derived from τ_{eff}. Geometrical parameters, detection efficiency and variations in the absorption cross section – parameters determining the fluorescence intensity – do not influence τ_{eff}. Furthermore, τ_{eff} does not depend on the incident laser light intensity and on the tracer number density if the limits of the linear regime are not exceeded. Thus measuring τ_{eff} is a way to determine relative fluorescence quantum yields with reduced calibration effort [13-14].

Aromatic species have become often used tracer species by many research groups for the last decade (e.g., [15-24]). The conventional candidates toluene and naphthalene, however, have not been chosen based on an exhaustive screening, but on experimental experience or available data base in literature. Depending on the measurement situation it makes sense to select other candidates with improved properties like anisole, as outlined below. In this thesis toluene, naphthalene, and anisole are investigated in more detail. Toluene is a popular tracer for internal combustion engines, since its evaporation char-

acteristics fit comparably well to those of gasoline. Naphthalene is often used as tracer for Diesel fuels or kerosene, and the last can be considered as a novel tracer being between toluene and naphthalene with interesting diagnostic potential.

This thesis is structured as follows: First the concept of tracer LIF is outlined with a detailed presentation of the photophysics of often used tracer species. Then typical diagnostics strategies are shown, not only for tracer LIF, but also for comparison some selected other techniques (chapter 2). Chapter 3 introduces the photophysical background of organic tracer species together with fluorescence model concepts. The design of the measurements cell and its characteristics are shown in chapter 4. Experimental results are presented in chapter 5. For each aromatic tracer the fluorescence properties like spectra and lifetimes are given as a function of temperature, pressure, and bath gas composition. Additionally, for completeness some lifetime measurements of acetone and 3-pentanone are presented. Existing fluorescence models are tested for consistency. Phenomenological model functions are introduced to mirror the dependences of the fluorescence lifetime on environmental conditions where models are not available or still fail. For each tracer investigations of the tracer stability at high temperatures are shown and possible pyrolysis pathways are discussed. The presentation of a practical application in an optical accessible IC engine and a discussion about the applicability of each tracer concludes this chapter. The thesis closes with conclusion and an outlook in chapter 6.

2. Background

2.1 Motivation

As outlined in chapter 1, optimisation of combustion processes is crucial in the near future. The exact control of the mixture formation prior to ignition is one key step for this optimisation. New concepts in, e.g., internal combustion (IC) engines like gasoline direct injection, high boost pressures, and downsizing require detailed knowledge about the in-cylinder mixing processes and the local temperature to avoid fuel-rich pockets (leading to enhanced pollutant formation) or temperature variations that lead to uncontrolled knocking. Optical diagnostics techniques play an important role in monitoring these processes because they are non-intrusive. Measurements in typical single-cylinder lab-scale optical engines as well as in close-to-production engines with endoscopic access deliver a wealth of information for engine optimisation. In addition to in-cylinder absorption (e.g., [1] and references therein), light scattering (e.g., [25-26]), or chemiluminescence (e.g., [27]) measurements, laser-induced fluorescence (LIF) imaging measurements have become established. The great advantage of LIF is the selectivity for certain substances by choosing specific excitation and detection wavelengths (wavelength ranges), leading to improved selectivity. Reliable reference data under engine-related conditions like (simultaneously) high pressure and high temperature is essential for quantification of signal intensities.

Besides diagnostics in IC engines, optical diagnostics techniques are also used to analyse, e.g., gas turbine combustors or cold gas flows. Though the devices under test are different, the range of environmental conditions is comparable, i.e., diagnostics strategies can be adapted in both directions. Again, high-quality reference data are necessary for the quantitative interpretation of measurements. In the beginning of optical in-cylinder and gas-flow diagnostics assumption or extrapolations from atmospheric-pressure, room-temperature conditions have often been used, leading to inaccurate results under engine-related conditions. Although in the meantime many studies have begun to close the data gap for the high-pressure, high-temperature regime, there is still need for additional reference data. This thesis will deliver – amongst others – a new puzzle piece in the map of reference data for fluorescence measurements.

Fluorescence is the process of absorption and the subsequent emission of a photon, usually with a fluorescence lifetime on the 0.1–150 ns timescale. This means, turbulent flow structures can be resolved, if pulsed light sources or gated detectors are used. If (pulsed) lasers are used as excitation source the resulting diagnostics technique is called laser-induced fluorescence (LIF). Two key quantities determine the LIF signal: On the one hand the absorption cross section, which is a probability of absorbing a photon by the molecule of interest. On the other hand the fluorescence quantum yield, which is the

fraction of the number of absorbed and the number of emitted photons in an ensemble of molecules. Roughly spoken, the higher both quantities are, the higher the LIF signal is.

Regarding the LIF equation (eq. 1, [28]) the detected LIF signal I_{LIF} depends on a number of parameters. While the detection efficiency η and the collection solid angle Ω are constants throughout the measurements with the same setup, and thus can easily be calibrated, the other parameters may change during the measurement and must be detected (laser energy, I_{Laser}), calculated from deployed substances (number density of fluorescing molecules, n), or need to be known from literature (absorption cross section, σ, and fluorescence quantum yield, ϕ) for each measured LIF intensity.

$$I_{LIF} = I_{Laser} \cdot n \cdot \sigma(\lambda, T) \cdot \phi(\lambda, T, p, p_{O_2}) \cdot \Omega\eta \tag{1}$$

The variation of σ of the absorbing species with temperature for typical laser wavelengths is often known from literature for many fluorescing molecules. Before practical application, the signal dependence on the environmental parameters of interest must be derived from calibration measurements under well-controlled conditions, realised, e.g., in high-pressure or high-temperature cells [7]. When the dependences on environmental conditions are known from these measurements, diagnostics strategies can be developed where the measured signal intensity leads to the desired quantity. In section 2.3 several typical diagnostics strategies are outlined. Beyond this purely application-oriented aspect of determining fluorescence properties in cell measurements, such data can be used for a deeper insight into the photophysical processes responsible for fluorescence emission, energy redistribution and relaxation in these molecules after photoexcitation as a function of environmental conditions. Therefore, as an additional goal of current research fluorescence models have been developed for several of the here measured species (e.g., [28-31]), and some of these will be further validated and improved in this thesis, while new ones are also presented.

2.2 Use of fluorescent tracers

Two different approaches to LIF diagnostics can be distinguished. In the first one the fluid of interest naturally shows fluorescence upon laser illumination. This is the case for typical commercial fuels, like gasoline, Diesel, or kerosene. In such fluids a large amount of unknown fluorescing species cause a highly undefined fluorescence signal allowing only qualitative measurements. When looking at, e.g., flame zones, naturally generated species are present like OH or NO. When only one species is excited by choosing the correct excitation wavelength, quantitative measurements are possible, but they are limited to conditions and regions where these species are present.

In the second case, the fluid of interest does not show measurable fluorescence. In this situation a single fluorescing species, a so-called tracer, is added in low concentrations (1–10%) in order not to disturb the chemical properties of the fluid significantly. As in

this case the signal is generated by only one defined species, quantitative measurements are possible if the fluorescence properties of the tracer are known as a function of external conditions (e.g., pressure, temperature).

The tracer must be chosen carefully depending on the investigated system. Ideally, the tracer should behave exactly like the fluid of interest in terms of evaporation, diffusion characteristics, and reactivity. As mentioned above, commercial fuels cause a highly undefined LIF signal. Thus, mostly a non-fluorescing surrogate with similar combustion and gas-dynamics properties is chosen and a tracer is added to this surrogate to yield the necessary information. One example is choosing toluene as a tracer for gasoline surrogate fuels [7], typically being iso-octane or n-heptane. Toluene is naturally present in gasoline. Therefore, the overall characteristics will be matched closely. In general, the conditions mentioned above cannot be satisfied simultaneously by one tracer. Several tracer species would be required; the latter choice would complicate the approach.

In the ideal case, the tracer-LIF signal intensity is directly proportional to the desired quantity and independent on other environmental conditions. Generally, however, the fluorescence signal simultaneously depends on temperature, pressure, and bath gas composition. It is thus of great importance to explore these dependences in test cells under well-defined environmental conditions to provide the data required for quantitative diagnostics in practical applications.

The easiest realisation of a tracer is a single atom or small inorganic molecules. The first following section will focus on these classes of tracers. Organic tracer molecules, however, are usually less or not toxic and not corrosive, many of them have high vapour pressures. Their absorption mainly takes place in the UV range, while the emission is located in the UV/Vis range. The natural occurrence in commercial fuels and the often high fluorescence quantum yields make them attractive for tracing fuel distributions in mixtures as well as in flow diagnostics. The most commonly used classes of organic tracers are aromatics and ketones. The following sections will describe in detail typical spectral and photophysical properties of selected tracer species, a third section will point out some general remarks about additional organic molecules less known as tracer species.

2.2.1 Atoms and small inorganic molecules

Atoms usually have a large absorption cross-section and a high fluorescence quantum yield. Their optical excitation is possible in the UV/Vis spectral region. The main problem is the generation of suitable atoms from their (molecular) precursors, which either requires high temperatures – when generated by pyrolysis – or intense laser radiation, when generated by photo-dissociation. In flames atomisation of metal salts to generate thallium or indium atoms is possible and has been used to gain information about temperature by two-line atomic fluorescence [32-33]. However, for diagnostics applications

in mixing cold gas flows or mixture formation in IC engines prior to combustion, atoms are not suitable as fluorescent tracer species.

Di- or triatomic inorganic in-situ formed molecules are often used in combustion diagnostics. OH, CH or C_2 radicals formed in the combustion zone (e.g. [34-37]) allow measurements in the region of the flame front, but are not suitable for measurements in low-temperature gas flows or prior to ignition.

Nitric oxide (NO) as a stable species at and below flame temperatures was investigated extensively, and its spectroscopy is well understood ([38] and references therein). Gas-phase thermometry using NO LIF is widely used [39-40] (see section 2.3.2). Sulphur dioxide (SO_2) also can be excited with typical UV wavelengths (e.g., 248 and 266 nm) [41-42] and LIF detection strategies have been developed [43]. The advantage of NO and SO_2 is the thermodynamic stability allowing their detection throughout flames or other regions of harsh environments. Iodine (I_2) can be excited and its fluorescence detected in the visible spectral range [44]. All three mentioned species, however, are corrosive or toxic, thus limiting the applicability mostly to enclosed experiments.

2.2.2 Aromatic organic molecules

Figure 1 displays the chemical formulas of aromatic species investigated for tracer LIF diagnostics. Table 1 summarises their thermodynamic properties.

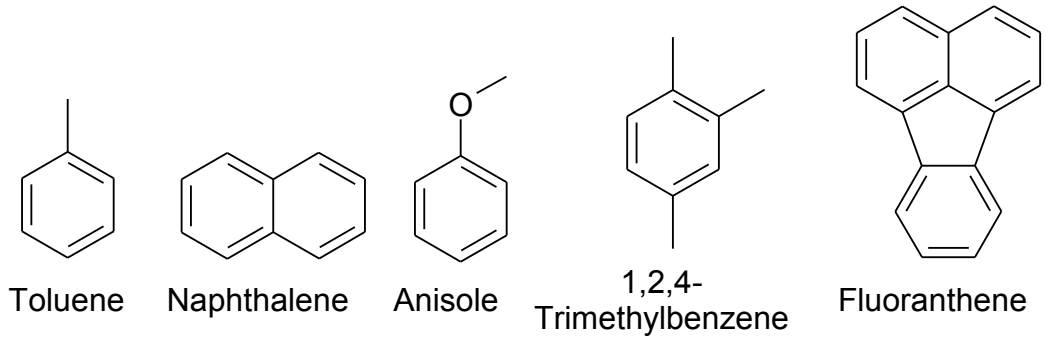

Figure 1: Chemical structures of several aromatic species used for tracer-LIF applications.

Table 1: Thermodynamic properties of often used aromatic tracer species

	Toluene	Naphthalene	Anisole	1,2,4-Trimethylbenzene	Fluoranthene
Chemical formula	C_7H_8	$C_{10}H_8$	C_7H_8O	C_9H_{12}	$C_{16}H_{10}$
Molecular mass (g/mol)	92.1	128.2	108.1	120.2	202.3

Melting point (K)	178	353	236	229	383
Boiling point (K)	384	491	427	442	657
Density at 293 K (g/cm^3)	0.87	1.14	0.99	0.86	1.24
Vapour pressure at 293 K (mbar)	29	0.024	3.6	2.8	0.01

Toluene

Toluene is often chosen because it traces well the evaporation and ignition behaviour of gasoline. Its relatively high vapour pressure together with its high fluorescence quantum yield (see below) also enables imaging of (cold) gas mixing processes. The fluorescence of toluene has been investigated since 1929 [45-46]. Figure 2 (left) shows gas-phase absorption spectra for different temperatures ranging from room temperature up to 1128 K [47]. At room temperature the spectrum covers a range from roughly 240 up to 270 nm. At the given spectral resolution the fine structure observable at room temperature washes out at higher temperatures, accompanied by a significant red-shift of the peak and a broadening of the whole spectrum. Excitation is possible with typical UV laser sources like KrF* excimer (248 nm) or frequency-quadrupled Nd:YAG lasers (266 nm). The absorption cross section of around 3×10^{-19} cm^2 stays nearly constant with increasing temperature for 248 nm excitation whereas for 266 nm excitation the absorption cross section increases (cf., Figure 2) [47].

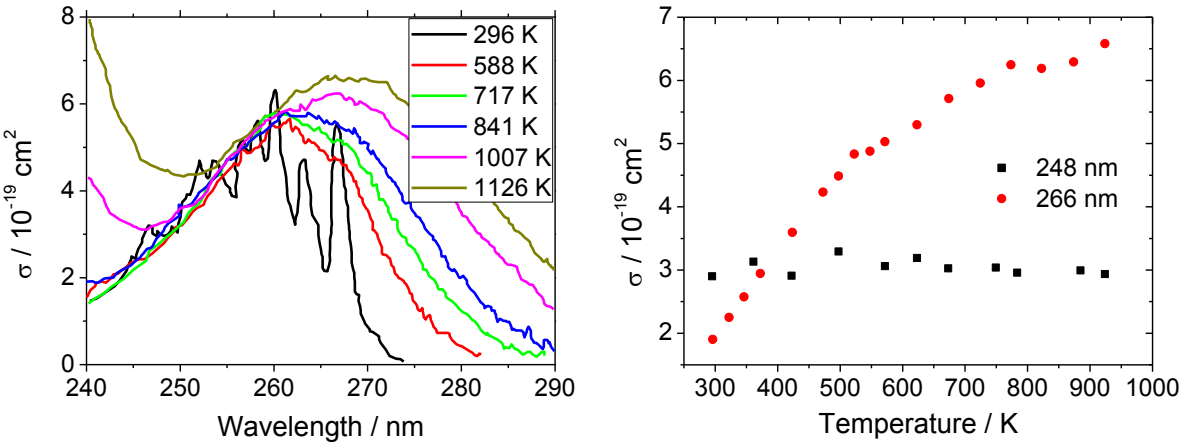

Figure 2: Toluene absorption spectra for different temperatures in 1 bar nitrogen (left panel) and toluene absorption cross section for excitation laser wavelengths of 248 nm and 266 nm as a function of temperature (right panel, Koban *et al.* [47]).

Fluorescence from toluene is emitted with high quantum yield [48] in the wavelength range of 270 up to about 320 nm, with a peak at around 285 nm at room temperature. With increasing temperature the emission spectrum shifts to the red by about 2 nm /

100 K while its Full-width-half-maximum (FWHM) also increases (cf., Figure 3, left panel) [31, 47]. This change of the position and shape of the fluorescence spectrum has been exploited in two-colour detection strategies for determining temperature [18, 22]. The fluorescence quantum yield decreases by three orders of magnitude when increasing the temperature from room temperature up to about 950 K, more pronounced for 248 nm than for 266 nm excitation (cf., Figure 3, right panel) [31, 47], which also can be exploited as a measure of temperature. Koban *et al.* derived a model function describing this dependence [47] which was later expanded to include the effect of O_2 on toluene LIF intensities [29]. For an absolute calibration the room temperature value of 0.3 (266 nm) and 0.1 (248 nm), respectively, can be used for the fluorescence quantum yield [48]. These quantum yields, however, were measured at low pressures (~22 mbar pure toluene). As shown later, total pressure affects the fluorescence quantum yield. Thus, these values would need to be corrected when used at atmospheric pressure.

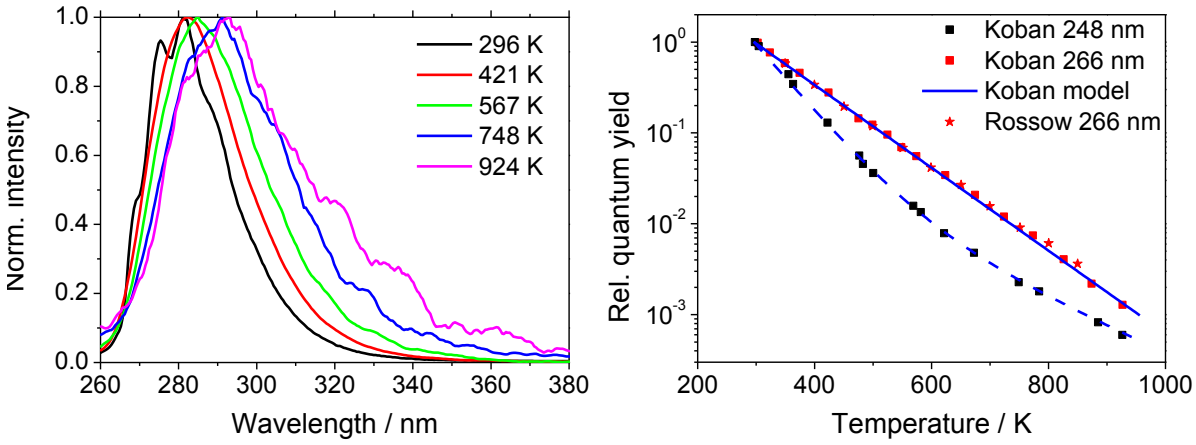

Figure 3: Normalised toluene fluorescence spectra for different temperatures upon 248 nm excitation (left panel, Koban *et al.* [47]) and evolution of the relative fluorescence quantum yield for 248 nm and 266 nm excitation (right panel, Koban *et al.* [47], Rossow [31]) with temperature in comparison with modelled relative quantum yields for 248 and 266 nm excitation (Koban *et al.* [29]).

Effects of total pressure on toluene fluorescence quantum yield were less often investigated. Rossow reports a pressure-induced decrease of quantum yield upon 266 nm excitation of about 70% at 450 and 700 K when increasing the pressure from 1 to 30 bar [31]. Cheung observed at 296 K nearly no pressure influence for 266 nm excitation [49], whereas for 248 nm excitation (at 296 K) a small increase of quantum yield was observed [8, 49-50]. Systematic investigations, however, are still missing.

Toluene fluorescence is known to be strongly quenched by molecular oxygen. This behaviour can be expressed by the Stern-Volmer relation (cf., chapter 3). Figure 4 (right panel) shows the significant decrease of fluorescence quantum yield with increasing oxygen partial pressure at 1 bar total pressure [29, 31] together with model predictions from the Koban model for the data taken with 248 nm excitation. The quenching effect of O_2 is reduced at higher temperatures, thus leading to the breakdown of the FARLIF concept

[51], in which the toluene LIF signal is assumed to be proportional to the local fuel / air ratio (see detailed discussion by Koban *et al.* [29, 52-53], cf., section 2.3).

Additionally, upon 248 nm excitation the fluorescence spectra show a red-shift with increasing O_2 partial pressure (cf., Figure 4, left panel). While the red-shift is strong at low O_2 partial pressures, it tends to saturate at around 200 mbar of O_2 [29]. Based on these results, a two-colour detection technique for measuring oxygen distributions has been developed [54], similar to the two-colour detection strategy for temperatures.

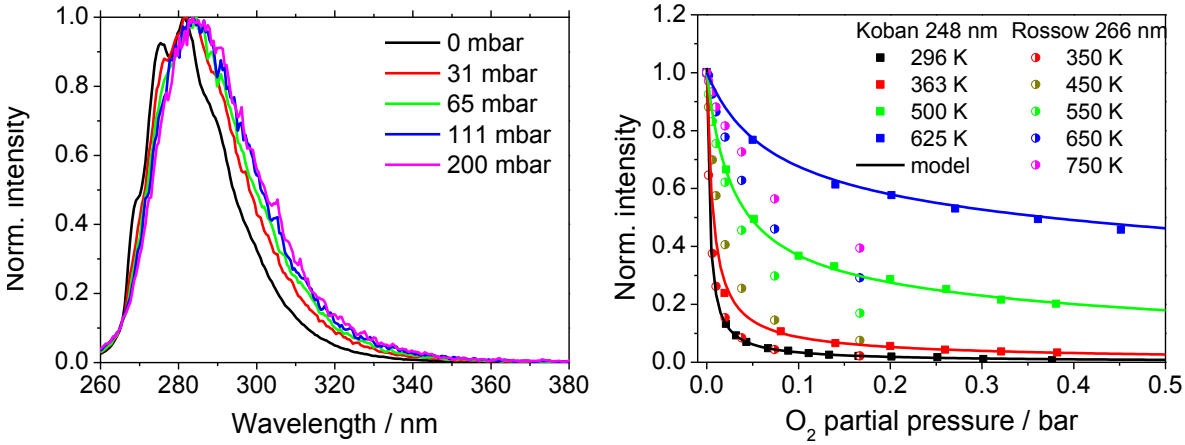

Figure 4: Normalised fluorescence spectra of toluene for different O_2 partial pressures at room temperature upon 248 nm excitation (left panel, Koban *et al.* [29]) and fluorescence quantum yield vs. O_2 partial pressure for different temperatures upon 248 and 266 nm excitation, comparison to modelled quantum yields for 248 nm excitation (right panel, Koban *et al.* [29], Rossow [31]).

However, contrary to numerous studies dealing with time-integrated LIF measurements of vapour-phase toluene in a wide range of temperature, pressure, and bath gas composition, only few studies directly investigate the lifetime of the electronically-excited S_1 state reached after photon absorption. Zimmermann *et al.* [55] determined toluene fluorescence lifetimes at 1 bar total pressure as a function of temperature and various O_2 partial pressures upon 248 nm excitation. For 266 nm excitation only studies at room temperature (or below), at low pressure (about 13.3 mbar and below) [56-59], or in air at 1 bar [60] are available. Despite its potential as a diagnostic tool for, e.g., gas phase thermometry, the variation of the fluorescence lifetime with environmental conditions was sparsely exploited for this purpose. Very recently, Friesen *et al.* demonstrated temperature measurements in an IC engine using the fluorescence lifetime of toluene [61-62].

1,2,4-Trimethylbenzene

One attractive tracer species not further mentioned here, is 1,2,4-trimethylbenzene [63]. At room temperature its fluorescence spectrum is about 10 nm red-shifted with respect to toluene, and has a slightly increased temperature-dependent red-shift of the spec-

trum, while the temperature dependence of its quantum yield in N_2 is comparable to toluene. The sensitivity to O_2 quenching is slightly more pronounced. The higher boiling point and thus lower vapour pressure with respect to toluene allows tracing of lower volatile fuels like, e.g., Diesel or kerosene. 1,2,4-Trimethylbenzene was identified as one species responsible for fluorescence emission in kerosene [64].

Naphthalene

Naphthalene as a natural component of many commercial fuels is often chosen to trace surrogate Diesel fuels or kerosene as its evaporation characteristics match best. Naphthalene is solid at room temperature and thus needs to be dissolved in a liquid for reliable mixing into the gas phase. Therefore, despite numerous studies of the basic photophysics of naphthalene for more than a hundred years (e.g., [13, 65-70] and references therein), its use as fluorescence tracer is not as common as toluene. Systematic investigations of naphthalene fluorescence properties under engine-related conditions have been performed by Orain *et al.* [71]. In earlier studies experiments were restricted in the temperature range investigated [20], or performed just in pure N_2 as bath gas at 1 bar total pressure [13].

Absorption spectra of naphthalene are published only for low temperatures, e.g., for 313 K [72] ranging roughly from 240 to 280 nm. Temperature-dependent studies of absorption spectra are not available in the temperature range of interest as for toluene. Temperature-dependent absorption cross-sections at 266 nm, however, show little variation within experimental uncertainty in the 350–900 K range [71]. Hence, fluorescence intensities can be interpreted as a relative quantum yield with good approximation.

At 350 K fluorescence emission of naphthalene extends roughly from 300 to 400 nm with a peak around 335 nm (cf., Figure 5, left panel). The spectrum's red-shift, however, is more pronounced (5 nm / 100 K) than for toluene (2 nm / 100 K; cf., Figure 3). Two-colour thermometry using naphthalene similar to techniques developed for toluene has been demonstrated [20]. The temperature dependence of the naphthalene fluorescence quantum yield (cf., Figure 5, right panel) shows a reduced sensitivity with respect to temperature compared to toluene [13, 71] (cf., Figure 3, right panel). In contrast to toluene, increasing the total pressure in N_2 as bath gas leads to a slight increase by 10 % in quantum yield.

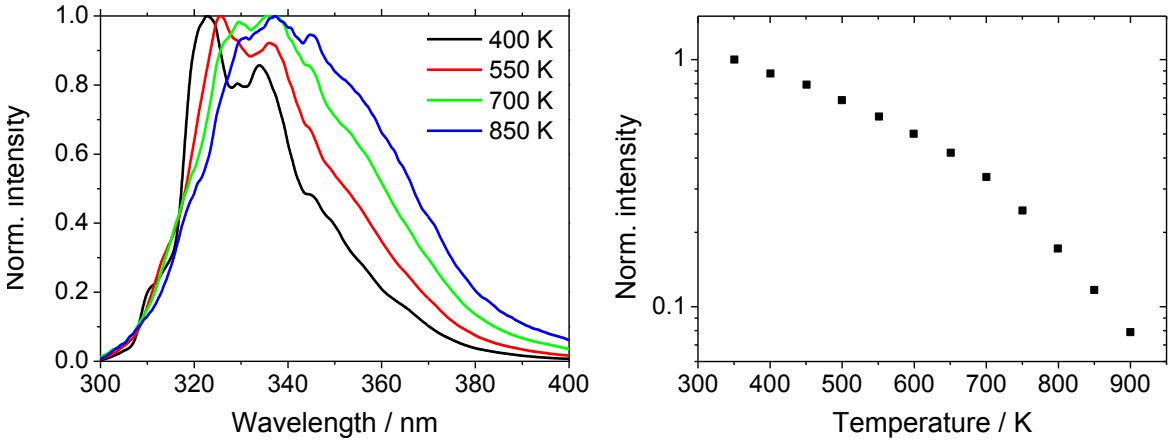

Figure 5: Normalised naphthalene fluorescence spectra for different temperatures upon 266 nm excitation at 1 bar in N_2 (left panel) and evolution of the relative fluorescence quantum yield with temperature at 1 bar (right panel). Data from Orain *et al.* [71].

Also for naphthalene, molecular oxygen has a strong fluorescence quenching effect (cf., Figure 6, right panel), which is even stronger than for toluene (cf., Figure 4, right panel). Again, the quenching effect diminishes at higher temperatures, but by a smaller amount than for toluene. Upon 266 nm excitation a red-shift of the fluorescence spectrum is observed (cf., Figure 6, left panel), slightly more pronounced than for toluene upon 248 nm excitation [13, 20, 71]. Detection strategies using this red-shift to determine oxygen distributions, however, have not yet been explored.

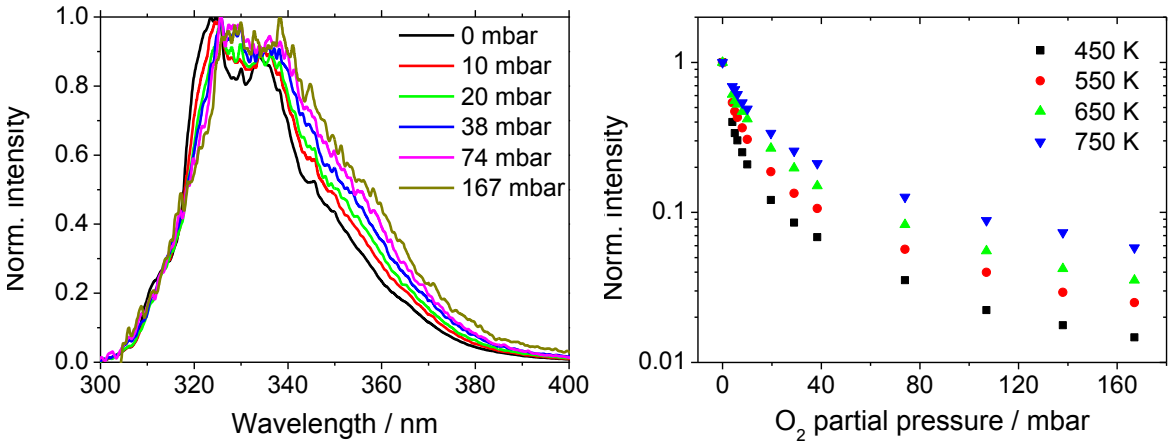

Figure 6: Normalised naphthalene fluorescence spectra for different O_2 partial pressures at 450 K upon 266 nm excitation (left panel), and relative fluorescence quantum yield vs. O_2 partial pressure for different temperatures at 1 bar total pressure (right panel). Data from Rossow [31].

Effective fluorescence lifetimes of naphthalene were investigated by several groups. Early measurements mostly were performed for selected environmental conditions (e.g., low temperature and low pressure, [66]). Ni and Melton [73] and Ossler *et al.* [13] determined naphthalene fluorescence lifetimes as a function of temperature in 1 bar nitrogen. The influence of oxygen and / or total pressure on the lifetime, however, has not

been investigated yet. Two lifetime components have been observed [13]. In contrast to toluene, the fluorescence lifetime of naphthalene has been used to determine temperatures in gas flows [73] and standard burners [14], but only in the absence of oxygen.

1-Methylnaphthalene

1-Methylnaphthalene, despite its larger molecular weight compared to naphthalene, is liquid at room temperature. As the photophysical properties are very similar to those of naphthalene it should be an easier to handle alternative to naphthalene. However, investigations within the tracer LIF community of Diesel fuels or kerosene mostly use naphthalene instead. The fluorescence spectrum of 1-methylnaphthalene is slightly red-shifted (~4 nm) with respect to naphthalene. Investigations of 1-methylnaphthalene are more seldom than those of naphthalene. Kaiser and Long investigated O_2 quenching of 1-methylnaphthalene at two temperatures [20] and found similar quenching efficiency towards O_2 as for naphthalene. 1-Methylnaphthalene has been used to "simulate" a kerosene emission spectrum and has been identified as being essential for correctly representing fluorescence spectra of kerosene and Diesel fuels [64].

Fluoranthene

For the very low volatile fractions of kerosene, fluoranthene was considered to be a suitable tracer. Its emission in the visible spectral range reduces the experimental effort because it does not require quartz optics in the detection channel. Fluoranthene fluorescence has been investigated as function of temperature and pressure by multiple groups (e.g. [74-76]). In contrast to all other aromatics mentioned here fluoranthene can be excited with both 266 and 355 nm, resulting in indistinguishable fluorescence spectra ranging from 380–600 nm with a peak around 450 nm (cf., Figure 7, left panel). In contrast to, e.g., toluene or naphthalene a spectral red-shift with increasing temperature is not reported. The fluorescence quantum yield strongly decreases with temperature, it increases with increasing total pressure (cf., Figure 7, right panel) with this trend diminishing with temperature, and it shows moderate O_2 quenching ([74-75] and references therein). Fluorescence lifetimes have been reported, but only in solution [77] and in the gas phase for a restricted temperature range [75]. Application of the fluorescence lifetime of fluoranthene for two-dimensional imaging has been discussed in [77] and demonstrated in the gas phase [75].

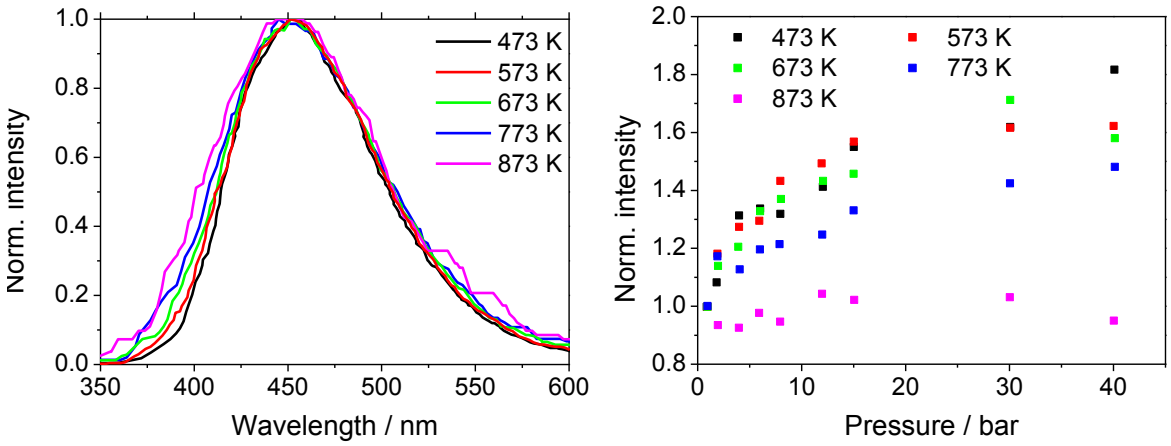

Figure 7: Normalised fluorescence spectra of fluoranthene for different temperatures at 12 bar in N_2 (left panel), and normalised fluorescence quantum yield as function of total pressure for several temperatures (right panel) upon 355 nm excitation (Kühni *et al.* [74]).

Anisole

For anisole only very few investigations of its photo-physical properties are available. In contrast to many other aromatics anisole is non-toxic and non-carcinogenic. Therefore, it should be an attractive alternative for tracer-LIF applications. In most commercial fuels anisole is not a natural component. Its chemical structure, however, is very similar to natural fuel components. Its fluorescence was investigated in 1924 [78] for the first time, and the application as a tracer for gas flows was already discussed by Hirasawa *et al.* [19]. Anisole shows significant absorption at 266 nm (absorption cross section ~10^{-17} cm^2 [79]) and its fluorescence spectrum covers the wavelength range between 270 and 360 nm, with a peak around 290 nm. The 63% larger fluorescence quantum yield (measured in the liquid phase, [80]) and the about 50 times higher absorption cross section compared to toluene should significantly improve signal strengths under otherwise identical conditions which makes anisole an attractive alternative for toluene in typical LIF-imaging applications. However, there are no known systematic investigations in a wider range of conditions as would be needed for typical tracer LIF applications.

2.2.3 Ketones

In contrast to the many different aromatic organic tracer molecules, the number of ketones used for tracer LIF is limited. Most common species in the group of ketones are acetone and 3-pentanone, while biacetyl as a diketone is used less frequently. Figure 8 shows the chemical structure of the three mentioned species.

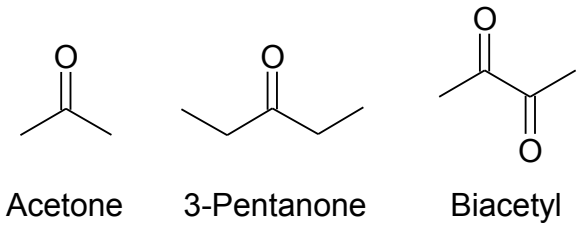

Figure 8: Chemical structures of ketones commonly used for tracer LIF applications.

Acetone and 3-pentanone

As acetone and 3-pentanone behave photophysically very similarly, they will be presented and discussed together. Their fluorescence was first described in the 1930s [81-82]. The most important differences between acetone and 3-pentanone are their boiling point and their vapour pressure (cf., Table 2) which thus mainly determines their practical applications. Acetone (boiling point 56°C) is often used to trace low temperature gaseous flows, whereas 3-pentanone (boiling point 101°C) is often used in engine applications (boiling point of gasoline ~110°C). Lozano *et al.* in their pioneering work about 20 years ago demonstrated the applicability of acetone LIF for imaging in gaseous flows [83], while the applicability of 3-pentanone in an engine was demonstrated by Neij *et al.* [84] two years later. However, without detailed knowledge of the photophysical properties and their underlying processes only qualitative measurements were possible, which triggered extensive work on ketone photophysics (e.g., [28, 31, 85-89]).

Table 2: Thermodynamic properties of ketone tracer species

	Acetone	3-Pentanone	Biacetyl
Chemical formula	C_3H_6O	$C_5H_{10}O$	$C_4H_6O_2$
Molecular mass (g/mol)	58.1	86.1	86.1
Melting point (K)	178	234	271
Boiling point (K)	331	375	361
Density at 293 K (g/cm^3)	0.79	0.81	0.99
Vapour pressure at 293 K (mbar)	246	16	65

In acetone and 3-pentanone the n→π* transition of the carbonyl group is responsible for absorption and emission of light. The broadband absorption spectrum at 296 K extends from 230 to 320 nm (cf., Figure 9, left panel) [90], thus allowing for efficient excitation with wavelengths from a KrF* excimer laser (248 nm), a frequency-quadrupled Nd:YAG laser (266 nm), or a XeCl* excimer laser (308 nm). With increasing temperature the absorption increases while the spectrum is simultaneously broadened and red-shifted (cf.,

Figure 9). The variation of the absorption cross section with temperature depends on the wavelength (cf., Figure 9, right panel) [87]: for 248 and 266 nm it is nearly constant, whereas for 308 nm it increases monotonically with temperature. Results for acetone are similar with only slightly smaller absolute values. Temperature measurement strategies based on two-colour excitation have been demonstrated [87, 89, 91], see also section 2.3.

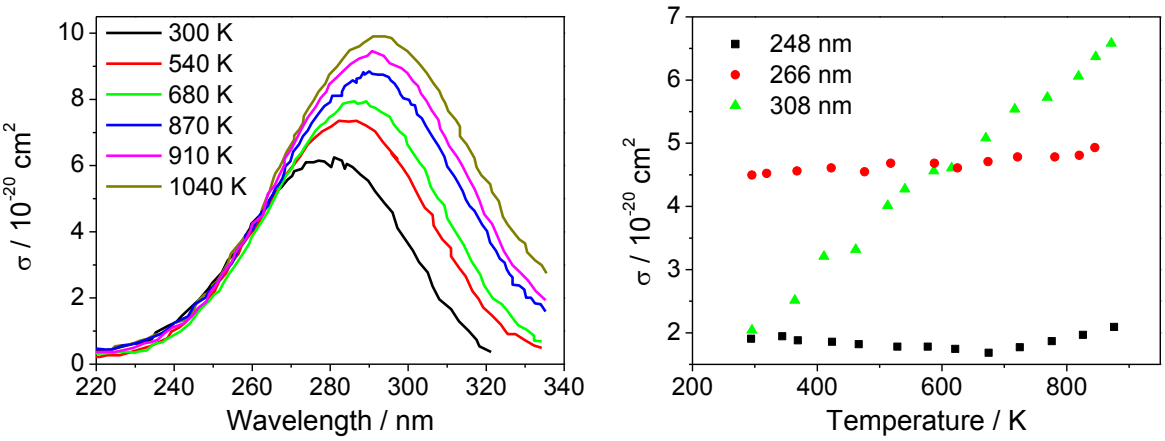

Figure 9: 3-pentanone absorption spectrum as a function of temperature (left panel, Koch [30]) and variation of the absorption cross-section with temperature at the typical laser wavelengths 248, 266, and 308 nm (right panel, Koch and Hanson [87]). For acetone, the general dependences are comparable.

In contrast to aromatics, ketones photo-dissociate to a significant fraction upon absorption of UV photons [92]. Luminescence emission was first observed as by-product during photolysis experiments [81]. The fluorescence quantum yield of acetone is about two to three orders of magnitude lower than that of aromatics [93]. That means that competing non-radiative processes are clearly dominant against fluorescence. Efficient ISC from the S_1 to the T_1 state occurs [94] due to the low energy gap between S_1 and T_1 of 3200 cm^{-1} [95]. Thus acetone shows efficient phosphorescence at room temperature – in contrast to aromatics – with a phosphorescence lifetime of about 200 µs [96]. This phosphorescence is efficiently quenched by O_2 due to the triplet structure [83].

Upon excitation at 266 nm most acetone molecules dissociate, primarily into methyl and acetyl radicals (e.g. [97-98]) in a Norrish-I [99] reaction. At excitation wavelengths below 254 nm the acetyl radical can also dissociate into a second methyl radical and carbon monoxide [100]. Two acetyl radicals can recombine to a biacetyl molecule ([101] and references therein) that influences the emission of light with respect to spectral shape and fluorescence quantum yield. In the literature inconsistent studies exist that discuss the origin of fluorescence emission after photoexcitation originating from the parent molecule itself or from photolysis products ([98, 102] and references therein). Most authors, however, claim acetone itself as being the emitter. For 3-pentanone such detailed investigations are not available, however, it is easy to imagine that for 3-pentanone similar processes occur because the chromophore is the same and only the substituents vary slightly.

In contrast to aromatics the fluorescence spectra of ketones are far red-shifted with respect to absorption and are located between 350 and 550 nm [93] (cf., Figure 10, left panel), nearly identical for acetone and 3-pentanone [31]. Within experimental error the spectral shape does not change with excitation wavelength, temperature, pressure, and O_2 concentration. Therefore, two-colour detection strategies exploiting the change of the spectral shape of the fluorescence signal as described with aromatics are not possible.

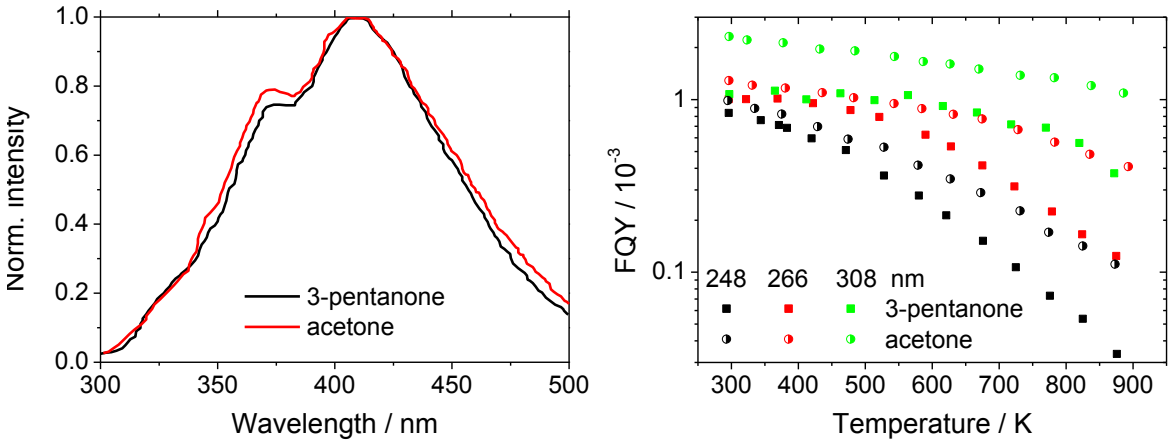

Figure 10: Normalised fluorescence spectra of 3-pentanone and acetone upon 266 nm excitation (left panel, Rossow [31]) and fluorescence quantum yield of 3-pentanone and acetone as a function of temperature for 248, 266, and 308 nm excitation (right panel, Thurber *et al.* [28], Koch and Hanson [87]).

The fluorescence quantum yield of ketones in N_2 at 300 K is about two orders of magnitude lower than for aromatics [28, 85, 93]. In addition to absolute quantum yields, relative quantum yields have been investigated as a function of temperature, pressure, and oxygen concentration for various excitation wavelengths (e.g. [86, 88, 103-105]). The influence of temperature on the quantum yield, however, is less pronounced than for e.g. toluene (cf., Figure 10, right panel, and Figure 11, right panel).

Increasing total pressure leads to an increase in quantum yield for excitation wavelengths below 300 nm until a limiting value at higher pressures is reached at around 10 bar (cf., Figure 11). For ketones, O_2 quenching is much less efficient than with aromatics. For a first approximation, the quenching influence was seen not to be present. An early evidence of O_2 quenching of ketone fluorescence, however, was given by Nau and Scaiano who demonstrated a weak quenching influence of O_2 on ketone fluorescence [106]. At moderate pressures (<3 bar), the ketone quantum yield is nearly the same in N_2 and air as bath gas. Increasing air pressure leads at high pressures to a small decrease in quantum yield, while in pure O_2 as buffer gas this quenching effect is always visible (cf., Figure 11, left panel). Due to the insensitivity towards O_2, ketones are often used as tracers during the compression stroke of motored or fired IC engine operation when the spatial distribution of the fuel number density is the quantity of interest.

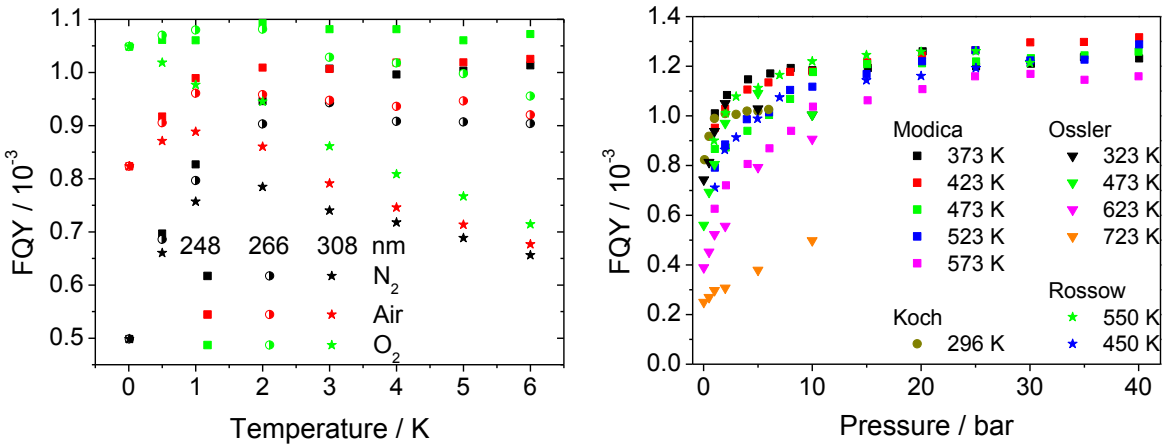

Figure 11: Fluorescence quantum yields of 3-pentanone as a function of pressure for 248, 266, and 308 nm excitation at 296 K (Koch [30]) for different bath gases (left panel) and for 266 nm excitation at different temperatures in N_2 as bath gas (right panel). Relative values from [31, 88, 107] are scaled to the absolute values of [93] at 1 bar.

Fluorescence lifetimes of ketones were systematically investigated by Ossler *et al.* [107] for different temperatures in nitrogen and air as bath gas. Earlier measurements were mostly restricted in temperature and to pure acetone vapour (e.g. [108]). The lifetimes are much shorter than for aromatics (~2 ns at 300 K), but mirror in a similar way the dependence of the quantum yield on environmental conditions.

In contrast to aromatics, the phosphorescence of ketones can be measured at room temperature in the absence of O_2. While the phosphorescence spectrum is not much different from the fluorescence spectrum, phosphorescence takes place on a much longer timescale (~1 ms). Due to the triplet structure of molecular oxygen, phosphorescence is very efficiently quenched by even small traces of O_2. This quenching effect can then be used for two-dimensional imaging of gas-flow mixing where one flow contains O_2 (or air) and acetone whereas the other is acetone in pure N_2 as bath gas [109]. In many practical applications, however, the timescale of phosphorescence is too long for instantaneous imaging or oxygen is present anyway. Therefore, ketone phosphorescence is usually used only in special applications.

Biacetyl

In addition to the ketones acetone and 3-pentanone, biacetyl as diketone was explored as tracer substance (e.g., [110]). The broadband absorption spectrum ranges from 340 to 470 nm (cf., Figure 12, left panel). In contrast to acetone or 3-pentanone biacetyl can thus be excited with 355 nm. The fluorescence quantum yield is low (~0.2%), but biacetyl shows significant phosphorescence that is quenched in the presence of O_2. The influence of temperature and pressure is comparable to acetone or 3-pentanone (cf. Figure 12, right panel).

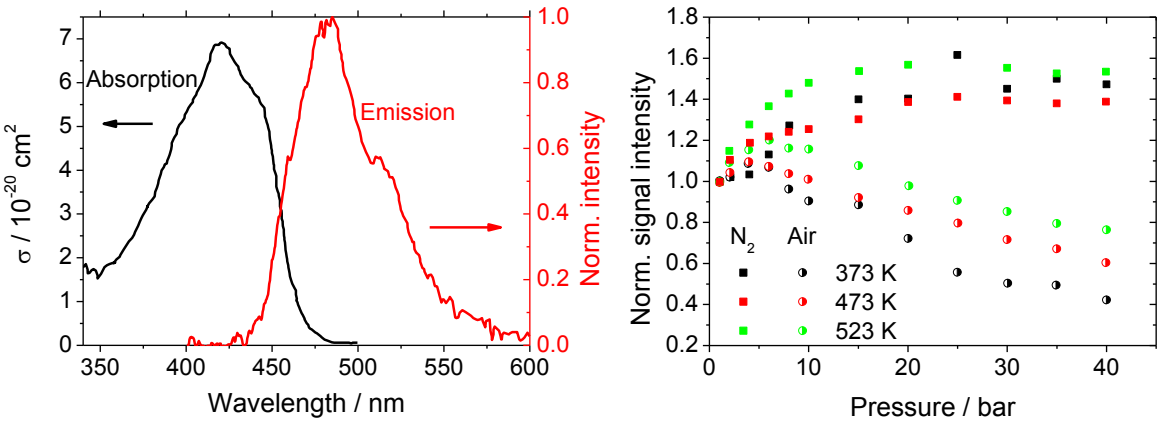

Figure 12: Biacetyl absorption and emission spectrum in N_2 at 523 K, 20 bar (left panel) and evolution of the emission intensity with pressure for three temperatures in N_2 and air (right panel) (Guibert *et al.* [110]).

As the evaporation characteristics of biacetyl do not match very well to those of gasoline (e.g. its boiling point is 361 K), the interest in biacetyl as tracer is not so pronounced. Additionally, the applicability of biacetyl is limited to closed setups due to its strong rancid malodour. In an IC engine biacetyl was used as a tracer to visualise fuel distributions quantitatively [111-112]. As an advantage, biacetyl can be excited with 355 nm radiation which enables high-speed in-cylinder LIF imaging [113] because for this excitation wavelength high repetition rate lasers with high laser power are available. Nevertheless, not much work has been performed so far in predicting fluorescence quantum yields via photo-physical models.

Similar to the 3-pentanone / toluene pair for quantitative imaging of gasoline, 5-nonanone and 2-decanone were selected as specific ketone partners for naphthalene when imaging Diesel-type fuels [114], but their low stability prevents their use in practical applications.

2.2.4 Other organic tracers

Beyond aromatics and ketones, other organic tracers have been explored. Aliphatic amines, such as triethylamine (TEA) or diethylmethylamine (DEMA) have been investigated as single tracers [115] or as part of exciplexes for laser-induced exciplex fluorescence (LIEF) [116] to distinguish between fluorescence emission originating from droplets and tracer vapour. Despite significant absorption at typical laser wavelengths like 248 or 266 nm and a sufficient quantum yield the corrosiveness and the strong malodour of aliphatic amines extremely constrains their applicability.

Aliphatic ethers have also been explored, e.g., dimethyl ether [117]. As dimethyl ether is gaseous at ambient conditions, it should be an ideal tracer for gas flows. However, significant absorption only takes place at wavelengths below 200 nm. Together with the low fluorescence quantum yield this limits the applicability to some special cases.

2.3 Typical applications of tracer-LIF diagnostics

There is a wide field of possible applications of tracer LIF. Beyond thermometry, which will be outlined in the following sections, the non-intrusive measurement of, e.g., fuel concentrations or fuel / air ratios is a typical field of application.

In most cases practical applications of tracer LIF are realised via LIF imaging. In this technique the laser beam is formed to a laser sheet which means a nearly two-dimensional laser beam. Typical dimensions of a laser sheet are a height of 20–30 mm and a thickness of around 0.5 mm. The fluorescence emission is optically filtered and imaged perpendicular to the illumination plane on a CCD or CMOS camera.

In many cases intensified CCD (ICCD) cameras are used because the emission wavelengths are in the UV range of light and / or of low intensity. The intensifier increases the detection efficiency and makes the CCD sensitive for UV light, but this goes along with a reduced spatial resolution. The emission of ketones, however, is located in the visible spectral range, which enables commercial camera lenses to be used. In some cases non-intensified CCD cameras can be used to enhance the spatial resolution [118].

Initial applications of tracer LIF was the qualitative, and later quantitative, visualisation of gas or fuel distributions in gas flows (first example [83]) and IC engines (first example [84]) which is still of great interest and widely applied.

For the optimisation of combustion processes the local fuel/air ratio must be known to avoid fuel pockets with enhanced pollutant formation. LIF imaging strategies using two-colour detection techniques in a similar way as for thermometry (see below) have been demonstrated [54]. Since the fluorescence of aromatics is efficiently quenched by O_2, first assumptions were that the fluorescence signal of toluene is directly proportional to the fuel/air ratio (Fuel/Air Ratio LIF, FARLIF) [9, 51]. However, work of Koban *et al.* [21, 29, 52-53] for toluene and Kaiser and Long [20] as well as Orain *et al.* [71] for 1-methylnaphthalene and naphthalene, respectively, showed that this assumption is in most cases not justified.

2.3.1 Thermometry with organic tracers

One of the most important applications of tracer LIF is thermometry, i.e., temperature measurement, often spatially resolved. As an example the knowledge of local in-cylinder temperature distributions in the compression stroke of an engine prior to ignition is crucial for optimisation of combustion processes. Thermometry techniques can be classified in single- and two-colour techniques, the latter one can be subdivided in two-colour excitation and detection techniques.

Single-colour techniques (e.g., [119]) can be applied when tracer and O_2 concentration is known and constant, e.g., in a homogeneously seeded gas flow of N_2 and tracer. In this technique the tracer is excited with radiation at one wavelength and the signal is collected in one wavelength range of the fluorescence spectrum (generally the full spectral emission range). The temperature can then be calculated from the known relationship between measured signal intensity and temperature derived from cell experiments. The advantages of single-colour thermometry are the high signal intensity, rather low experimental effort, and the compact arrangement. However, it fails when tracer and / or O_2 concentration is not constant throughout the measurement volume.

Two-colour excitation techniques (e.g., [91]) take advantage of temperature-dependent shifts of the absorption spectrum that can be observed for ketones as well as for aromatics. The excitation is performed with two different and carefully chosen excitation wavelengths while the fluorescence is collected in one wavelength range. The laser pulses are triggered one after the other within a short time interval which needs to be short enough with respect to the time scales of turbulent motion in the fluid. Detection is realised with a double-framing camera or two single cameras with subsequent image mapping procedure. In the latter case the detected signal intensity is often reduced due to a beam splitter arrangement imaging the signal on both cameras simultaneously. The flexibility of this technique is hampered by the rather high experimental complexity and costs.

The *two-colour detection technique* (e.g., [119]) takes advantage of changes in the emission spectrum with temperature as known from the previous section for most aromatic tracer species. Excitation is performed with one excitation wavelength. Emission is detected in separate spectral ranges with two cameras, which again requires exact spatial mapping of both images. The spectral ranges are chosen for maximum temperature sensitivity in the ratio of the collected signal intensities. The ratio between both channels yields the temperature, independent on the local tracer concentration. As an advantage, laser light sheet inhomogeneities and fluctuations in laser power are cancelled out. Compared to the two-colour excitation technique the experimental effort is reduced. However, detected signal intensities are lower because each camera only receives a (spectral) fraction of the total fluorescence emission. The technique only works with aromatics because only they show spectral shifts with temperature or O_2 partial pressure, which all may limit the applicability.

2.3.2 Thermometry with NO and OH

As outlined in section 2.2.1 NO and OH are fluorescing species stable in flame zones. This allows the non-intrusive temperature measurement in flames or other reactive media like plasmas [120].

The absorption spectra of NO and OH show a distinct line structure. The line strengths and shapes are temperature dependent. When scanning the LIF excitation spectrum of

NO or OH in a stable flame, the temperature can be calculated by assuming a Boltzmann distribution throughout the vibration-rotational manifold of the molecule. For NO LIF a fitting routine has been established using five characteristic absorption lines. In this routine a simulated excitation spectrum is fitted to the measured one with the temperature as the only variable parameter (e.g., [40, 121]).

2.3.3 Alternative thermometry techniques

LIF with fluorescing species is not the only option for measuring gas-phase temperature with optical techniques. In the following paragraphs some of these will be shortly reviewed.

Absorption spectroscopy methods

A classical non-intrusive measurement technique is absorption spectroscopy. Typically, the experiment is performed in a line-of-sight arrangement. It is advantageous that almost all fluids of interest exhibit absorption features in the ultraviolet, visible and/or infrared spectral region. For example, organic fuels can directly be observed by absorption spectroscopy. One common subject in absorption studies is the concentration measurement of a certain species of interest [122-123].

As the concentration / number density is inversely proportional to the temperature when the pressure is constant, absorption studies furthermore allow line-of-sight-averaged thermometry over a wide temperature range in a rather simple setup. By using more than one wavelength, i.e., by accessing ground states with different energies and thus temperature-dependent populations, thermometry without knowledge of the concentration is possible [1, 124]. However, the line-of-sight arrangement may prevent the spatial resolution of flow structures throughout the beam path. Tomographic methods have been investigated to overcome this problem [125].

An extension of this simple experimental approach is the measurement of the integrated absorbance connected with the line shape by tuneable excitation sources. The advantage is the increased accuracy of measured temperature and the measurement of pressure via pressure-induced line broadening. If diode lasers are used as excitation source, this method is called tuneable diode-laser absorption spectroscopy (TDLAS), see [1, 126] and references therein.

Two or more lasers can be used to realise a two- or multi-line measurement to enable single-pulse thermometry (see above). In this case, temperature-dependent population differences in the distinct vibrational or rotational modes are measured and temperature is derived similarly to the procedure with OH or NO as described above.

Rayleigh scattering

Photons can interact with molecules via scattering. Scattering always occurs, even if the photon energy is non-resonant with any allowed transition. The scattering probability, however, is much lower than any resonant luminescence. Thus, resulting signal intensities per molecule are much smaller than in LIF experiments. The more probable scattering process is elastic scattering, where the molecule returns into its original quantum state after the scattering process. This process is called Rayleigh scattering. Rayleigh scattering is always present and only depends on the number density of molecules (and thus the temperature) and the molecule-specific Rayleigh scattering cross-section. In fields with constant gas composition two-dimensional temperature imaging is possible, even with high temporal resolution if pulsed laser sources are used (e.g., [4, 127]).

Rayleigh cross-sections are well known from literature for many molecules. Thus, Rayleigh signals can be used to determine the detection efficiency of a detector in order to achieve absolute quantum yields of a tracer molecule (e.g., [93]).

As the detected wavelength is the same as the incident one, severe stray light problems may occur originating from windows, walls, or particles. Hence, filtered Rayleigh scattering techniques have been developed taking advantage of the different Doppler width of light reflected off walls and originating from the gas molecules (e.g., [128]).

Raman scattering

In contrast to Rayleigh scattering Raman scattering is an inelastic scattering process where the molecules return in a different rotational or vibrational quantum state after interaction with the incident photon. The emitted light can be red-shifted (Stokes lines) or blue-shifted (anti-Stokes lines) and is of low intensity compared to the Rayleigh signal. Raman diagnostics is mostly realised in spectrometer arrangement with one-dimensional spatial resolution. Recently, Greszik *et al.* demonstrated two-dimensional Raman scattering for measurements of water film thicknesses [129].

The spectral structure of the Raman signal is species-dependent. Thus, different species can in principle be detected simultaneously. The temperature of a species can be derived from relative intensities of the Raman lines by simulated Raman scattering [130].

Coherent Anti-Stokes Raman Scattering (CARS)

Coherent anti-Stokes Raman scattering (CARS) [2] is – in contrast to Rayleigh or Raman scattering – a nonlinear technique. Two laser beams are necessary for CARS. The difference between both laser frequencies must fit a Raman-active ground state vibrational/rotational transition frequency in the molecule [3]. For thermometry applications the most used probe species is N_2 because the available database is sufficient, the mole-

cule is stable, and a major species in many combustion experiments where air is used as the oxidiser.

As the signal originates from a non-linear process varying concentrations or excitation energies lead to severe signal fluctuations. Hence, the requirement on laser stability, beam quality, and laser alignment is much higher for CARS than for the other, linear techniques.

CARS only allows point or at most one-dimensional measurements due to controlled overlapping of two laser beams. The temperature measurement accuracy is very high and the resulting signal is strong. Thus, CARS measurements are often used to calibrate or validate other thermometry techniques. CARS thermometry has been demonstrated in gas turbine combustors [131], fuel injectors [132], and nanoparticle reactors [133]. Widespread applications, however, are often limited due to the high experimental complexity.

2.3.4 Multi-tracer diagnostics

In some applications it can be advantageous to use two tracers instead of one, especially when more than one quantity needs to be known. When using more than one tracer it is of great importance to quantify the interaction (i.e., energy transfer) between the tracer species after photon excitation, e.g., toluene is known to be quenched efficiently by 3-pentanone [134].

One often used approach is the combination of an aromatic tracer with a ketone with similar evaporation characteristics, e.g. toluene combined with 3-pentanone. As quenching of ketone fluorescence by O_2 is insignificant, its signal is assumed to represent the fuel concentration or temperature – depending on the measurement purpose. With known fuel concentration or temperature the ratio between the ketone and the aromatic signal delivers the fuel / air ratio. This techniques has been demonstrated for gas-flow mixing [134], in an optical engine [135], and in a close-to-production engine with endoscopic optical access [18, 136].

Another approach is the combined use of a single-ring aromatic combined with a double-ring aromatic. As both species exhibit different quantum yield dependences with temperature, the signal ratio is a function of temperature and can thus be used for thermometry [19]. Very recently, a combination of toluene and naphthalene as tracer species in combination with a three-colour detection strategy has been demonstrated for the simultaneous detection of temperature, fuel distribution, and O_2 concentration [137].

2.3.5 Diagnostics using the fluorescence lifetime

In all the techniques outlined before, time-integrated signal intensities are recorded to deduce the desired quantity. This procedure has the disadvantage that non-uniform species concentrations or intensity variations of the excitation source cause signal variations which may lead to misinterpretations and which need to be corrected for. In contrast, the fluorescence lifetime is independent on the excitation energy and the species concentration if the limits of the linear regime are not exceeded. Thus, information can be derived in, e.g., inhomogeneously seeded gas flows and / or with fluctuating excitation energy without loss of accuracy.

For time-resolved measurements the excitation must be pulsed and the pulse width must be negligible short compared to the fluorescence lifetime. If the pulse width is not negligible deconvolution algorithms have been developed to solve this problem within certain limits [77, 138]. The deduced fluorescence lifetime is proportional to the fluorescence quantum yield which on its part leads to the desired quantity of interest, like temperature or O_2 concentration.

Imaging diagnostics using the fluorescence lifetime cause more experimental effort. Beyond the short-pulsed excitation source imaging is restricted to one dimension with a streak camera [138] because in this case one spatial axis of the two-dimensional camera image is replaced by a time axis. Alternatively, at least two gated cameras are necessary for two-dimensional imaging [73, 75, 138]. In this case the lifetime can be extracted from the ratio between each pixel of both images.

The use of photomultiplier tubes restricts the measurement to a point-like spatial region, but the high sensitivity, the high temporal resolution, and the compact design opens up new diagnostic strategies. Besides thermometry in open flames [14], fibre-optic diagnostics inside an IC engine through an optical accessible spark plug are possible. The high sensitivity in combination with high repetition rate laser sources allow crank-angle resolved thermometry during an engine cycle [61-62].

In summary, diagnostics using the fluorescence lifetime of a molecular species are possible and show a great potential, but are so far seldom applied. On the one hand the experimental effort is often still too high, on the other hand the available database of fluorescence lifetimes is currently in many cases not sufficient.

3. Photophysics of small organic molecules

In laser-induced fluorescence (LIF), molecules are electronically excited by photon absorption typically in the UV/Vis region of light. Subsequent spontaneous emission (fluorescence) occurs usually on a timescale of about 1–200 ns. The bath gas has a strong influence on the non-radiative energy transfer processes in the excited state affecting the fluorescence quantum yield and the spectral distribution. Quantitative interpretation of measured signal intensities requires a detailed knowledge of the underlying photophysical processes which are described in this chapter [7, 139-140].

3.1 Excitation

3.1.1 Classification of electronic transitions

All molecules investigated here show absorption in the UV range. Photon absorption populates excited electronic levels. The wavelength-dependent absorption cross-section $\sigma(\lambda)$ represents the absorption strength. In organic molecules, chemical bonds are mostly described by linear combinations of atomic orbitals (LCAO), in this case, s- and p-orbitals. The LCAO results in orbitals with different symmetries: binding σ and π orbitals, non-binding n orbitals and anti-binding (repulsive) σ* and π* orbitals. The resulting typical optically-active transitions are:

- $\pi \rightarrow \pi^*$, e.g., in molecules with C=C double bonds or aromatic systems
- $n \rightarrow \pi^*$, e.g., in molecules with carbonyl groups
- $n \rightarrow \sigma^*$, e.g., in amines and alcohols
- $\sigma \rightarrow \sigma^*$, e.g., in saturated hydrocarbons

According to the photo-active group (chromophore) the molecules can be sorted into different classes. Typical properties of each class are shown in Table 3. For the tracers considered here some deviations can occur due to substituent effects. Therefore, the values must be taken as approximate.

Table 3: Wavelength of maximum absorptivity and maximum absorption cross section for relevant chromophores occurring in typical tracer species. Taken from [141].

Chromophore	Transition	λ_{max} (nm)	σ_{abs} (10^{-20} cm^2)
C=O	n → π*	280	8
mono-aromatic	π → π*	260	80
C=N	n → π*	240	50
C=C–C=C	π → π*	220	8×10^4
C=C	π → π*	180	4×10^4
C–C, C–H	σ → σ*	<180	400

3.1.2 Classification of excited electronic states

Electronic states of a molecule can be characterised by their degree of excitation and total spin. In most molecules in the ground state the total spin is $S = 0$. This is called a singlet state. Upon excitation of one electron the two resulting unpaired electron spins are either parallel ($S = 1$) or anti-parallel ($S = 0$). The first one is called triplet (T) state, the latter one singlet (S) state, corresponding to the resulting multiplicity of the states. In a singlet state, all electrons (each with $s = ½$) are paired with anti-parallel spin. An index indicates the level of excitation: 0 is the ground state, and 1, 2, 3, … are excited states with increasing energy. Figure 13 shows the electron distribution and energy levels for ground and excited states of a carbonyl group.

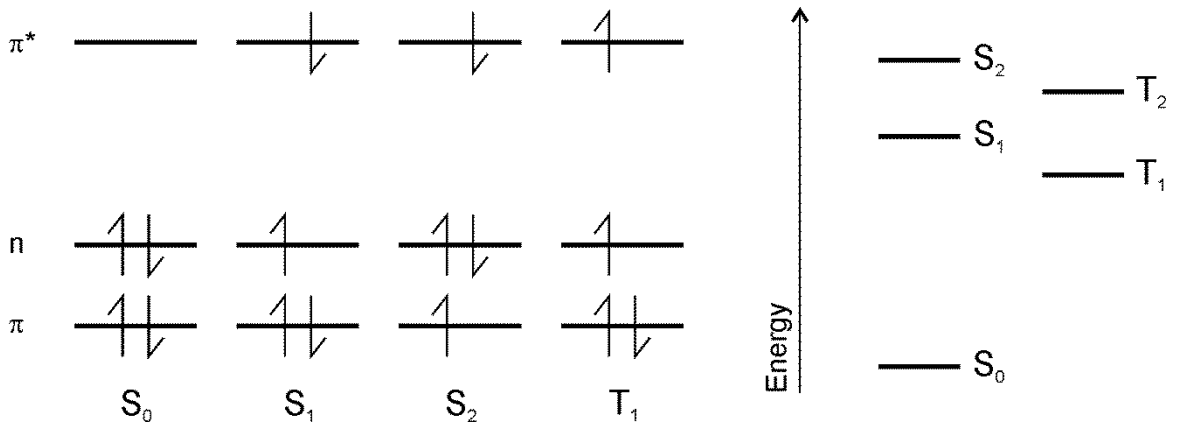

Figure 13: Electron population of molecular orbitals in the ground and first excited states in a carbonyl group (left) and relative energy of various states (right)

3.1.3 Transition probabilities

The photon absorption probability can be calculated using the time-dependent perturbation theory. The interaction with electromagnetic radiation is regarded as a short per-

turbation of the system. The time-dependent Schrödinger equation can be written as [140]

$$\hat{H}_{total} \cdot \psi = i\hbar \frac{\partial}{\partial t} \psi \tag{2}$$

with

$$\hat{H}_{total} = \hat{H}_0 + \hat{H}' \ . \tag{3}$$

$\hat{H}_{total}$ is the Hamiltonian of the total system, $\hat{H}_0$ the Hamiltonian of the unperturbed system, and $\hat{H}'$ the perturbation Hamiltonian representing the interaction of the electromagnetic field with the chromophore. The resulting wave function ψ is a linear combination of the initial (m) and the final (n) state of the respective transition.

$$\psi = a_m(t)\psi_m + a_n(t)\psi_n \ , \tag{4}$$

with the time-dependent coefficients a_m and a_n. The latter one corresponds to the probability that the transition has occurred. On a short timescale eq. 4 can be solved as

$$\frac{\partial}{\partial t} a_n = -\frac{1}{\hbar} \langle \psi_n | \hat{H}' | \psi_m \rangle \ . \tag{5}$$

The integral is called the transition matrix and is a measure for the coupling of the states to the electromagnetic field. With $\hat{H}' = pE$ as the interaction of the incident electromagnetic field with the total dipole p moment of the molecule eq. 5 can be solved to yield the transition probability of the transition $m \rightarrow n$, P_n:

$$P_n \approx \frac{E^2 |M_{nm}|^2}{\hbar^2} t^2 \ . \tag{6}$$

M_{nm} is the transition dipole moment with

$$M_{nm} = \langle \psi_n | p | \psi_m \rangle = \int \psi_n^* p \psi_m d\Gamma \ . \tag{7}$$

This is an integral over all spatial electron and nucleon coordinates. The transition dipole moment is transition-specific. The strength can be calculated using the Born-Oppenheimer approximation. In this approximation electron and nuclear motion is separated which is in most cases justified as nuclei are much heavier than electrons and thus much slower.

This leads to a molecular wave function $\psi = N\phi\chi$ which can be separated into the spatial electronic wave function ϕ, the nuclear wave function N and the electronic spin wave function χ. Development of the dipole operator leads to:

$$M_{nm} = \langle \phi_n | p | \phi_m \rangle \langle N_n | N_m \rangle \langle \chi_n | \chi_m \rangle \ . \tag{8}$$

As the transition probability is proportional to $|M_{nm}|^2$ its magnitude is determined by three factors:

- The spatial overlap and the symmetry of the respective electronic wave functions
- The spatial overlap of the nuclear wave functions (Franck-Condon factor)
- The spin wave function is zero for singlet-triplet transitions because of orthogonal wave functions and unity for singlet-singlet and triplet-triplet transitions

Combining of all three factors results in the selection rules of a transition. If the symmetry of wave functions of the ground and the excited state are different, the transition moment integral is zero and thus the transition is "symmetry-forbidden", which is the case for the S_0–S_1 transition in aromatics and ketones. In contrast to the selection rules, these molecules absorb light because the Born-Oppenheimer approximation is partly violated. Molecular vibrations couple with the electron system and break the perfect symmetry by distorting the electron wave functions. This introduces non-zero contributions to the integral, i.e., the resulting transitions are "vibrationally allowed". Increasing temperature or decreasing excitation wavelength enhances those transition moments. This effect explains why the $\pi \rightarrow \pi^*$ transition in aromatics is weaker by three orders of magnitude than the symmetry-allowed $\pi \rightarrow \pi^*$ transition in alkenes (cf., Table 3).

Singlet-triplet transitions should be non-existent because of the differences in the spin wave function mentioned above. In reality, however, the spin couples with the orbital's angular momentum and results in a non-orthogonal wave function of the total angular momentum. In typical organic molecules the coupling is very small, thus singlet-triplet transitions are very weak only. Heavy atoms in the molecule, however, increase significantly the spin-orbit coupling and thus enhance the singlet-triplet transition.

3.2 Deactivation of excited molecules

After excitation by a pulsed laser of suitable wavelength to meet the energy difference of an allowed transition, the molecule is promoted into an electronically excited state (cf., Figure 14). Each excited molecule tends to reach its ground state. The optically-introduced energy can be lost via chemical (dissociation or other photo-induced reactions) and physical processes. The following sections will focus on these physical processes. They can be divided into three categories: Radiative processes, where the excitation energy is fully or partly lost by spontaneous emission (e.g., fluorescence), non-radiative processes, where the energy is thermalised via vibrational and rotational energy transfer without emission of light, and collisional quenching, where the energy (or a part of it) is transferred to a collider species and the originally excited molecules return into the ground state without emission.

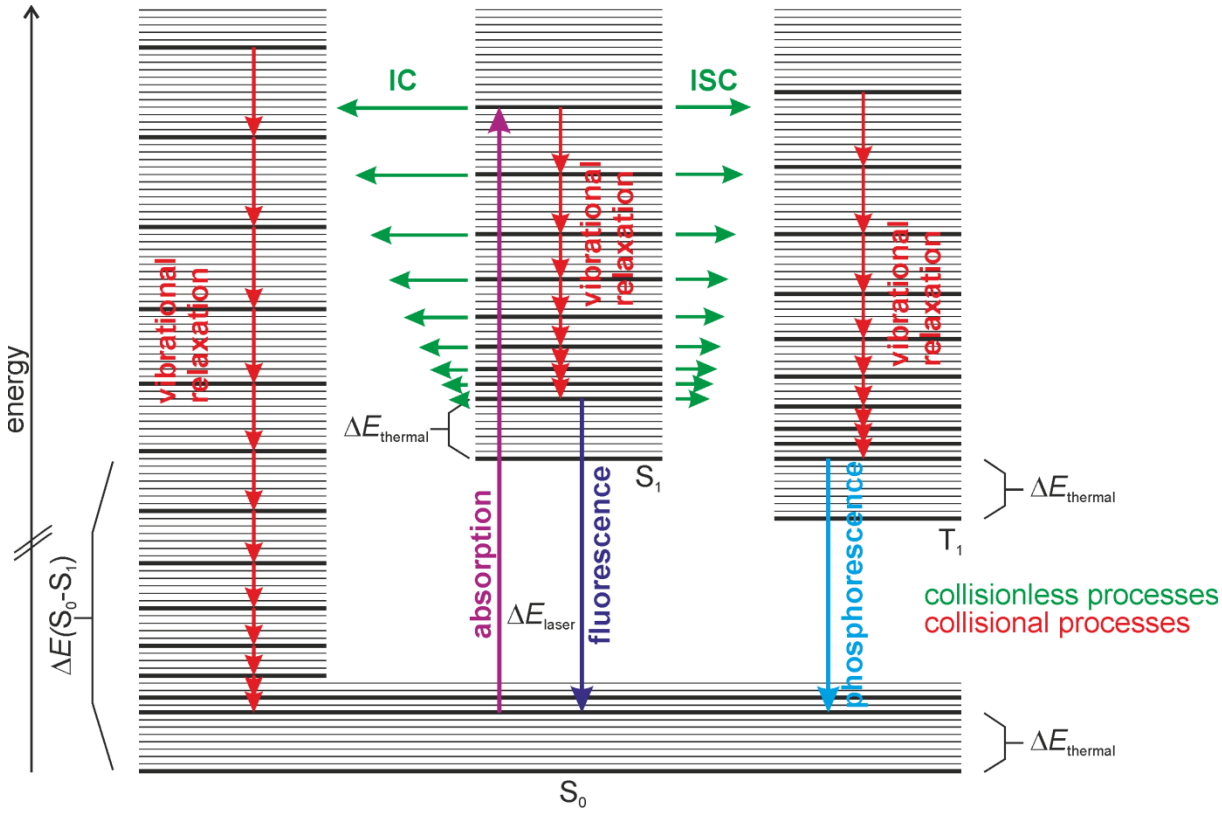

Figure 14: Schematic overview of photophysical processes in organic molecules (Jablonski diagram): Radiative processes (absorption, fluorescence, phosphorescence) and non-radiative processes (Inter System Crossing, ISC; Internal Conversion, IC; quenching processes) are marked by straight arrows. The horizontal arrow length indicates the relative respective rate constants. $\Delta E_{\text{thermal}}$ is the thermalisation level in each state.

In each electronic state a multitude of vibrational modes exist. The population distribution throughout these vibrational modes is temperature-dependent. The thermalisation level in each electronic state is the level where the mean distribution of the molecules in thermal equilibrium is located and can be calculated assuming a Boltzmann distribution, and using known energies of the main vibrational modes in the harmonic oscillator approximation. With increasing temperature the thermalisation level shifts to higher vibrational modes in each electronic state. Each molecule tends to reach this thermalisation level after disturbing the system, e.g., by absorption of a photon. Energy transfer processes between the vibrational modes allow the molecules to reach thermal equilibrium. This process is called vibrational redistribution (VR) and is promoted via collisions with other molecules, e.g., bath-gas molecules.

From each state along this vibrational cascade competing processes can occur: Radiative emission of photons (fluorescence), inter-system-crossing (ISC) to a triplet state, internal conversion (IC) into vibrationally highly excited modes of the ground state, and quenching processes with collider species. Contrary to the rate constants of fluorescence and quenching, ISC and IC strongly depend on the respective vibrational mode. Thus, increasing the rate of vibrational relaxation by, e.g., increasing the bath gas collision rate by a corresponding increase in pressure reduces the loss probability via ISC and IC and

thus enhances the fluorescence emission. Figure 15 (left panel) illustrates these processes.

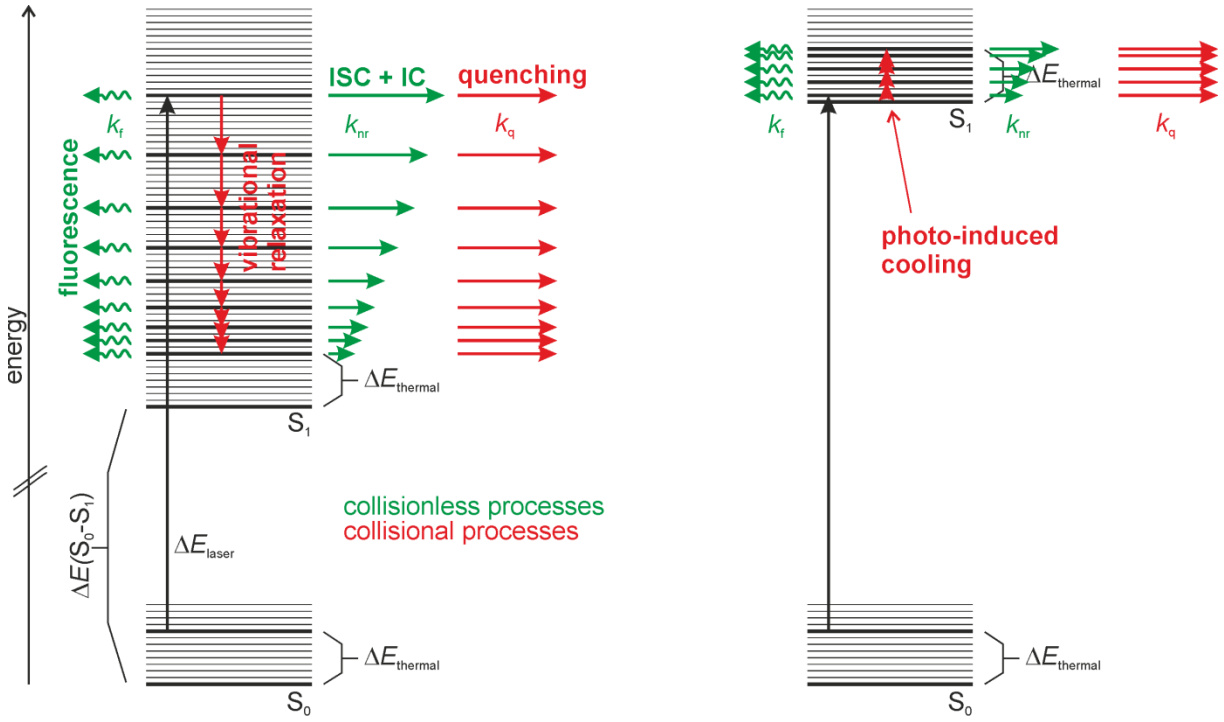

Figure 15: Schematic overview of the photophysical processes in organic molecules (extracted from [31] and references therein): Radiative processes (fluorescence) are symbolised by wavy arrows, non-radiative processes (Inter System Crossing, ISC; Internal Conversion, IC; quenching processes) by straight arrows. The horizontal arrow length indicates the relative rate constants. $\Delta E_{thermal}$ is the thermalisation level in each state. The figure displays two different cases of molecules distinguished by their S_0-S_1 energy gap and using the same excitation wavelength. Triplets or highly excited vibrational modes from S_0 (cf., Figure 14) are not shown. See text for details.

In the paragraph above the case was discussed in which photo-excitation leads to a population in the S_1 state that is above the thermalisation level. Figure 15 (right panel) illustrates a case where the absorption ends in vibrational modes below the mean thermalisation level. In this case, the vibrational relaxation cascade induced by bath gas collisions goes upwards towards the mean thermalisation level. As this process is accompanied by energy transfer from bath gas molecules to the excited species this is called photo-induced cooling [31]. The decision if "normal" vibrational relaxation or photo-induced cooling occurs depends on the S_0–S_1 energy gap and on the excitation wavelength. In the following paragraphs all the processes mentioned above will be introduced.

Spontaneous emission of photons depends on the same selection rules as for absorption. The energy difference between the coupled states, however, enhances the probability of spontaneous emission by the third power of the frequency. The emission from the S_1 state is called fluorescence. As a fast process typical lifetimes are in the range 1–100 ns. Radiative emission from triplet states occurs, although this is a spin-forbidden process.

This emission is called phosphorescence and typically ranges at a timescale between ms and s.

Inter-system crossing (ISC) is the non-radiative process between states of different spin multiplicity. Most important here is the transition from S_1 to T_1. ISC can be allowed ($S(n,\pi^*)\rightarrow T(\pi,\pi^*)$, $S(\pi,\pi^*)\rightarrow T(n,\pi^*)$) or forbidden ($S(n,\pi^*)\rightarrow T(n,\pi^*)$, $S(\pi,\pi^*)\rightarrow T(\pi,\pi^*)$). The rates of forbidden transitions are not zero, but much lower than the rates for allowed transitions. Table 4 gives an overview of typical ISC rate constants for different transitions.

Table 4: ISC rates for molecules with similar singlet-triplet gaps (24-80 kJ/mol) but different symmetries [66, 142-143]

Molecule	Transition	Selection rule	ISC rate [10^8 s^{-1}]
Naphthalene	$S_1(\pi,\pi^*)\rightarrow T(\pi,\pi^*)$	"forbidden"	0.1
Acetone	$S_1(n,\pi^*)\rightarrow T(n,\pi^*)$	"forbidden"	5
Benzophenone	$S_1(n,\pi^*)\rightarrow T(\pi,\pi^*)$	"allowed"	1000

Although ISC is symmetry forbidden for typical aromatics and ketones, its rate is 1 and 3 orders of magnitude faster than the fluorescence rate, respectively. In the presence of certain collider species like, e.g., O_2 the rate can be significantly increased. This will be discussed in section 3.3. The rate of ISC is also dependent on the vibrational level, normally increasing with vibrational excess energy.

Internal conversion (IC) is a non-radiative transition between states of the same spin multiplicity. For large energy gaps, as between S_1 and S_0, IC is of minor importance. At high vibrational excess in the S_1 state certain vibrational modes can promote IC leading to high losses in fluorescence emission. This is important for elevated temperatures.

Vibrational relaxation (VR) occurs with high efficiency via collisions with bath gas molecules. In the gas phase VR does not fully relax the molecules to the thermalisation level in the S_1 state during the fluorescence lifetime and proceeds on the same timescale as competing processes, such as ISC and fluorescence.

3.2.1 Quantum yield and fluorescence lifetime

In this chapter, the kinetics of the relevant photophysical processes are derived. The resulting equations are essential for photophysical modelling (cf., chapter 3.4) and prove the proportionality of fluorescence quantum yield and the effective fluorescence lifetime.

For simplification the presence of only one excited singlet state S_1 is assumed, and radiative processes coming from triplet states are ignored. Radiationless transitions from higher lying singlet states are usually much faster than the fluorescence coming from

these states. Thus, fluorescence emission only occurs from S_1. This is known as Kasha's rule which says that the non-radiative transfer rates depend on the energy gap between the involved electronic states. The energy gap between S_0 and S_1 is much larger than between the higher excited singlets and S_1. Therefore, the cascade of non-radiative deactivation ends at E_{thermal} in S_1. In the following paragraphs the duration of excitation is assumed to be negligibly short relative to the timescale of the processes mentioned in this chapter.

If fluorescence emission was the only deactivation pathway from the excited state to the ground state, the temporal development of the concentration of excited molecules [M*] can be described as follows:

$$-\frac{d}{dt}\left[M^*\right] = k_{fl}\left[M^*\right], \tag{9}$$

with the fluorescence rate k_{fl} (in s^{-1}). This leads to an exponential decay with the initial concentration $[M^*]_0$.

$$\left[M^*\right] = \left[M^*\right]_0 \cdot \exp\left(-k_{fl}t\right) \tag{10}$$

The radiative lifetime τ_{rad} is the time when the concentration has decayed to $1/e$ of its initial value:

$$\tau_{rad} = \frac{1}{k_{fl}} \ . \tag{11}$$

In real systems, fluorescence is not the only deactivation pathway. IC and ISC as non-radiative intra-molecular processes always occur simultaneously. The intra-molecular deactivation of the excited molecules [M*] can then be described by the following rate equation.

$$-\frac{d}{dt}\left[M^*\right] = \left(k_{fl} + k_{ISC} + k_{IC}\right)\left[M^*\right], \tag{12}$$

where k_{fl}, k_{ISC}, k_{IC} are the rates (all in s^{-1}) of fluorescence emission, intersystem crossing, and internal conversion, respectively. The total depopulation rate, k_{tot}, is then connected to the experimentally accessible effective fluorescence lifetime, τ_{eff}, via the following relation:

$$k_{tot} = \sum k_i = k_{fl} + k_{nr} = k_{fl} + k_{IC} + k_{ISC} = \frac{1}{\tau_{eff}}, \tag{13}$$

where k_{nr} is the non-radiative decay rate (s^{-1}) as the sum of all decay rates except k_{fl}.

The fluorescence quantum yield ϕ_{fl} is the fraction of the number of molecules having absorbed a photon and emitting fluorescence radiation. If no non-radiative deactivation

processes occurred, ϕ_{fl} would be unity. It can also be expressed as the ratio of the fluorescence and the absorption rate.

$$\phi_{fl} = \frac{k_{fl}[M^*]}{k_{abs}[M][h\nu]} , \tag{14}$$

where $[h\nu]$ is the number of photons. Using $k_{nr} = k_{tot} - k_{fl}$, the temporal variation of the concentration of $[M^*]$,

$$\frac{d}{dt}[M^*] = k_{abs}[M][h\nu] - \left(k_{fl}[M^*] + k_{nr}[M^*]\right) , \tag{15}$$

with the steady-state assumption d/dt[M*]=0 eq. 15 yields eq.16

$$[M^*] = \frac{k_{abs}[M][h\nu]}{k_{fl} + k_{tot}} . \tag{16}$$

A substitution of $[M^*]$ leads to

$$\phi_{fl} = \frac{k_{fl}}{k_{tot}} = \frac{\tau_{eff}}{\tau_{rad}} , \tag{17}$$

as the expression of the fluorescence quantum yield. Thus, the fluorescence quantum yield is proportional to the effective fluorescence lifetime. On the other hand, if the quantum yield is known, it is possible to calculate the non-radiative decay rate, k_{nr}. In the following, the effective fluorescence lifetime τ_{eff} will be handled as a relative quantum yield ϕ_{rel}.

3.3 Collisional Quenching

In the section before the non-radiative processes that reduce the fluorescence quantum yield were intra-molecular. Collisions with bath-gas molecules lead to intermolecular deactivation/energy redistribution whose rates depend on the nature of the collider species and their concentration (i.e., collision rates). In the subsequent paragraphs quenching mechanisms are discussed, and the quenching kinetics with its effects on the quantum yield (and thus the fluorescence lifetime) are presented.

3.3.1 Quenching processes

Electronic energy transfer is one of the most important processes responsible for collisional quenching in organic molecules. The colliding species Q can be excited during the collision with the excited chromophore. Alternatively, the quencher species assimilates the energy by enhancing its translational or – more seldom – rotational or vibrational energy. In the context of energy transfer, M is often called donor, Q acceptor.

$M^* + Q \rightarrow M + Q^*$

The simplest transfer type is an emission of a photon by M* with subsequent absorption by Q. This is called radiative energy transfer. In contrast to non-radiative processes, however, radiative energy transfer is often much less efficient.

The first type of non-radiative energy transfer is the fluorescence resonance energy transfer (FRET, sometimes also Förster (resonance energy) transfer) first described by Förster [144]. In this case the electronic structure is distorted by dipole-dipole interactions. Dipole oscillations of M* induce oscillations in Q. Direct physical contact is not necessary, but the interaction strength depends strongly on the distance between the molecules. Energy transfer over several molecule diameters (up to ~10 nm) is possible. The energy transfer probability dP_n within a time interval dt can be described as follows [144]:

$$dP_n = \frac{1}{\tau_{eff}} \left(\frac{r_0}{r} \right)^6 dt \tag{18}$$

The "critical radius" r_0 is a measure for the strength of interaction and depends on the spectral overlap between the emission spectrum of M* and the absorption spectrum of Q. As in this type of energy transfer electrons are not exchanged between the molecules the spin selection rules mentioned in subsection 3.1 must be satisfied. Therefore, possible processes are:

$^1M^* + {}^1Q \rightarrow {}^1M + {}^1Q^*$

$^1M^* + {}^3Q \rightarrow {}^1M + {}^3Q^*$

A different type of energy transfer mechanism was first describes by Dexter [145] (sometimes called Dexter (energy) transfer) in which an electron is exchanged between the two molecules. A direct physical contact is necessary leading to spatial overlap of different molecular orbitals. Thus the maximum distance is typically in the range 0.5–1 nm. Again the spectral overlap determines the probability of the process. Selection rules, however, do not occur. Therefore, following processes are possible:

$^1M^* + {}^1Q \rightarrow {}^1M + {}^1Q^*$

$^1M^* + {}^1Q \rightarrow {}^1M + {}^3Q^*$

In contrast to most other molecules the ground state of molecular oxygen is a triplet state. Fluorescence from organic molecules can therefore efficiently be quenched by promoting transitions into triplet states. The following energy transfer reactions are assumed [146]:

$$^1M^* + {}^3O_2 \leftrightarrow {}^3(M,O_2)^* \rightarrow \quad {}^3M + {}^1O_2^*$$

$$\qquad\qquad\qquad\qquad\qquad\quad {}^3M + {}^3O_2$$

When the organic molecule collides with molecular oxygen, a short-lived exciplex as transition state is formed. Different states within the exciplex with localised excitation and charge transfer structure are possible. Intersystem crossing is enabled because in this exciplex states with different spin multiplicity are coupled. When the ionisation potential of the molecule increases quenching coefficients decrease. This indicates that at least partly charge transfer complexes are involved in the transition state [147]. The quenching process can only occur if the singlet-triplet energy gap in M is larger than the excitation energy required to promote O_2 into its singlet state (360 kJ/mol, 0.98 eV). In aromatic molecules this condition is fulfilled, but not in ketones. Thus, aromatic fluorescence is strongly quenched by O_2, ketone fluorescence usually only weakly. The mechanism shown above describes well the effects of collisional quenching in aromatics [148].

3.3.2 Stern-Volmer relation

When including collisional quenching processes, the equation for the fluorescence quantum yield has to be expanded in the denominator by a new quenching term:

$$\phi_{fl} = \frac{k_{fl}}{k_{tot} + \tilde{k}_q n_q} \quad . \tag{19}$$

The fluorescence quenching probability is proportional to the collision rate times a species-specific quenching cross-section. Practically, this is expressed by the number density of the quencher, n_q, and a rate coefficient (in m^3/s) $\tilde{k}_q$. It becomes a rate by multiplying with the number density.

If the quenching term is dominant, ϕ_{fl} is inversely proportional to the quencher concentration. In each case it must be checked if this assumption is fulfilled. For O_2 quenching on aromatics this assumption is valid in most cases. The signal variation with increasing quencher concentration can then be written as [149]:

$$\frac{S_{fl}^0}{S_{fl}} = \frac{k_{fl}}{k_{tot}} \frac{k_{tot} + \tilde{k}_q n_q}{k_{fl}} = 1 + \frac{\tilde{k}_q}{k_{tot}} n_q \quad . \tag{20}$$

S_{fl}^0 is the fluorescence intensity (proportional to quantum yield and lifetime, respectively) in the absence of quencher species. The ratio $\tilde{k}_q / k_{tot}$ is the so called Stern-Volmer coefficient, k_{SV}, with

$$k_{SV} = \frac{\tilde{k}_q}{k_{tot}} = \tilde{k}_q \tau_{eff} \quad . \tag{21}$$

k_{SV} (in m^3) indicates the strength of fluorescence quenching and is thus experimentally important. It can be determined by measuring fluorescence intensities at varying quencher concentrations, with temperature and total pressure kept constant. This rela-

tion can graphically be represented by the so-called Stern-Volmer plot (cf., Figure 16). In many cases Stern-Volmer coefficients are temperature-dependent.

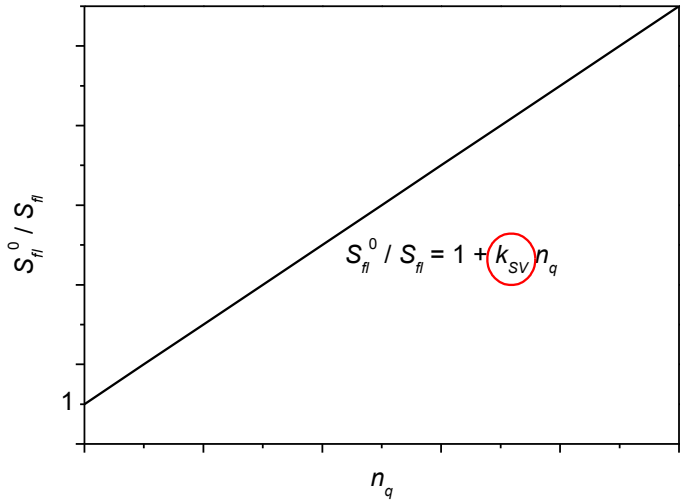

Figure 16: Example for a Stern-Volmer plot. The ratio between the signal without quencher and the signal with actual quencher number density is plotted against the number density of the quencher. The linear slope is then the Stern-Volmer coefficient.

In practical applications it is easier to use Stern-Volmer coefficients depending on the quencher partial pressure instead of the quencher number density. In this case the dimension of the Stern-Volmer coefficient changes to bar^{-1} with a temperature-dependent conversion factor of $1.3791 \cdot 10^{-28} \cdot T$.

3.4 Photophysical models

The prediction of fluorescence intensities or quantum yields for given environmental conditions can be done in two different ways: On the one hand, functional fits to experimental data (Figure 3, Figure 4) deliver the necessary information. However, this procedure is strictly limited to the range of conditions, where the fit functions applied for. The generally rather simple fit functions allow an analysis of experimental data with low computational effort. These models are inconsistently named in literature as phenomenological or empirical models, or – to distinguish from the photophysical models described in the following paragraph – model functions or parameterised fitting functions.

On the other hand – and this is much more challenging – real photophysical models can be created. They consider in detail the energy transfer processes taking place in each vibronic level in the excited state(s). If accurate enough, these models help to understand photophysical processes and deliver as by-product the same quantum yield information as the empirical models. As advantage, their applicability may not be limited to condi-

tions where the model was validated but can be extended to experimentally unexplored temperature and pressure conditions.

3.4.1 Phenomenological model for toluene

Koban *et al.* [29] set up a phenomenological model for predicting toluene-LIF signal intensities, i.e., fluorescence quantum yields, as a function of excitation wavelength, λ_{exc}, temperature, T, and O_2 number density, n_{O2}, relative to a calibration at known conditions based on the simplifications mentioned in chapter 3.2. The model was validated against experimental data obtained in a cell at 1 bar total pressure for temperatures between 300 and 950 K in pure N_2, and between 300 and 700 K in the presence of 0 – 300 mbar O_2. According to Eq. (17), after a proper calibration the model should equally be applicable to the present lifetime measurements. As outlined in [29, 52], the model describes the time-integrated LIF-signal intensity (cf., eq. (22)) as being proportional to two factors:

$$I_{LIF}\left(T,\lambda_{exc},n_{O_2}\right)\propto n_{tol}\sigma_{abs}(T)\cdot\left(\frac{A_1(T,\lambda_{exc})}{1+k_{SV,1}(T)\cdot n_{O_2}}+\frac{A_2(T,\lambda_{exc})}{1+k_{SV,2}(T)\cdot n_{O_2}}\right) \tag{22}$$

The first part considers the number density, n_{tol}, of toluene and the temperature dependence of the absorption cross-section, σ_{abs}, which is necessary to predict signal intensities as a function of temperature. However, since the variations of the absorption cross-section are not part of the calculation of the fluorescence quantum yield, it needs not be taken into account for comparison to the lifetime measurements presented in this thesis. The second factor describes the relative quantum yield as a function of temperature and O_2 partial pressure. It considers two separate de-excitation pathways for molecules excited to the S_1 state, represented by two separate Stern-Volmer factors [29]. This form, however, is just an empirical form without a clear photophysical background. A shortcoming of the model is that it does not consider effects of total pressure in, e.g., N_2 as bath gas.

3.4.2 Step-ladder models

The first widely-used step-ladder type fluorescence model for organic molecules was introduced by Thurber *et al.* [28] for acetone. It is based on the theoretical description outlined by Freed and Heller [150] and preliminary studies by, e.g., Wilson *et al.* [151] and Yuen *et al.* [152]. Although still some simplifications were made the general approach was visible. Koch generalised the model by considering oxygen quenching and also being able to model 3-pentanone quantum yields [30]. In the following years, the model was optimised by several authors for specific applications [88, 103, 153], with the latest optimisation presented by Cheung and Hanson [85].

For simplification, in this model only the thermal average of the vibrational energy distribution in the S_1 state is considered. After photon absorption the vibrational energy E_1 in the S_1 state is given by:

$$E_1 = \frac{10^7}{\lambda} + E_{thermal} - E_{0-0} \tag{23}$$

with λ as excitation wavelength in nm, E_{0-0} the energy gap between the S_0 and the S_1 state in cm^{-1}, and $E_{thermal}$ (in cm^{-1}) the thermal vibrational energy. As outlined in chapter 3.2, along the vibrational cascade each molecule can undergo fluorescence emission or non-radiative processes (cf., Figure 14 and Figure 15). Thus the total fluorescence quantum yield can be described in a simplified way as the sum of individual quantum yields from each energy state:

$$\phi = \sum_n \phi_n = \sum_n \frac{k_{f,n}}{\sum_i k_{i,n}} \ , \tag{24}$$

where n is the given energy level in S_1, and i the respective deactivation channel available from level n. Written explicitly, this equation yields [30]

$$\begin{aligned} \phi = & \frac{k_f}{k_f + k_{vib} + k_{ox}[O_2] + k_{nr,1}} \\ & + \sum_{i=2}^{N-1} \left[\frac{k_f}{k_f + k_{vib} + k_{ox}[O_2] + k_{nr,i}} \prod_{j=1}^{i-1} \left(\frac{k_{vib}}{k_f + k_{vib} + k_{ox}[O_2] + k_{nr,j}} \right) \right] , \\ & + \frac{k_f}{k_f + k_{ox}[O_2] + k_{nr,N}} \prod_{j=1}^{N-1} \left(\frac{k_{vib}}{k_f + k_{vib} + k_{ox}[O_2] + k_{nr,j}} \right) \end{aligned} \tag{25}$$

where the sum starts at the initially excited energy level 1 and proceeds along the vibrational cascade downwards to the thermalisation level N. For each state the fluorescence probability is summed and multiplied with the probability to reach this state (except for the initial state). k_{nr} is the sum of the rates for inter-system-crossing k_{ISC} and for internal conversion k_{IC}. As in the case of modelling the quantum yield ISC and IC lead to the same effect, namely non-radiative deactivation of the excited molecule, this simplification is justified.

The vibrational relaxation rate k_{vib} is calculated as the sum of collisions of the excited species with all surrounding collider species [154].

$$k_{vib} = \sum_{m=1}^{M} Z_{coll,m} n_m \ , \tag{26}$$

where $Z_{coll,m}$ is the collision frequency factor (in $cm^3\ s^{-1}$) between the ketone and the respective species m. It is calculated using the Lennard-Jones collision theory with approximations given in [155]. If the excited molecule undergoes vibrational relaxation, this can be described by:

$$E_{n+1} = E_n - \Delta E_{coll} = E_n - \alpha\left(E_n - E_{thermal}\right) . \tag{27}$$

α is called the vibration cascade parameter. α is temperature dependent [30]. In the presence of different collider species, α must be calculated as a weighted average of the species-specific cascade parameters α_m:

$$\alpha = \frac{1}{k_{vib}} \sum_{m=1}^{M} \alpha_m Z_{coll,m} n_m \quad . \tag{28}$$

Recently, Cheung and Hanson introduced an additional new rate, the quenching rate for collisions with N_2 [85], leading to more accurate results when compared to measured quantum yields. Furthermore, the specific rates were slightly modified. The general concept of the model, however, was not changed. One simplification is the fact that the direction in the vibrational cascade is strictly downwards, which works well for ketones.

As this approach of modelling was very successful in predicting quantum yields of ketones, Rossow [31] transferred this model structure to the aromatics toluene and naphthalene. Therefore, the idea is the same, the rates and collision frequencies, however, must be adjusted. Additionally, the severe quenching by O_2 leads to a new formulation of k_{ox}. While the model works quite convincing when predicting naphthalene quantum yields for a large range of environmental conditions, it fails for toluene at elevated pressures. The pressure-induced cooling effect (cf., chapter 3.2) taking place in excited state toluene is not taken into account by this model structure as it would need upwards steps in the vibrational cascade.

4. Experiment and data evaluation

4.1 High-temperature high-pressure cell

A static cell with optical access is a suitable means for studying the photophysical properties of tracer molecules under the desired well-defined conditions of temperature, pressure, and bath gas composition (e.g., [107, 110]). However, long residence times can cause degradation of the organic species due to pyrolysis, wall-catalysed reactions, or photolysis. This risk can be reduced by slowly flowing the sample gas mixture through the cell. In literature, cells for this purpose are mostly made of stainless-steel and heated resistively from outside, which limits the maximum attainable temperature to below 900 K if simultaneously elevated gas pressures are applied (e.g., [30, 47, 63, 103]). Cells made from ceramic materials can withstand much higher temperatures, are corrosion resistant and exhibit low catalytic activity, however, due to their fragility, measurements are often limited to atmospheric pressure [13, 156]. Another method for reaching simultaneously high temperature and pressure conditions is the shock tube, in which an incident and reflected shock wave almost instantly transforms a gas mixture to a well-defined thermodynamic state in the test section of the tube. The short exposure time to the desired temperature and pressure conditions reduces material demands, but the resulting measurement time is limited to just a few milliseconds with an extremely low duty cycle of a few measurements per day ([50] and references therein).

The cell used in this work combines the advantages of both concepts: Firstly, the gases are forced to flow through a cell made from alumina ceramics allowing high temperatures to be achieved, and secondly this cell is placed inside a thermally insulated stainless-steel cylinder allowing high pressures.

4.1.1 Design of the cell

A schematic drawing of the current pressure vessel including the internal flow cell is shown in Figure 17. The instrument was initially designed for LIF studies of NO and CO [157] and is presently configured for measurements with vaporised organic tracer species.

Gas mixtures of interest can be continuously flown through an externally heated cylindrical ceramic flow chamber placed inside a 400 mm diameter stainless-steel vessel. As shown in Figure 17 the flow cell consists of two concentric ceramic cylinders, each having four circular wall openings at half height and separated by 90°, which for optical access from outside are arranged in line with four optical window ports of the outer pressure vessel. The four optical ports of the outer pressure vessel are fitted with quartz windows (30 mm clear aperture). Four meander-shaped ceramic heating elements ($MoSi_2$ / SiO_2 coated, 3 mm diameter, Schupp-Ceramics, Germany), are fixed on the inner wall of four

bored half cylinders (inner diameter 150 mm, wall thickness 75 mm, 125 mm high) made of ceramic fibre thermal insulation material. Each of these units is placed around the flow chamber above and below the plane containing the optical ports. Most of the interior of the pressure vessel is filled with thermal insulation material except for tubes along the optical view ports and a 50 mm high section at the top reserved for electrical connections. The heating elements are connected to pressure tight electrical feedthroughs (Hositrad) by short sections of flexible aluminium ribbon. The heating current is regulated by a thyristor-based phase-sensitive current regulator (Eurotherm, combined with home-made electronics), and is controlled by an R-type thermocouple (PtRh/Pt) placed near the heating elements. The gas temperature in the flow chamber is measured with a second R-type thermocouple located on the centreline of the inner flow chamber shortly above the viewport holes. The cell is designed for temperatures and pressures up to 1400 K and 10 bar, respectively.

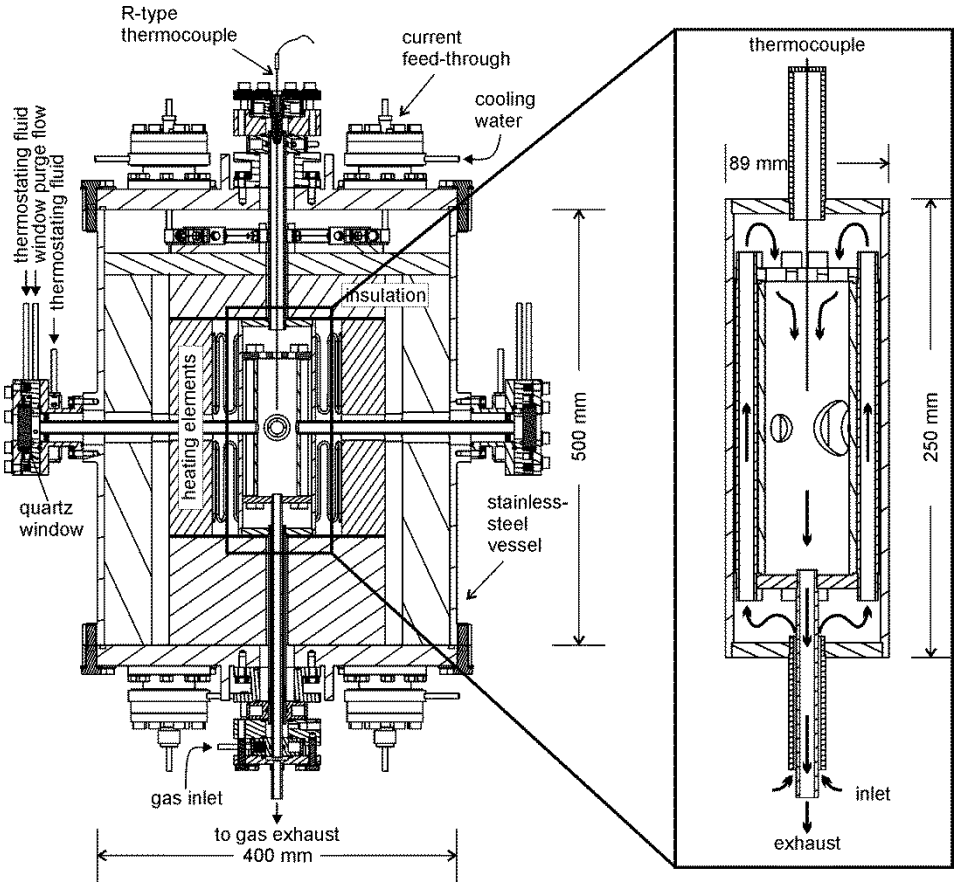

Figure 17: Schematic cut through the centre plane of the high-pressure vessel (left panel) with the high-temperature flow cell mounted in the centre (right panel). See text for more details.

Gas mixing

As shown in Figure 17 (right panel) gases are supplied to the concentric flow cells through the outer of two concentric ceramic tubes fed through the bottom flange of the

pressure vessel. The gases first enter the lower mixing chamber formed between outer and inner ceramic cylinders where the gas flow is preheated and directed through eight ceramic tubes into the upper chamber, before they enter the inner (measurement) chamber through seven holes in its top end plate (cf., Figure 17), after which it exits the pressure vessel through the inner ceramic tube. From all windows a weak purge flow is applied through respective ceramic tubes connected with the inner flow cell to minimise diffusion of the gas mixture into dead volumes of the pressure vessel. Figure 18 shows an overview over the gas supply system of the cell.

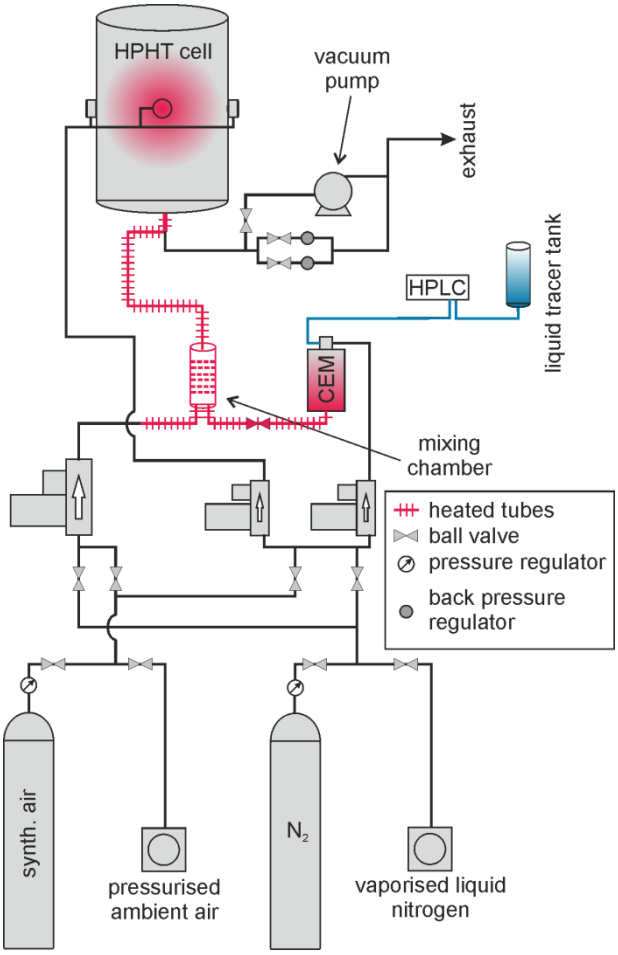

Figure 18: Schematic view of the gas supply for the high-pressure high temperature cell. A CO_2 gas cylinder is installed as required instead of the N_2 or air cylinder. For details see text.

Different organic tracer species (liquid at ambient conditions) can be stored in a cylindrical borosilicate glass tank (QVF, filling volume 200 ml, wall thickness 5 mm) PTFE sealed to stainless steel endplates and connected to a HPLC pump (HPLC Compact Pump 2250, Bischoff-Chrom). From there, the flow is pressurised to 25 bar and metered into a CEM (Controlled Evaporation and Mixing, Bronkhorst) system, where it is mixed with a part of the main carrier gas. Subsequently, different gas compositions can be realised via additional supply lines each equipped with suitable mass flow controllers (Bronkhorst) before the gas flow passes through a small gas mixing chamber into the

pressure vessel. To avoid condensation the marked tubes in Figure 18 were resistively heated to 470 K. The total flow rate is kept between 2 and 20 SLM (standard litres per minute). This corresponds to a residence time in the range of 1–5 s in the hot zone of the cell. Flow velocities are thus in the range 2–10 cm/s. Elevated pressures are realised with two back-pressure regulators (Hoke, 1–6 bar, and 2–10 bar, respectively) situated between the exit of the cell and the exhaust line.

Carrier gases are provided either from gas cylinders (purity 4.6 or 5.0) or the laboratory gas supply delivering vaporised liquid nitrogen or compressed and dried air, respectively. A membrane vacuum pump is installed to support gas exchange and cleaning from impurities when changing bath gases. The outside wall of the pressure vessel and the window flanges can be heated up to about 370 K to avoid tracer condensation on the vessel walls or windows.

4.1.2 Temperature distribution and gas-flow characterisation

Although the cell was already used and characterised concerning temperature reliability and absorption effects during a diploma thesis [157], a new characterisation was required because several reconstructions were done in the meantime and the cell is now operated with vaporised liquids instead of gases as done before.

Temperature distribution and flow characteristics

Due to the rather complex geometry of the flow system, CFD (Computational Fluid Dynamics) calculations were performed in collaboration with L. Deng and I. Wlokas (Chair for Fluid Dynamics at IVG, University of Duisburg-Essen) to analyse temperature distributions and flow characteristics within the ceramic flow cell [158].

The computational domain which also included the cell body was discretised using a hex-core mesh. Due to the complexity of the geometry, it was found to be the best solution in order to keep the meshing procedure at a reasonable effort. An estimation of the flow characteristics by dimensional analysis showed also that a uniformly spaced grid would be sufficient to describe the laminar flow field. Areas of very low Reynolds numbers are filled with a coarser mesh.

Results of the CFD calculations will be shown here exemplarily representative for a typical operating condition of the flow cell with a volumetric gas flow of 5 SLM at $T = 500$ K and 3 bar total pressure. Figure 19 shows the gas velocity in the central cross sectional plane as shown in Figure 17 and the wake flow zones in the upper mixing chamber. Clearly visible is the accelerated flow upwards through the ceramic guiding tubes connecting the lower and upper mixing chamber between inner and outer flow cell and the dead volumes of low circulation located next to the inflow in the upper mixing chamber. Main wake flow locations are identified (see insets in the right panels) next to the inflow

in the upper mixing chamber and in the top of the main chamber behind the circularly arranged inlet holes around the centreline. The length of this separation zone should be kept as short as possible to minimise negative effects of the flow in the probe volume which is located in the centre of the measurement cell.

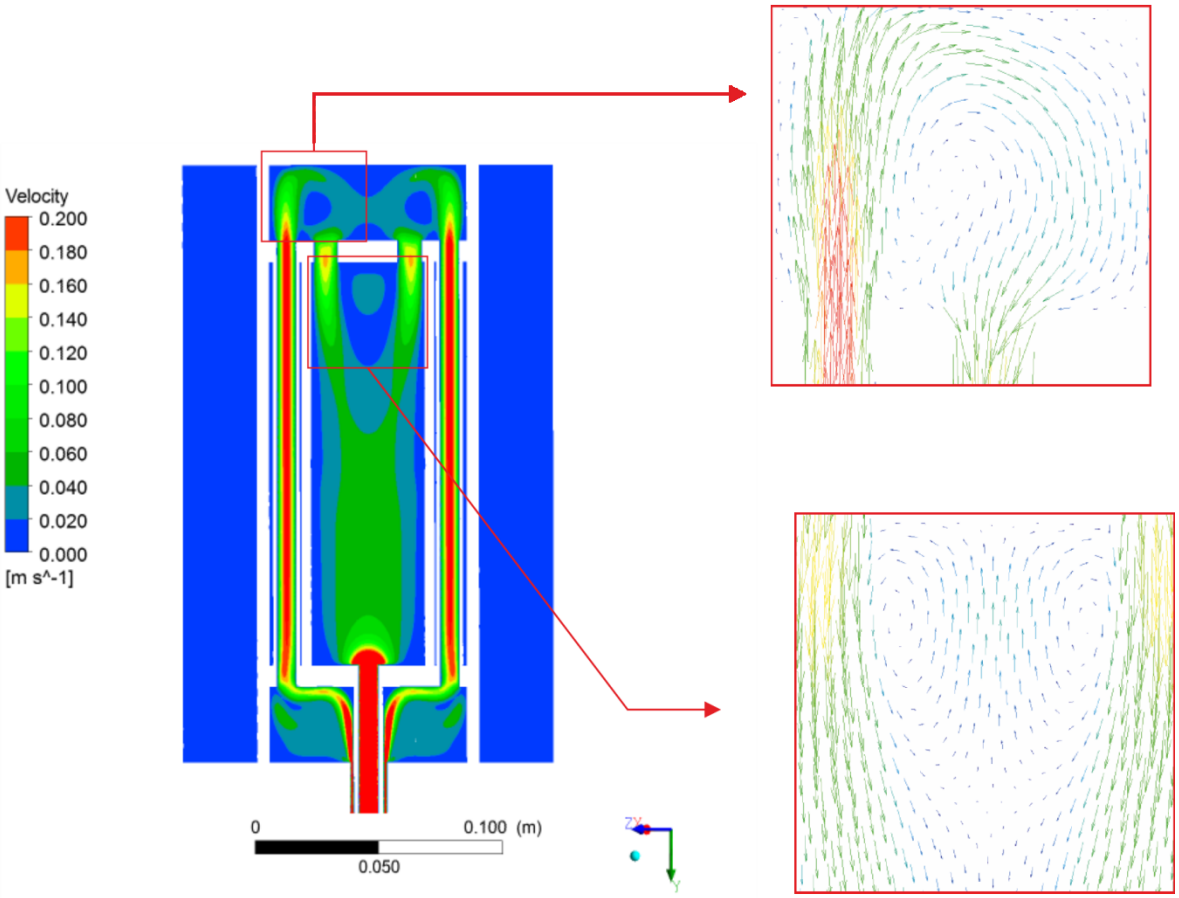

Figure 19: Flow velocity map for 3 bar and a gas flow of 5 SLM at 500 K. Wake zones are enlarged (taken from [158]).

Of high importance for the experimental work conducted with the present equipment is the knowledge about the conductive heat flux between the solid vessel components and the gaseous flow passing between the inlet and outlet ports. Therefore, the temperature distribution in the same plane already shown for the velocity field was of interest and is depicted in Figure 20. It is observed that for the present flow conditions the temperature inside the inner flow cell, i.e., the LIF measurement volume, is equal to the desired set temperature, and that, except for the region within the lower settling chamber and in the inflow regions of the flow guiding ceramic tubes, the temperature distribution is homogeneous.

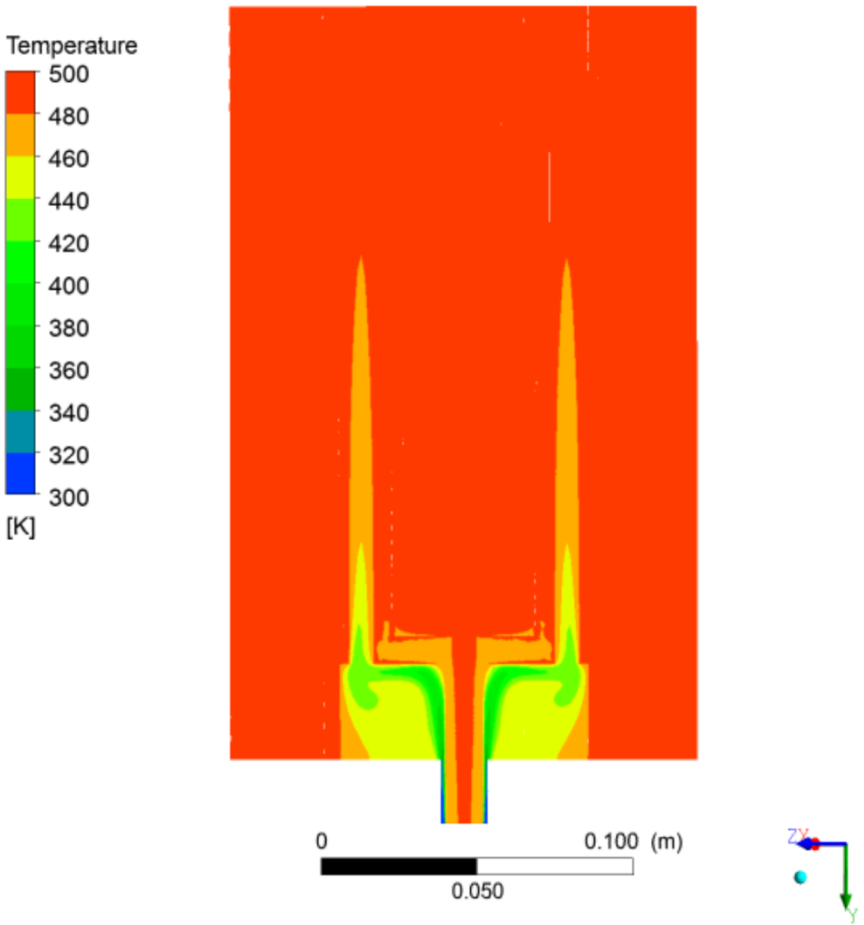

Figure 20: Temperature distribution within the same cross-section of the cell as displayed in Figure 19, 3 bar, 5 SLM fresh gas flow rate, 500 K cell temperature (taken from [158]).

Absorption studies and repeatability

One important quantity of tracer species is the absorption in general and the wavelength-dependent absorption cross-section as a function of temperature in particular.

The absorption cross-section can in principle be measured by determining the laser energy before and after the cell. For this purpose on both sides of the cell photodiodes were positioned detecting reflected light from quartz plates inserted into the beam path. Thus the photodiodes provide relative laser intensity information to calculate the absorption cross section [31, 63, 71] via the geometrical boundaries shown in Figure 17 and the Lambert-Beer law. Previous flow simulations revealed that with an adequate window purge flow tracer diffusion into the window arms of the cell can be neglected [159]. Thus, the assumption of the pathlength being the inner diameter of the measurement cell should be valid. The results shown below, however, indicate that this assumption is not justified and hence absorption cross-sections cannot be derived from measurements performed in this cell.

One example result of such absorption experiments is displayed in Figure 21, where measured absorption and fluorescence of naphthalene is plotted against time after switching on the naphthalene / dodecane flow. As the absorption cross-section cannot be calculated from measurements in this cell, the laser beam attenuation was used to gain information about the time-dependent evolution of the attenuation under otherwise constant conditions. This information is useful to clarify if the duration of an experiment influences the experimental results.

The line in Figure 21 is the laser attenuation calculated from literature values, the geometrical boundaries from Figure 17 and the incident naphthalene concentration using the classical Lambert-Beer law of absorption. Fluorescence (as evaluated from the streak camera LIF spectra, see below) and the laser beam attenuation follow qualitatively the same trend with time. For the first minutes after starting the tracer flow the absorption increases until a plateau is reached after about 20 min. This can be explained by the fact that the tracer needs some time to reach the measurement volume. However, this time seems to be quite long when regarding mean flow velocities (see section above).

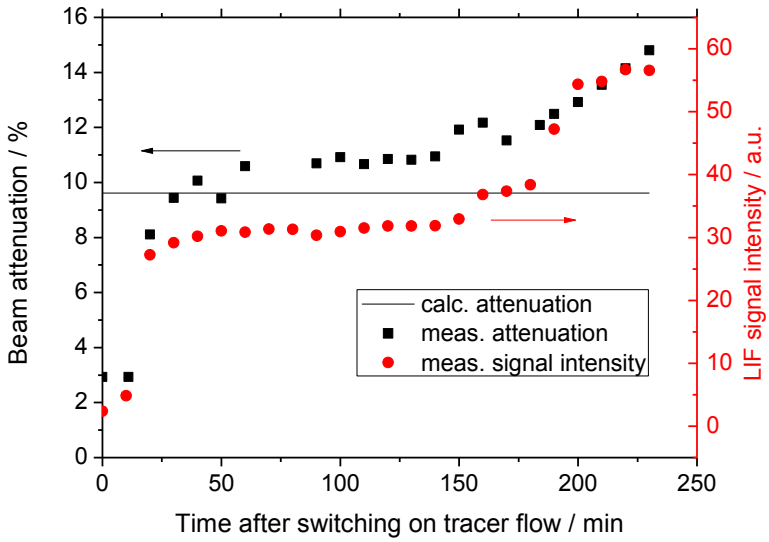

Figure 21: Measured laser beam attenuation (black squares) and fluorescence (red circles) of naphthalene vapour at 373 K, 1 bar, N_2 as a function of time after switching on the naphthalene/dodecane flow. For comparison the calculated absorption is also shown (line).

The following plateau region of constant absorption and fluorescence lasts around 130 min. All measurements presented in this thesis were performed in this plateau region. Subsequently – and this is reproducible – absorption and fluorescence start to increase although nothing has changed in the entire setup. One possible reason might be that due to the open cell small amounts of naphthalene diffuse inside the pressure vessel – in contrast to simulations – and hence cause higher absorption. The increase in fluorescence cannot be explained by this assumption because fluorescence is only detected

from the measurement volume. Another explanation could be that naphthalene accumulates before the lower endplate of the cell before leaving to the exhaust. After a certain time this accumulation is expanded inside the measurement volume where absorption and fluorescence are disturbed. The fluorescence lifetime, however, is not influenced and is constant within the usual experimental error.

Beyond this quantified anomalies other phenomena can be observed which all influence absorption and fluorescence intensity, but not the fluorescence lifetime. For example, the increase of the window purge flow reduces the absorption in a non-linear manner, but increases the fluorescence signal. In contrast to the abovementioned flow simulations [159] some small amounts of tracer may diffuse inside the window "arms" of the cell and cause additional absorption – again confirming the breakdown of the assumption that the window purge flow avoids tracer diffusion out of the measurement cell. Thermodiffusion due to large temperature differences between measurement cell and windows may enhance this. This assumption is strengthened by the fact that at condition where pyrolysis occurs soot deposits can be observed on the windows.

Another unexplainable finding is the fact that doubling the tracer concentration does not double the signal intensity. Re-absorption (signal trapping) of fluorescence light by tracer molecules between the measurement volume and the window may be one reason. The spectral overlap between absorption and fluorescence spectra, however, is low. Self-quenching of tracer molecules may be another reason. This would, however, influence the fluorescence lifetime which was not observable within experimental error. Therefore, convincing explanations describing all phenomena inside the cell are not available yet.

The above investigations suggest that measurements of absolute or relative signal intensities are not feasible with the present version of this cell. Fluorescence lifetimes, however, are not affected. As the fluorescence lifetime is independent on tracer concentration it can be evaluated with sufficient accuracy. In combination with the spectral shape necessary calibration parameters for organic fuel tracers can be derived to develop diagnostic strategies for single- or two-colour detection.

4.2 Optics setup

The experimental arrangement for the combined measurement of effective fluorescence lifetimes and spectra of organic species at high temperature and pressure is depicted in Figure 22. A flashlamp-pumped frequency-quadrupled Nd:YAG laser (PL2143B, Ekspla) delivers a maximum pulse energy of 7 mJ at 266 nm with a pulse length of 26 ps at a repetition rate of 10 Hz. The circular laser beam (Gaussian beam profile) is reduced by a Galilei telescope (f = 100 mm and f = –40 mm) to a diameter of about 3 mm before entering the cell. Fluorescence signals are collected perpendicular to the laser beam axis through one of the larger diameter optical ports (cf., Figure 17, right panel) by a quartz lens (f = 375 mm) and then focused with a second quartz lens (f = 300 mm) and an UV-

enhanced aluminium mirror on the entrance slit of the spectrograph (f = 300 mm, Acton SP2300, Princeton Instruments) equipped with a 150 grooves/mm grating. The spectrally resolved signal is then imaged on the entrance slit of a streak camera (C5680-24C, Hamamatsu Photonics) equipped with a streak module (M5677-01) and a CCD camera (Orca R2, 640×512 pixel). Depending on the manually adjusted height of the entrance slit in front of the photocathode of the streak tube and the chosen sweep speed (perpendicular to the wavelength dispersion axis) a maximum time resolution of about 20 ps can be achieved. For each laser pulse, the system therefore delivers two-dimensional images with temporal and spectral intensity information along each dimension. The streak unit is synchronised with the laser firing using a pulse delay generator (DG645, Stanford Research Systems) triggered externally with the SYNC1 and SYNC2 trigger outputs, respectively, from the laser – depending on the chosen sweep speed of the streak tube and the hence necessary delay between trigger output und laser beam. Camera and spectrograph are controlled via the streak camera software HPD-TA 8.4.0 (Hamamatsu) installed on a personal computer. A second personal computer allows the recording of temperature, pressure, and laser pulse energy before and after the cell using a data acquisition module (USB-6009, National Instruments) and home-made LabView software (version 8.6.1, National Instruments).

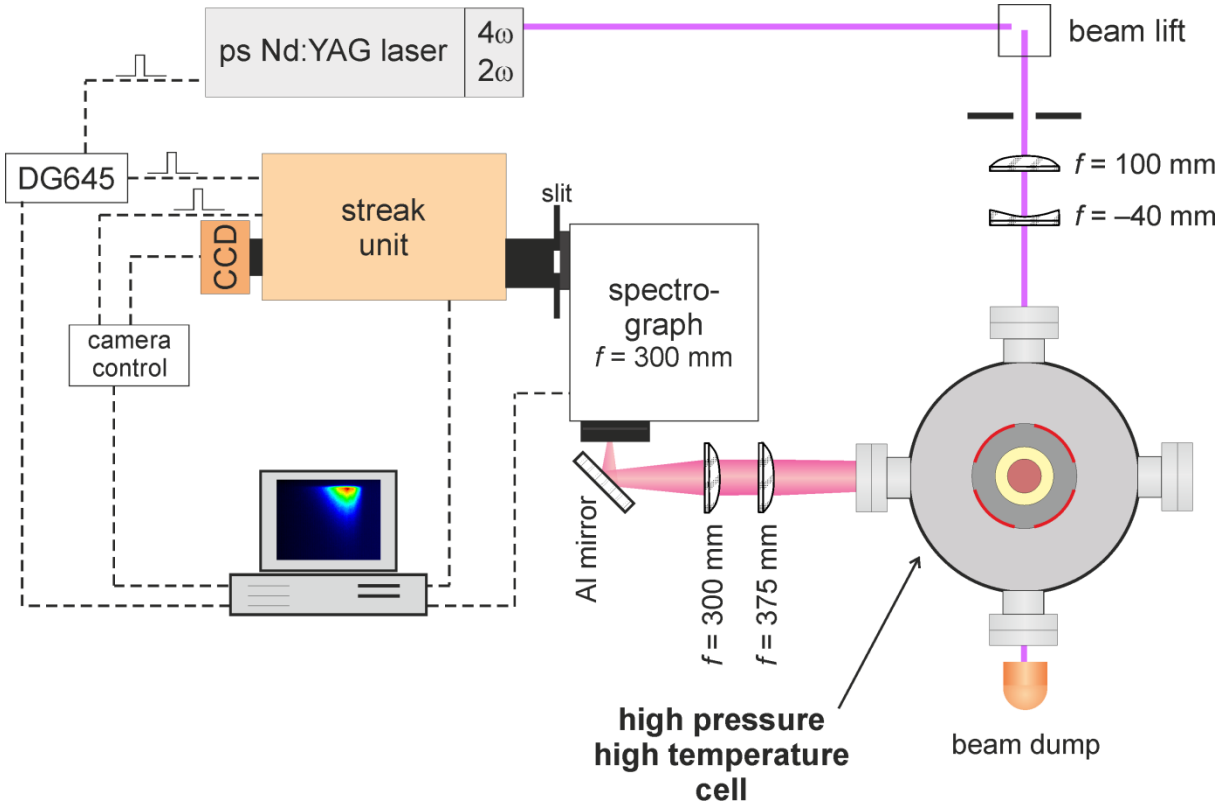

Figure 22: Experimental arrangement for spectrally and time-resolved fluorescence measurements, CCD: CCD camera, DG645: pulse delay generator

4.2.1 Excitation source: ps laser

Figure 23 shows the optical arrangement of the commercial ps-Nd:YAG laser. The laser consists of four different parts: Master oscillator, regenerative amplifier, power amplifier and harmonics generator. The following description is extracted from [160]:

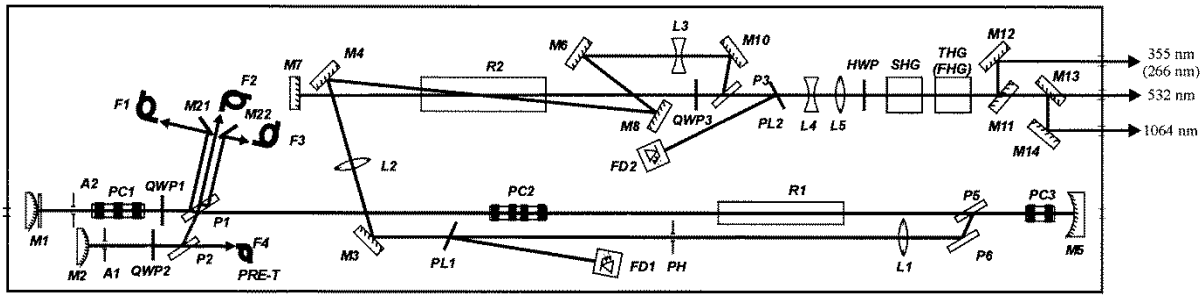

Figure 23: Schematic view and beam paths realised in the ps-Nd:YAG laser used in this thesis, taken from [160]. A: apertures; F: optical fibres; FD: photodetector heads; FHG: fourth harmonics generator; HWP: half wave plate; L: lenses; M: mirrors; P: polarisers; PC: pockels cells; PH: pinhole; PL: glass plates; QWP: quarter wave plates; R: Nd:YAG rods; SHG: second harmonics generator; THG: third harmonics generator

The master oscillator consists of mirror M1, three Pockels cells PC1-3, the oscillator Nd:YAG rod R1, and mirror M5. It utilises active and passive mode locking via Pockels cell PC1 and a solid state modulator (directly in front of M1), respectively. Several roundtrips in the oscillator are necessary to achieve a stable bandwidth-limited pulse. The energy is kept at around 10 μJ in order to not deplete the stored excited state population in R1 by dynamic and fixed losses. Dynamic losses are realised by the radio-frequency modulated Pockels cell PC1 causing variable attenuation. The quarter wave plate QWP1 in connection with polariser P1 cause fixed losses at each roundtrip.

When the bandwidth-limited pulse duration in the oscillator is reached the pulse is directed into the regenerative amplifier to reach pulse energies of around 600 μJ without damaging the mode-locking elements. Hence, the pulse is directed via Pockels cell PC2 and polariser P1 into the regenerative amplifier formed by mirrors M2 and M5.

After a user-defined number of oscillations Pockels cell PC3 rotates the polarisation. Thus, the pulse is dumped via polariser P5 and P6 through the pinhole PH and the mirrors M3 and M4 into the power amplifier. The power amplifier consist of the double flashlamp-pumped Nd:YAG rod R2 and mirror M7 in combination with quarter wave plate QWP3 and polariser P3. In this master amplifier the laser energy is amplified by a variable and user-defined gain up to the maximum amplification factor by varying the delays between the flashlamps and the Pockels cell without influencing the beam profile.

In the harmonics generator section the fundamental wavelength (1064 nm) is frequency-doubled by the second harmonics generator (SHG, K*DP nonlinear crystal) to 532 nm. Subsequently a third harmonics generator (THG, K*DP) or a fourth harmonics generator (FHG, KDP) can be installed to provide 355 and 266 nm radiation, respectively. The dif-

ferent wavelengths are separated by a set of dichroic mirrors. These mirrors are configured in a way that all created wavelengths are simultaneously available through different openings of the laser frame.

All experiments presented here were performed with 266 nm excitation.

4.2.2 Detection system: Streak camera

The operating principle of a streak camera is depicted in Figure 24. The entrance slit in front of the photocathode cuts out a thin ribbon of the incident fluorescence light. Since the spectrograph is mounted in front of the camera, the wavelength coordinate is along the slit axis. This spectrum is then imaged onto the photocathode by the collection optics and is converted into photoelectrons. The electrons pass the space between two sweep electrodes and are accelerated in the streak tube perpendicular to their propagation direction and wavelength axis. The field is swept in a way that a time-dependent streak of the incident photoelectrons is formed on the multi-channel plate (MCP) at the end of the streak tube, beginning at the top down to the bottom. The sweep speed defines the time span imaged on the MCP. The electrons are multiplied in the MCP by a variable and user-defined gain factor. The multiplied electrons cause green light emission after striking a phosphor screen. This screen is finally imaged onto a CCD camera and the image data are transferred to the computer.

The instrument response of this setup to stray light from the excitation laser is a Gaussian type function spread over a specific number of pixels depending on the width of the imaged line. The number of occupied pixels corresponds to a time span depending on the selected sweep speed in the streak tube. The height of the entrance slit defines the thickness of the imaged line which limits the temporal resolution. Thus, an instrument response function has to be recorded for each selected time range and slit width. In this work the slit width was held constant at 50 μm.

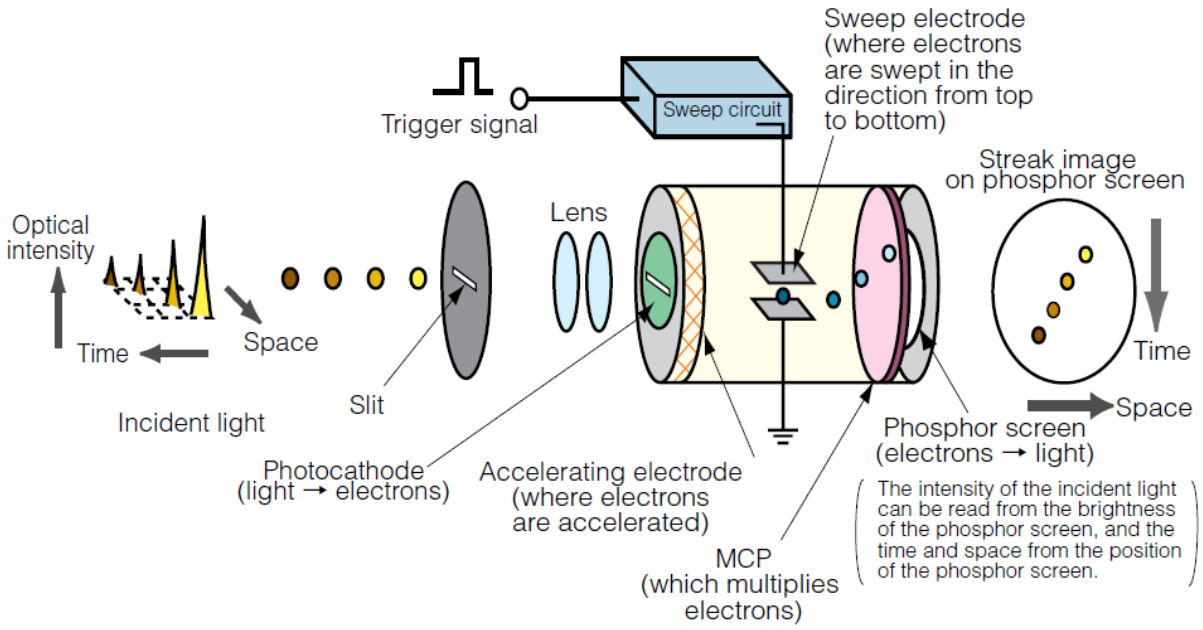

Figure 24: Working principle of a streak camera (taken from [161]). In the realised setup the space axis is converted into wavelength axis because a spectrograph is mounted in front of the camera entrance.

4.3 Data evaluation

In the setup used in this work fluorescence emission from a single point is spread out in the wavelength domain with the spectrograph and in the time domain with the streak camera. Depending on the signal-to-noise ratio, for each condition 200 to 1000 individual measurements were carried out. Single-shot images were then averaged with a jitter-correction routine provided by the streak camera software to minimise smearing of the temporal profiles by overlapping the rising edge of the fluorescence signal of each single-shot image. Finally, a background image was subtracted, which was obtained while the laser was firing and pure nitrogen was flowing through the cell. Resulting sample images are depicted in Figure 25, with wavelength along the horizontal and time along the vertical axis, respectively.

The resulting image delivers either spectrally selected temporal profiles (horizontal binning of columns) or fluorescence spectra for specific time intervals (vertical binning of rows) after laser excitation. It was carefully checked that within experimental uncertainty the number of binned columns does not influence the evaluated decay time. The spectrally-resolved fluorescence emission was extracted by binning a number of rows in the range of significant pixel counts (red rectangle in Figure 25). The resulting spectral profiles were then corrected for instrument spectral response by recording the emission of a lamp with known spectral radiance intensity using the same optical setup. Depending on the wavelength region, a deuterium (for $\lambda < 400$ nm) or a tungsten lamp (for

$\lambda > 350$ nm) was chosen. As this correction function depends on the grating, the centre wavelength and the spectrograph entrance slit width, for each of the chosen parameter sets a lamp spectrum was recorded separately.

The detection system covers a spectral range of about 110 nm which is sufficient for the investigation of most tracer species. In some cases, however, especially when tracer pyrolysis takes place (cf., section 5.2), fluorescence emission is spread over a wider spectral range than covered by one camera image. In these cases, two or more averaged images were recorded for different grating positions to cover the whole spectrum. These spectra must be combined after individual correction for the spectral response. The combining algorithm presented by Rossow [31] was used. In this algorithm the overlapping spectral region of two spectra is filled with a weighted average of both spectra meaning that pixels closer to the CCD centre receive heavier weight factors. This algorithm allows combining of multiple spectra and yields a continuous line without abrupt changes in intensity.

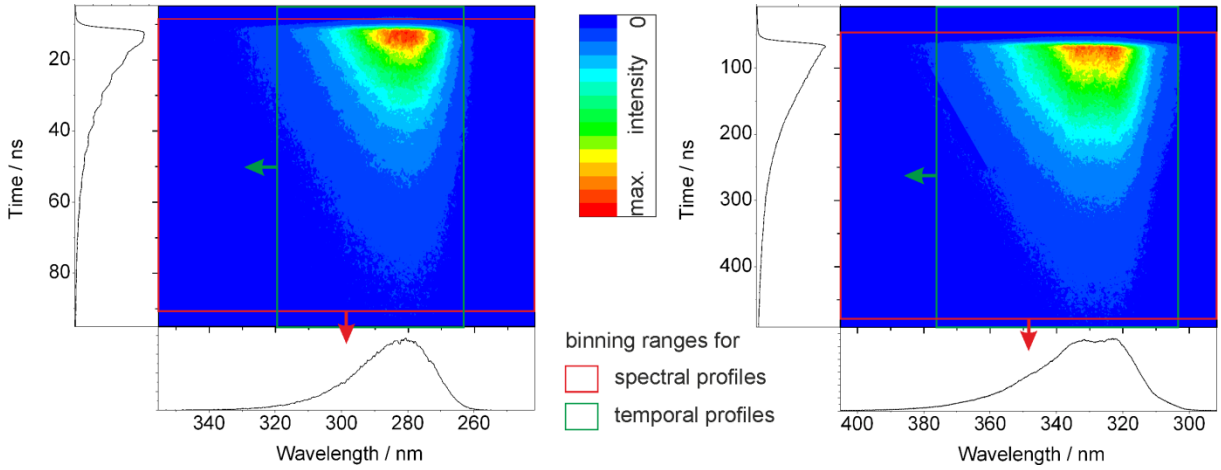

Figure 25: Sample images (averaged over 300 single-shot images) of time- and spectrally-resolved toluene (left panel) and naphthalene (right panel) LIF after excitation at 266 nm. Conditions: 373 K, 2 bar total pressure of CO_2, toluene partial pressure 4 mbar, naphthalene partial pressure 0.4 mbar. The signal integration ranges along the time axis for the evaluated spectral profiles are marked as red, and along the spectral axis for the decay profiles as green rectangles, respectively.

Signal decay times, τ, were determined using a simplified version of the convolve-and-compare technique outlined by Settersten *et al.* [162-163] (cf., eq. 29).

$$I(t) = I_f\left(i_o, \tau_o, t_o; t\right) * f(t) + y_o \quad , \tag{29}$$

where "*" designates a temporal convolution, the index "o" marks an adjustable parameter. I_f is a single-exponential function with the amplitude i_o, the decay time τ_o, and the time offset t_o. When using a double-exponential function I_f, two amplitudes $i_{1,o}$ and $i_{2,o}$ in combination with two decay times $\tau_{1,o}$ and $\tau_{2,o}$ were used. $f(t)$ represents the temporal instrument response function and y_o a baseline offset. Variable parameters in the fit were the decay time(s) and a shift on the time axis to optimise the instance where ex-

perimental and simulated signal intensities reach their peak values. The modelled decay profile is fitted to the experimental one by minimising the sum of squares of the residual differences between the model and the data. The maximum of the decay curve was used to determine t_o.

Using this procedure, Figure 26 depicts representative toluene and naphthalene LIF excitation/decay profiles for three gas temperatures, together with the instrument response function recorded in the spectral region of the laser stray light around 266 nm in the absence of tracer. Since decay times vary substantially with changing environmental conditions, for each temperature the temporal resolution of the streak tube needs to be adjusted for optimised temporal resolution of the detection system along the time axis of the CCD pixel array (here: the y-axis with 512 pixels). Therefore, for each temperature the recorded data trace covers different time spans, and separate instrument functions need to be recorded. For the present hardware settings the minimum temporal resolution of the detection system was 50 ps.

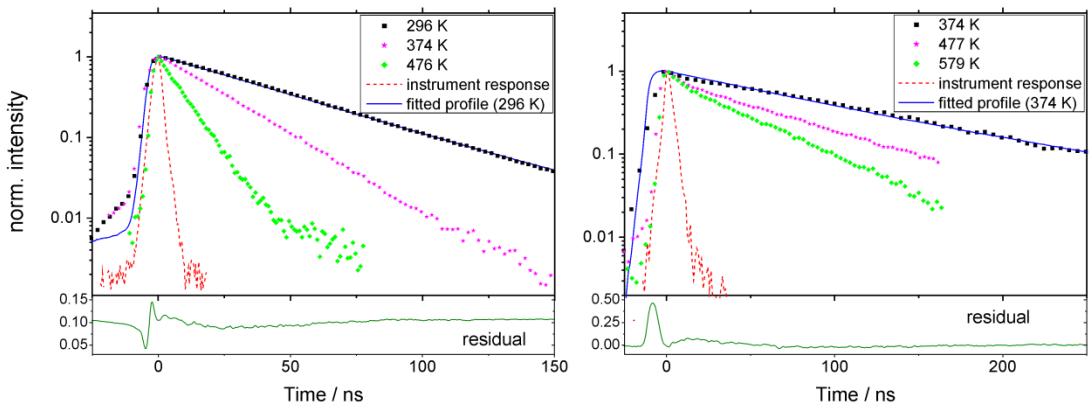

Figure 26: Time-resolved LIF intensity for toluene (left panel) and naphthalene (right panel) in 1 bar N_2 with excitation at 266 nm at various temperatures. For 296 K (toluene) and 374 K (naphthalene), the fitted function and the residuals are shown as blue and green curve, respectively. The instrument response curves (red dashed lines) were recorded without tracer for the streak speeds appropriate for the respective 296 K and 374 K measurements.

5. Results

5.1 Spectroscopic characterisation of tracer species

5.1.1 Toluene

Toluene fluorescence lifetimes were investigated as a function of laser fluence to determine the limits of the linear regime (cf., Figure 27, left panel) which was found to be 35 mJ/cm² at 296 K. This laser fluence was used for temperatures up to 900 K. Because the saturation limit is known to shift to higher fluences at elevated temperatures [17], for sake of an improved signal-to-noise ratio at higher temperatures the fluence level was increased stepwise to 70 mJ/cm² at the highest temperature investigated which was checked to be in the linear regime. The toluene partial pressure was 4 mbar at 296 K which corresponds to a number density of ~2×10^{23} m^{-3}. At higher temperatures the partial pressure was increased to maintain a nearly constant number density of tracer molecules in the probe volume. In additional measurements it was tested that at this number density self-quenching can be neglected (cf., Figure 27, right panel).

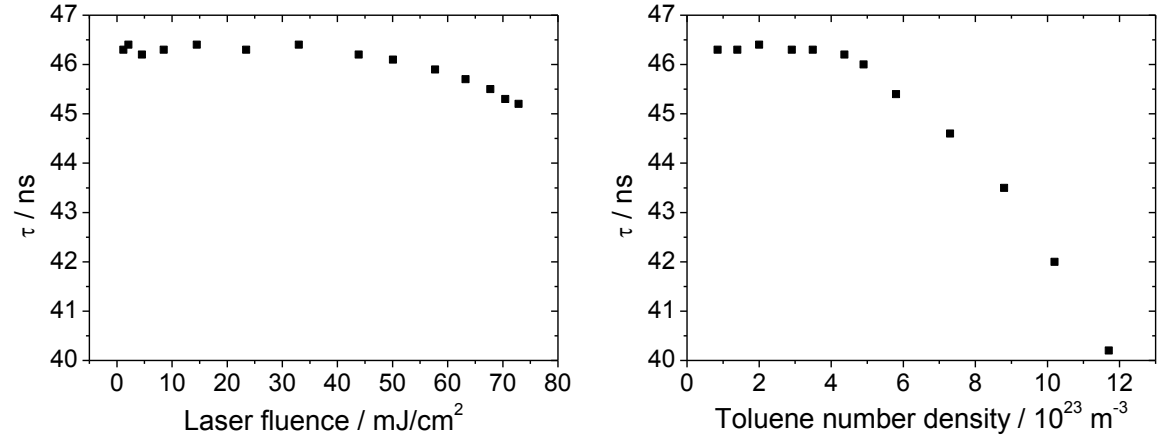

Figure 27: Toluene fluorescence lifetime vs. laser fluence (left panel) and toluene number density (right panel), respectively. The limit of the linear regime can be detected at a laser fluence of 35 mJ/cm², toluene self-quenching can be neglected for number densities below 4×10^{23} m^{-3}.

Temperature and pressure dependence in the absence of oxygen

Figure 28 shows the temperature dependence of toluene fluorescence spectra in 1 bar N_2 normalised to their respective peak intensities. Spectra recorded in CO_2 (not shown here) exhibit similar shapes and positions. The spectra were smoothed by an adjacent-average filter with a window size of 3 nm. At room temperature emission extends from roughly 265 to 340 nm with a maximum at around 280 nm. With increasing temperature, a slight red-shift of this maximum of about 2 nm per 100 K can be observed, and the tail

on the long wavelength side of the spectra becomes stronger relative to the peak which is known from literature (cf., Figure 3) [31, 47]. Due to the limited spectral resolution of the spectrometer / camera unit of about 3 nm (FWHM of a negligible narrow mercury line at 254 nm, indicated by the arrows in Figure 28) an additional "fine structure" except for the two peaks shown in the 296 K spectrum in Figure 28 is not observed in the present data at lower temperatures. Increasing total pressure does not influence the emission spectrum. The results are consistent with previously published work by Koban [47] and Rossow [31].

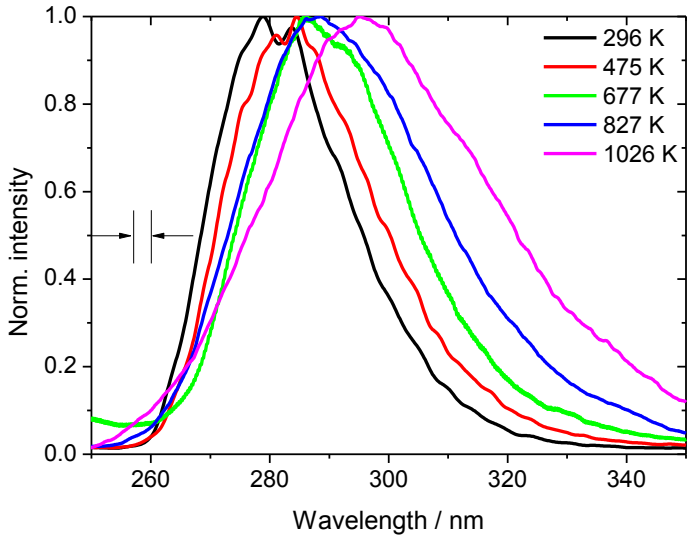

Figure 28: Peak-normalised toluene fluorescence spectra at various temperatures in 1 bar N_2 bath at a toluene number density of ~2×10^{23} m^{-3}. Spectra in CO_2 are similar. The arrows indicate the spectral resolution of the detection system by the FWHM of a recorded mercury line at 254 nm from a low-pressure discharge lamp.

Figure 29 shows temperature-dependent toluene fluorescence lifetimes measured in bath gases of pure N_2 and pure CO_2 at 1 bar total pressure. The effective fluorescence lifetime strongly decreases with increasing temperature (from 46±3 ns at room temperature until close to the temporal resolution limit of 0.05±0.01 ns at 925 K). Within the investigated temperature range and quoted error limits, the evaluated fluorescence lifetimes are identical for both N_2 and CO_2 as collider species. From room temperature up to 950 K a strong reduction in fluorescence lifetimes, and thus the fluorescence quantum yield is observed. This reduction follows the prediction of the Koban model (solid line in Figure 29) obtained from time-integrated LIF intensities.

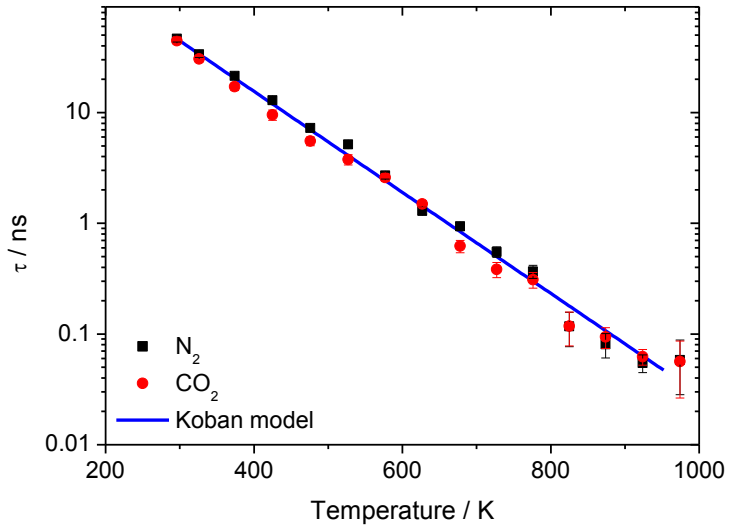

Figure 29: Effective fluorescence lifetimes of toluene as a function of temperature in 1 bar N_2 (black squares) and CO_2 (red circles), respectively. Solid line: Relative fluorescence quantum yield calculated from the phenomenological model of Koban *et al.* [29].

The almost constant lifetimes seen for temperatures larger than 900 K may be explained with the limited temporal resolution of the detection system and the convolute-and-compare algorithm. Note, that at such high temperatures there is some concern about the onset of thermal decomposition of toluene within the residence time in the cell. Chapter 5.2 will deal with this topic in more detail.

In the past the influence of total pressure on the toluene fluorescence quantum yield has been neglected [8, 47, 49] leading to inaccurate analysis of, e.g., in-cylinder measurements [21]. Only recently a quenching effect with pressure in N_2 was reported by Rossow [31] for time-integrated signal intensities determined at 450 and 700 K, validating the presented lifetime measurements of toluene at elevated pressures (cf., Figure 30). When normalising Rossow's data with the respective lifetimes at 1 bar from measurements of this work at the nearest measured temperatures, they show good agreement (cf., Figure 30). Compared with N_2, in CO_2 (not shown), the quenching effect is slightly more pronounced (by about 5%). A comparison with the model of Koban *et al.* is not possible because this model does not include the effect of total pressure. Therefore, in the present work Koban's model was extended to also cover the behaviour at higher pressures in N_2 (see later). The results of this modified model are included in Figure 30.

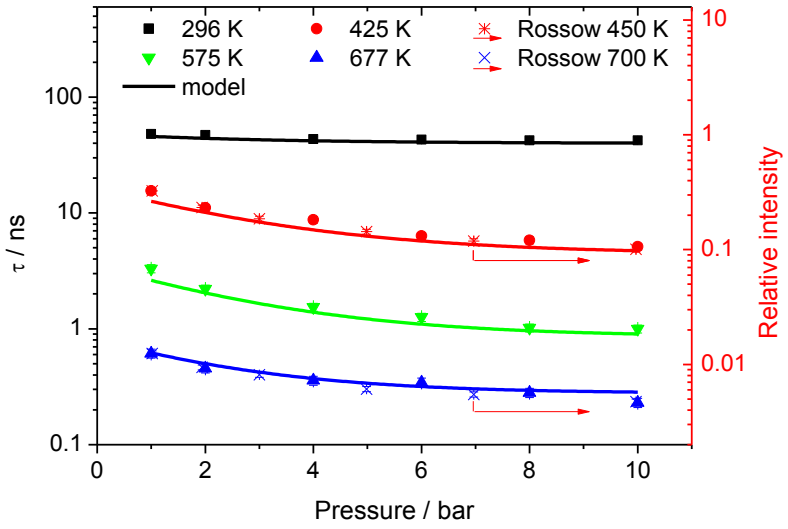

Figure 30: Effective fluorescence lifetimes of toluene in N_2 (symbols) as a function of total pressure at various temperatures. For comparison, normalised signal intensity values from Rossow [31] are included (cross symbols). Lines are from the modified Koban quantum yield model. See text for details.

The decrease in the effective fluorescence lifetimes of toluene (cf., Figure 30) with increasing pressure is in contrast to pressure effects known from, e.g., ketones (e.g., [85, 88]) and naphthalene (e.g., [71]). This finding is traced back in literature to the fact that upon 266 nm excitation, toluene is excited in the vicinity (~580 cm^{-1} at 300 K) of the 0–0 electronic transition. Such close to the S_1 origin the stabilisation effect of collisions with the bath gas is inverted into a destabilisation effect. This was interpreted as a so-called photo-induced cooling effect of the excited-state vibrational distribution initially prepared by the excitation process. Subsequently, collisional heating by the bath gas follows [65, 164], which transforms population into higher lying vibrational levels undergoing faster non-radiative deactivation. This pressure destabilisation effect is also found for other aromatic species when excited near the vibrationless S_1–S_0 transition by photon absorption, e.g., anthracene excited at 365 nm [165] (cf., section 3.2).

With respect to excited state energy transfer and relaxation, in previous literature for toluene [58] a so-called "third decay channel" is discussed if a certain amount (~2150 cm^{-1}) of excess energy is reached in the S_1 state. For benzene, this third decay channel opens up because of enhanced internal conversion due to nonadiabatic transitions via conical intersections [68, 166]. It is easy to imagine that for toluene similar processes occur [31, 58]. This additional loss channel also causes the appearance of a second lifetime component in the fluorescence decay curves, e.g., when at room temperature excitation is accomplished with wavelengths shorter than 250 nm. In addition to the typical fluorescence lifetimes measured in the present work, Zimmermann *et al.* found a short lifetime component when excitation of toluene is performed at 248 nm at room temperature [55]. Alternatively, for 266 nm excitation this deactivation channel is

opened for temperatures higher than ~480 K. At temperatures above ~500 K the toluene decay curves can be fitted equally well using double-exponential decays. However, the fast decay component in toluene fluorescence has a low amplitude making meaningful data evaluation difficult.

Influence of molecular oxygen

The shape of the toluene fluorescence spectrum (cf., Figure 28) does not change with increasing amounts of O_2 present. This finding is in accord with Koban *et al.* [29] and Rossow [31] who found that upon 266 nm excitation no spectral shift occurs with either increasing O_2 partial pressure or total pressure for all bath gases investigated.

Molecular oxygen is a strong fluorescence quencher of the S_1 state in toluene [7, 29]. Figure 31 shows the significant influence of O_2 on the effective fluorescence lifetime. At room temperature the fluorescence lifetime is reduced with increased O_2 partial pressure, with this trend decreasing at higher temperatures. The measurements cover a range of temperatures and O_2 partial pressures between pure N_2 and air at 1 bar total pressure. The fluorescence lifetime in air at room temperature of 0.63±0.05 ns is in good agreement with measurements of Ehn *et al.* [60] of 0.65 ns. The decreasing quenching efficiency of O_2 with increasing temperature has also been observed by Koban *et al.* [29] and by Rossow [31] after excitation with 266 nm when determining relative fluorescence quantum yields from time- and wavelength-integrated toluene fluorescence spectra. Again, the measurements are in good agreement with the model of Koban (solid lines in Figure 31) even in the presence of O_2 without any correction.

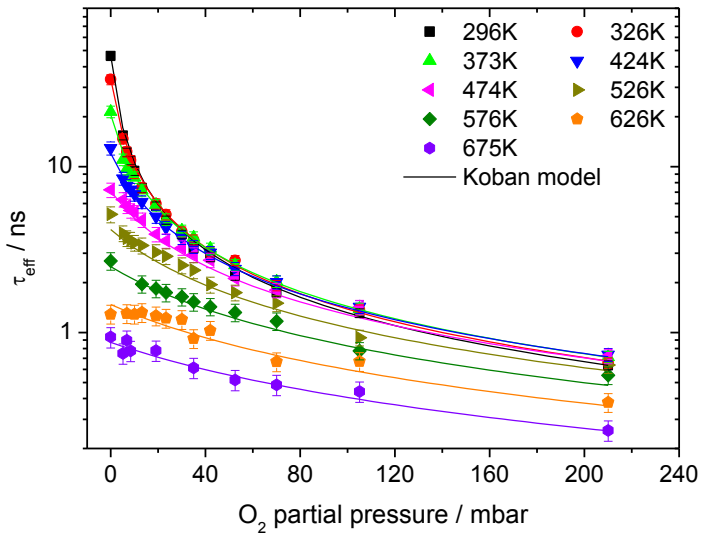

Figure 31: Effective fluorescence lifetimes of toluene diluted in N_2 as a function of O_2 partial pressure at 1 bar total pressure and for various temperatures. Solid lines: Lifetimes calculated from the phenomenological model of Koban *et al.* [29].

Figure 32 shows effective fluorescence lifetimes of toluene in air (symbols) as a function of temperature for pressures from 1 to 10 bar. Due to the high O_2 partial pressures, fluorescence lifetimes are much shorter than in N_2 (cf., Figure 31). For constant temperature the fluorescence lifetime decreases with increasing air pressure, more significantly at lower temperatures. The effect of O_2, however, saturates at a partial pressure of p_{O2} of around 2 bar. For 1 bar total pressure, the increase of the fluorescence lifetime in air with increasing temperature up to 450 K was also observed by Koban *et al.* [29]. The increase is due to the decreasing O_2 number density with increasing temperature and thus a decreased collision rate. At higher temperatures the temperature effect dominates the quenching effect and thus the lifetime decreases. The temperature drop-off is shifted to higher temperatures with increasing pressure due to increased quenching by the higher O_2 concentrations. For comparison, predictions from the Koban model [29] are included in Figure 32 (solid lines) by normalising for each pressure to the respective measured lifetimes at room temperature. The model shows large deviations at total pressures higher than 1 bar, especially at higher temperatures above 500 K. It needs to be emphasised here that the model does not handle effects of total pressure.

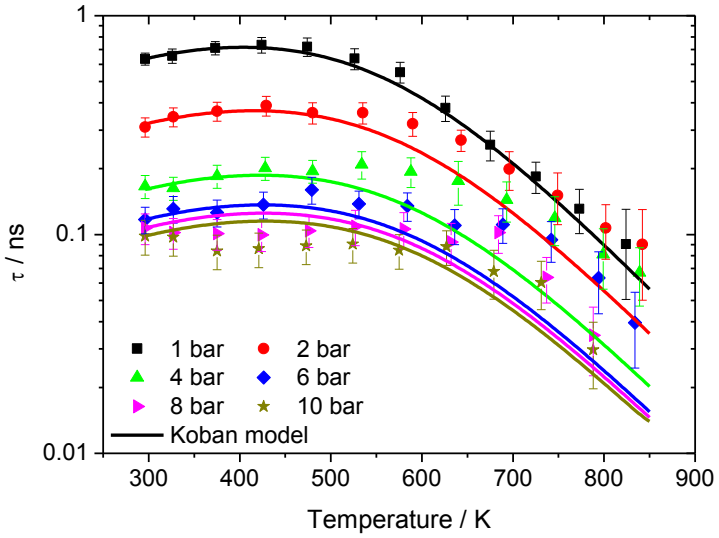

Figure 32: Effective fluorescence lifetimes of toluene as a function of temperature at various air pressures. Solid lines: Relative fluorescence quantum yield calculated from the Koban model [29], normalised to the respective values at room temperature.

As temporally-integrated fluorescence intensities of toluene show Stern-Volmer behaviour [29, 31], according to eq. (20) this should also apply to the measured effective fluorescence lifetimes. To validate this, Stern-Volmer coefficients were determined from data taken at atmospheric pressure for varying O_2 partial pressures and several temperatures (cf., Figure 31 and Figure 33, left panel). The temperature-dependent Stern-Volmer coefficients for quenching of toluene by O_2 are depicted in Figure 33 (right panel, filled squares) together with values from Koban *et al.* [29] and Rossow [31]. There is overall agreement, especially with the values of Koban *et al.*, while up to 550 K the Stern-

Volmer coefficients of Rossow are systematically higher by about 30%. Shifting his data by about 25 K towards lower temperatures brings the values in agreement with our data. As our coefficients and the ones from Koban *et al.* follow the same single-exponential trend (solid curve in Figure 33, right panel) and are close to each other within their combined measurement uncertainty we conclude that it is more likely that the values of Rossow are too high than that both the values of this thesis and Koban's values are too low.

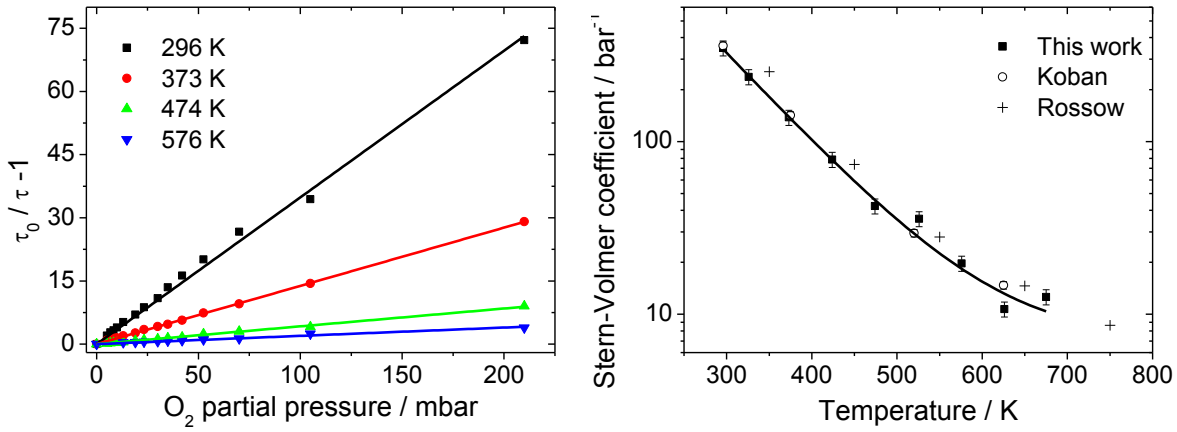

Figure 33: Stern-Volmer plots of toluene fluorescence quenched by O_2 for selected temperatures (left panel). Stern-Volmer coefficients (right panel) for toluene at various temperatures for 1 bar total pressure. Values of this work (filled squares) are compared to values by Koban *et al.* (open circles) [29] and Rossow (plus symbols) [31]. The line is a mono-exponential fit to the data from this work.

Model improvement

One simplification made in Koban's fluorescence model [29] is the neglect of the effect of total pressure on the relative fluorescence quantum yield. The presented measurements have shown that the effective fluorescence lifetime also depends on total pressure (cf., Figure 30). Using these data it is possible to expand the model by introducing an additional multiplicative pressure-dependent factor as shown in Eq. (30).

$$\phi_{rel} \propto \tau_{eff} \propto \left(\frac{A_1(T)}{1+k_{SV,1}(T)\cdot n_{O_2}} + \frac{A_2(T)}{1+k_{SV,2}(T)\cdot n_{O_2}} \right) \cdot \left(B_1(T)\exp\left(-\frac{p_{tot}}{B_2(T)} \right) + B_3(T) \right) \qquad (30)$$

with p_{tot} as the total pressure in bar. To obtain the necessary fitting coefficients B_1, B_2, and B_3 the last term in Eq. 30 was fitted to the pressure-dependent data in Figure 30, normalised to their value at 1 bar for each temperature. The temperature dependence of the coefficients B_1, B_2, and B_3 are then given by the fitting polynomials in Table 5, all other parameters in Eq. 30 do not change and can be found in [29], but for sake of completeness they are added in Table 5.

Table 5: Fitting coefficients to model the effective fluorescence lifetime, i.e., the relative fluorescence quantum yield as a function of temperature, pressure (multiplier in Eq. 30), and O_2 number density of toluene after 266 nm excitation. Temperature T is in K.

Parameter	Expression
$A_1(T)$	$\phi_{fl}^{N_2}(T) - A_2(T)$
$A_2(T)$	$\dfrac{1}{0.0241T^2 - 25.12T + 7029}$
$\phi_{fl}^{N_2}(T)$	$22.5\exp(-0.0105T)$
$k_{SV,1}(T)$	$7.69\cdot10^{-25} + 2.57\cdot10^{-22}\exp(-0.010T)$
$k_{SV,2}(T)$	$8.8\cdot10^{-26} - 4.0\cdot10^{-28}(T-500)$
$B_1(T)$	$-8.713 + 0.0574T - 1.22\cdot10^{-4}T^2 + 1.12\cdot10^{-7}T^3 - 3.80\cdot10^{-11}T^4$
$B_2(T)$	$3.32 - 1.39\cdot10^{-3}T$
$B_3(T)$	$7.76 - 0.0465T + 1.06\cdot10^{-4}T^2 - 1.06\cdot10^{-7}T^3 - 3.97\cdot10^{-11}T^4$

A comparison of calculated fluorescence lifetimes with the experimental data is presented in Figure 30 (solid lines) showing overall good agreement. At atmospheric pressure the model is reduced to Koban's model equation.

Note that these modifications are only valid for the conditions of the present experiments, i.e., 266 nm excitation, temperatures between room temperature and 950 K, and for total pressures ranging from 1 to 10 bar. Additional quenching effects that occur in the presence of O_2 (cf. Figure 32) at pressures above atmospheric are not covered by Eq. 30. Effects including O_2 quenching at elevated pressures would cause much more modelling effort. It will be part of future work to model toluene fluorescence quantum yield with a step-ladder type model to cover all observable aspects with physically based model parameters.

5.1.2 Naphthalene

The naphthalene fluorescence intensity was investigated as a function of laser fluence to determine the limits of the linear regime, which was found to be 35 mJ/cm² at 373 K [137]. At 374 K the naphthalene partial pressure was fixed at 0.4 mbar. At higher temperatures the partial pressure was increased to maintain a nearly constant number density of tracer molecules in the probe volume. In additional measurements it was tested that at this number density self-quenching can be neglected [137].

Temperature and pressure dependence in the absence of oxygen

Figure 34 shows peak-normalised fluorescence spectra of naphthalene diluted in N_2, and for a range of temperatures at a total pressure of 1 bar. As for toluene, within the measurement accuracy, spectra in CO_2 (not shown) exhibit indistinguishable shapes and positions. At 374 K, fluorescence emission extends from roughly 305 to 400 nm with a maximum at around 335 nm. For naphthalene, the red-shift of the emission spectrum with increasing temperature (5 nm per 100 K) is more pronounced than for toluene. Again, the tail on the long wavelength side of the spectrum becomes stronger relative to the peak emission. Regarding peak position and half width these results are consistent with other work [13, 20, 71]. Orain *et al.* [71], however, report a different fine structure of the emission peak, where the first peak is larger than the second, whereas in this thesis, and also reported by Kaiser and Long [20], the second vibrational peak is the strongest. Ossler *et al.* [13] do not report a fine structure.

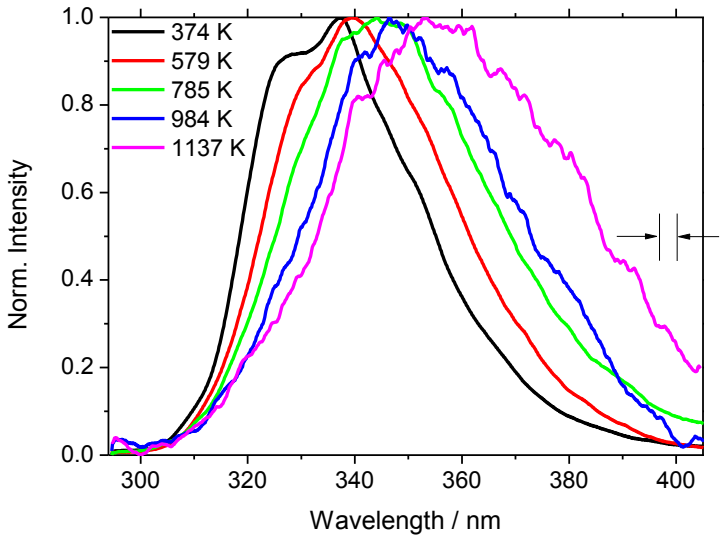

Figure 34: Peak-normalised fluorescence spectra of naphthalene upon 266 nm excitation at various temperatures in 1 bar N_2 at a naphthalene number density of ~2×10^{22} m^{-3}. The spectra in CO_2 are similar. The arrows indicate the spectral resolution of the detection system.

For the fluorescence decay, previous work by Ossler *et al.* [13] has shown that it can be described by two lifetime components, representing two different deactivation channels in the excited molecule. They were identified as intersystem crossing (ISC) and internal conversion (IC) [66]. While for energies relevant in this thesis ISC is always present as a deactivation pathway, the IC channel is activated only when a certain threshold excess energy is available in the S_1 state vibrational manifold. In contrast to toluene, the 266 nm excitation in naphthalene already provides enough excess energy at low temperatures (~2500 cm^{-1} at 374 K) to make that happen [58, 66]. Therefore, double-

exponential functions were applied when fitting all measured naphthalene fluorescence decay profiles of this thesis.

In Figure 35 the evolution of both components of naphthalene fluorescence lifetimes with temperature is shown for N_2 pressures between 1 and 10 bar. At temperatures higher than 1000 K the limited signal-to-noise ratio of the fluorescence decay profiles prevented double-exponential fits from extracting the short lifetime component. The fluorescence lifetime decreases by a factor of 370 when temperature increases from 373 to 1123 K, i.e., from 104±6 ns down to 0.28±0.05 ns. Noteworthy in Figure 35 is the marked increase of the negative slope of the temperature-dependent lifetime decay above about 800 K. Compared with results from toluene (cf., Figure 31), for naphthalene the effect of pressure is not only much reduced, but also lifetimes increase instead of decrease with increasing pressure (cf., inset in upper panel of Figure 35), although this trend is almost buried within the error limits at temperatures higher than 800 K. This behaviour of naphthalene is attributed to faster vibrational relaxation into the lowest vibrational levels of the S_1 state due to an increased number of buffer gas collisions, thus increasing the chance for fluorescence due to a much reduced intersystem crossing rate out of the lowest vibrational levels in S_1 [31, 71]. At temperatures below 800 K data from this thesis at 1 bar agree well with results from Ossler *et al.* [13]. However, at higher temperatures lifetimes from this thesis are significantly shorter than those reported by Ossler *et al.* which might be attributed to their quoted temporal resolution of 2.5 ns. In CO_2, lifetimes at 1 bar (not shown here) are the same as those in N_2 within experimental error. At higher pressures, lifetimes in CO_2 are marginally longer (by about 5%) than in N_2. The results of a phenomenological model for naphthalene (introduced later) are included in Figure 35 for a total pressure of 1 bar.

Although with much larger experimental error, the short lifetime component shows a similar behaviour with temperature. At temperatures up to 600 K the lifetime nearly stays constant at around 7±1 ns, while at higher temperatures it decreases to 0.6±0.2 ns at 923 K. Within the error limits a pressure effect could not be observed. The values at 1 bar total pressure are consistent with those of Ossler *et al.* [13], while at temperatures beyond 800 K our lifetimes are smaller by about a factor of 2.

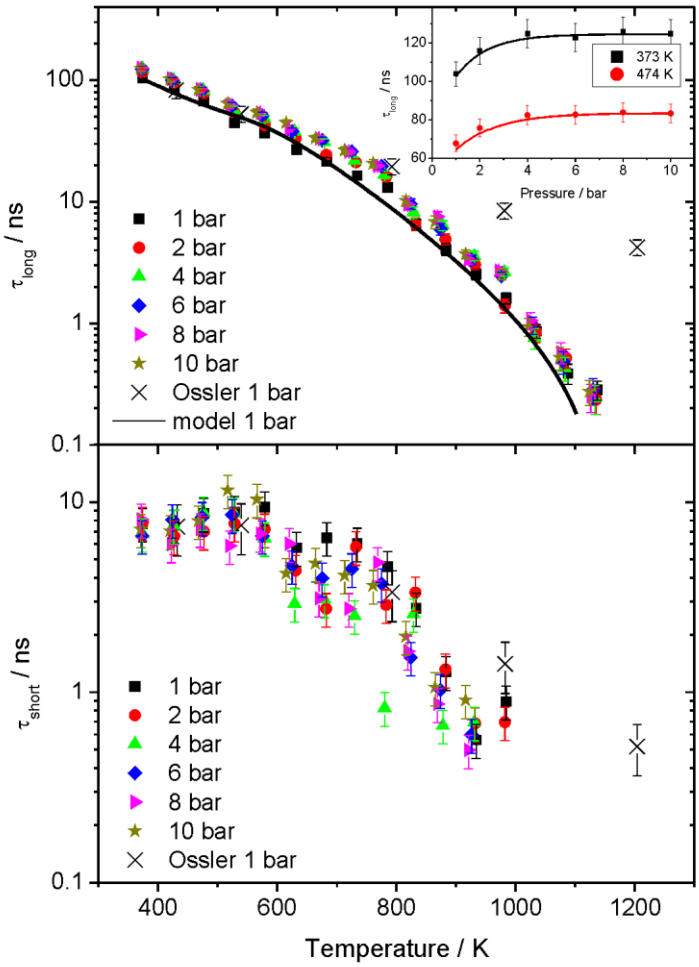

Figure 35: Effective fluorescence lifetimes of naphthalene as a function of temperature for several total pressures in N_2. Upper panel: Long lifetime component, lower panel: Short lifetime component. Comparison is made to literature data from Ossler *et al.* [167] (crosses). Inset in the upper panel: Long lifetime component vs. total pressure of N_2 for two temperatures. The long lifetime component at 1 bar is compared to calculated values from the model presented below.

In contrast to toluene, excitation of naphthalene with 266 nm radiation deposits energy far above (~6000 cm^{-1} at 400 K) its S_1 0–0 band origin. Therefore, collisions cause stabilisation of population in S_1 due to vibrational relaxation, and thus an increase of the fluorescence lifetime with increasing pressure. This stabilisation effect was first described for naphthalene by Beddard *et al.* [168] theoretically and proven experimentally.

For naphthalene, a similar "third-decay-channel" as known from toluene and benzene is reported at a threshold of 10,000 cm^{-1} [169]. When exciting beyond this threshold the non-radiative decay rate increases rapidly. When exciting with 266 nm radiation, this energy corresponds to a temperature of about 750 K. This may explain the change in logarithmic slope in Figure 35 for the long lifetime component and the beginning decrease in the short lifetime component at around 800 K. The explanation is that the non-

radiative processes are enhanced above this limit and thus the lifetime is shortened "faster" than below.

In contrast to toluene, the short lifetime component in naphthalene cannot be explained by this third-decay-channel because it is present already at energies where this deactivation channel is not yet available. One reason found in literature is fluorescence from higher excited states, such as S_2 [13] competing with vibrational relaxation to the S_1 state. Satisfactory explanations, however, have not been published yet.

Influence of molecular oxygen

In contrast to the emission spectrum of toluene (with 266 nm excitation), which is unaffected by O_2, the fluorescence spectrum of naphthalene shows a significant red-shift with increasing O_2 partial pressure (cf., Figure 36). While the shift is pronounced for low O_2 partial pressures it seems to saturate for O_2 pressures larger than 100 mbar. This oxygen-dependent red-shift occurs in addition to the temperature-dependent red-shift and is visible for all temperatures with similar amplitude. These observations are consistent with the work of Orain *et al.* [71] and Kaiser and Long [20].

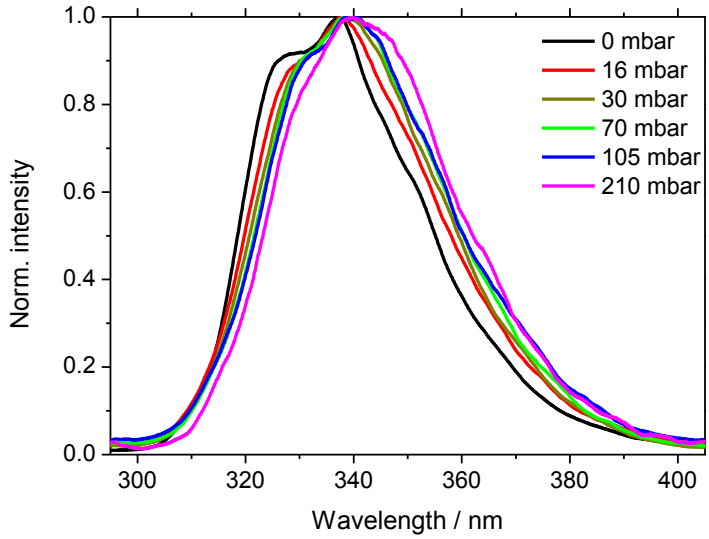

Figure 36: Peak-normalised fluorescence spectra of naphthalene upon 266 nm excitation as a function of O_2 partial pressure at 373 K and 1 bar total pressure.

In air the effect of temperature on the fluorescence lifetime (cf., Figure 37) is quite different from the behaviour in N_2 (cf., Figure 35): For constant temperature, increased air pressure causes a strong decrease of fluorescence lifetime due to increased O_2 number density. The quenching effect for naphthalene is stronger than for toluene (cf., Figure 32): For naphthalene the average decrease ranges from about 1.1 ns at 1 bar to about 0.05 ns at 10 bar, while for toluene these values change from 0.7 ns to 0.09 ns in the same pressure interval. For each air pressure the fluorescence lifetime is almost tem-

perature independent in the range from 373 to 700 K, followed by a stronger decrease, until naphthalene undergoes oxidation reactions at around 875 K. This behaviour is similar to that reported by Orain *et al.*, who also found such a plateau region for the time-integrated spectral intensities at 1 bar total pressure [71]. For air pressures above 2 bar the range where the lifetime is constant (within experimental error) is extended to even higher temperatures. For the present conditions the amplitude of the short lifetime component is too small to be determined with sufficient accuracy.

The measurements show that for naphthalene, quenching by O_2 almost dominates over the temperature effect – in contrast to toluene, where a pronounced temperature effect is still present in air up to a pressure of about 8 bar (cf. Figure 32). Therefore, these results support the conclusion of Kaiser *et al.* [20] that naphthalene should be a suitable tracer for fuel/air-ratio measurements. Figure 37 also displays calculated lifetimes for various total air pressures, normalised to the respective value at 373 K, using a phenomenological fitting function described below.

The lifetimes at the highest temperature of 875 K decrease more strongly than suggested by the trend seen at lower temperatures. This discrepancy is attributed to the onset of naphthalene oxidation in the gas flow which makes it uncertain as to whether signals originate from naphthalene and/or from pyrolysis and oxidation products, probably having shorter lifetimes than the parent molecule.

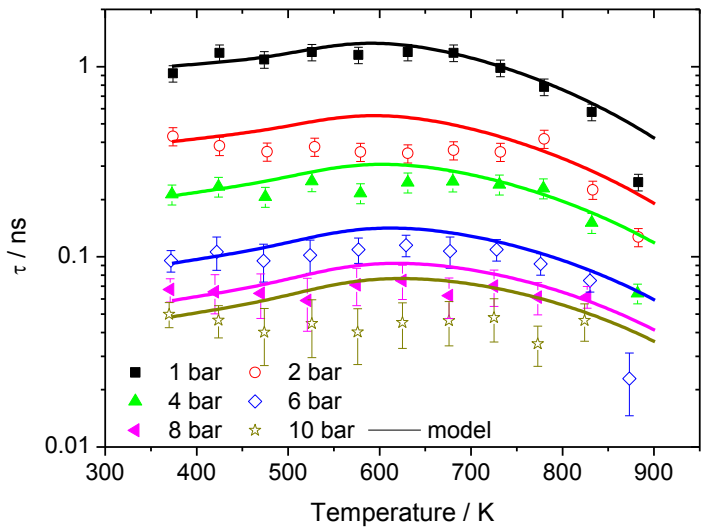

Figure 37: Effective fluorescence lifetimes of naphthalene as a function of temperature for several air pressures. Lines are lifetimes calculated from a fitting function introduced below, normalised to the respective value at 373 K.

Collisional quenching of naphthalene by O_2 was also investigated at various temperatures by varying the O_2 partial pressure at a total pressure of 1 bar. From previous work it is known that collisional quenching of naphthalene by O_2 follows Stern-Volmer behaviour [20, 71], cf. eq. (20) and Figure 38 (left panel). As shown in Figure 38 (right panel)

the resulting coefficients (filled red triangles and fitted exponential) are systematically lower and show a somewhat larger slope than the results by Orain *et al.* [71] within the overlapping temperature range. The result from Kaiser and Long at 500 K (red open diamond) is lower by 40% relative to the value of the fit function [20]. The Stern-Volmer coefficients for naphthalene are larger than those of toluene, indicating higher fluorescence quenching efficiency in collisions with O_2. This also supports the result presented above that in air naphthalene fluorescence lifetimes are nearly unaffected by temperature.

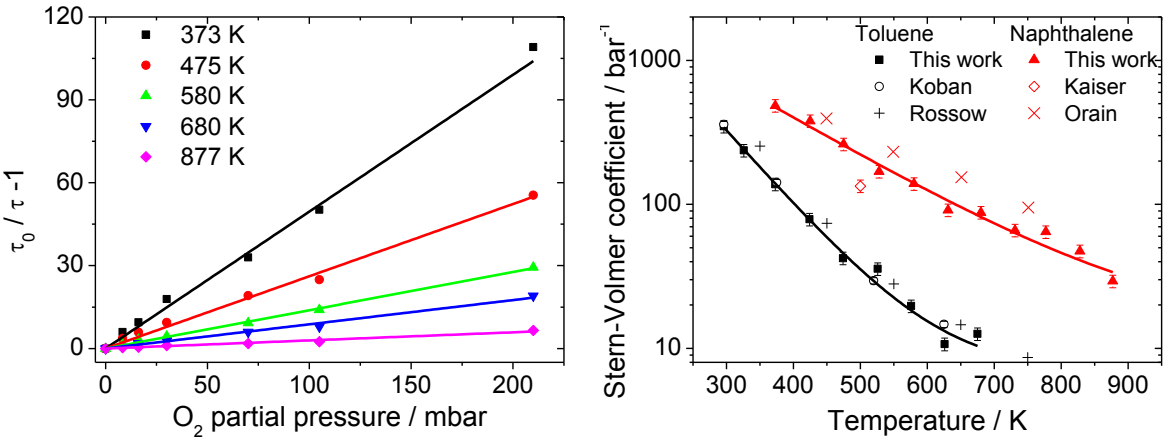

Figure 38: Stern-Volmer plots of naphthalene fluorescence quenched by O_2 for selected temperatures (left panel). Stern-Volmer coefficients (right panel) for toluene and naphthalene at various temperatures for 1 bar total pressure. Values of this work (filled black squares and red triangles) compared to values for toluene (cf., Figure 33) by Koban *et al.* (open black circles) [29] and Rossow (black plus symbols) [31], and for naphthalene by Orain *et al.* (red crosses) [71] and Kaiser and Long (open red diamond) [20]. Lines are mono-exponential fits to the data.

Phenomenological model for naphthalene

The model presented below for naphthalene is a functional fit to experimental data. The short lifetime component is low in amplitude and not evaluable in air. Therefore, for simplification the presented model functions are applied only for the long lifetime components. When comparing to (relative) quantum yield data, additional deviations may occur due to this simplification.

The model equation (eq. 31) consists of three terms (enclosed in square brackets): The first term describes the temperature dependence of the relative naphthalene fluorescence quantum yield ϕ_{rel} at 1 bar in pure N_2. The second term represents the pressure dependence in N_2 bath in the absence of O_2 which equals unity at 1 bar total pressure. The third term describes O_2 quenching by a Stern-Volmer relationship, where the temperature dependence is derived from the exponential fit in Figure 38.

$$\phi_{rel} = \left[A_1 + \left(\frac{A_2}{A_3 \cdot \sqrt{0{,}5 \cdot \pi}} \right) \cdot \exp\left(-2 \left(\frac{T - A_4}{A_3} \right)^2 \right) \right] \cdot \left[B_1(T) \cdot \exp\left(-\frac{p_{tot}}{B_2(T)} \right) + B_3(T) \right] \cdot \left[\frac{1}{1 + k_{SV}(T) \cdot p_{O_2}} \right] \tag{31}$$

Table 6 lists the respective model parameters. Fluorescence lifetimes can be calculated by multiplying ϕ_{rel} with a constant factor of 104 ns, as shown in the last row of Table 6.

Table 6: Fitting coefficients and polynomials used in the functional form of Eq. 31 for modelling the effective fluorescence lifetime of naphthalene upon 266 nm excitation as a function of temperature, O_2 partial pressure and total pressure in N_2. Temperature T is in K, total pressure p and O_2 partial pressure p_{O2} in bar.

Parameter	Value
A_1	$-6.381 \cdot 10^{-3}$
A_2	6376
A_3	850.6
A_4	-424
$B_1(T)$	$-0.00704 - 0.00117 \cdot T$
$B_2(T)$	$1.059 + \frac{5.943}{1 + 10^{(7323 - T) \cdot 0.00376}}$
$B_3(T)$	$1.156 + \frac{0.5056}{1 + 10^{(531.8 - T) \cdot 0.01019}}$
$k_{SV}(T)$	$4644 \exp\left(-\frac{T}{161} \right) + 13.77$
τ_{eff}	$104 ns \cdot \phi_{rel}$

This model function is valid from 373 up to 1100 K without O_2, and up to 900 K in the presence of O_2. Model results are compared with the temperature dependence of the data in N_2 at 1 bar in Figure 35, and with the temperature dependence in air at various total pressures in Figure 37, respectively. At air pressures above 1 bar the agreement between experimental data and model predictions is reduced, especially since the modelled lifetimes evolve through a shallow maximum with increasing temperature, which is not seen in the data. As these functions are derived from data at 1 bar total pressure, differences at elevated pressures might occur due to photo-physical effects not covered by this simple approach.

5.1.3 Anisole

In this section the properties of fluorescence spectra and effective fluorescence lifetimes of anisole are presented in the range 296 up to 977 K in N_2 and at total pressures between 1 and 10 bar. At temperatures beyond 1000 K, significant pyrolysis takes place. The measurements are completed by studying the effect of O_2 on the fluorescence emission in N_2 with varying amounts of O_2 at 1 bar total pressure. As in air the mixture ignites at high temperature, the maximum temperature was limited to 775 K.

The effect of laser fluence on the fluorescence lifetime of anisole vapour was investigated to determine the limits of the linear regime (cf., Figure 39, left panel), which was found to be 33 mJ/cm² at 296 K. The anisole number density was held nearly constant at 5×10^{22} m^{-3} for all temperatures, corresponding to a partial pressure of 2 mbar at 296 K. In additional measurements it was tested that at this number density self-quenching can be neglected (cf., Figure 39, right panel).

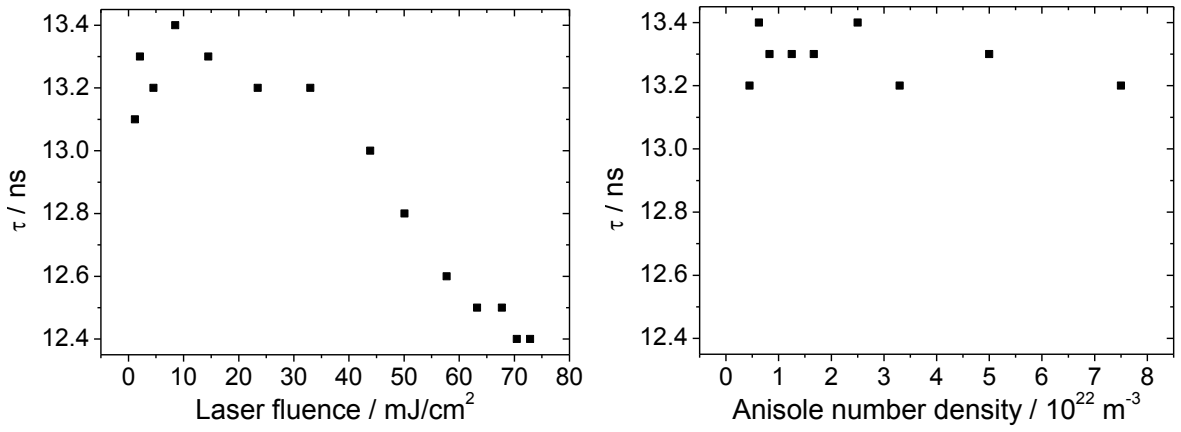

Figure 39: Anisole fluorescence lifetime vs. laser fluence (left panel) and anisole number density (right panel). The limit of the linear regime was defined for a laser fluence of 33 mJ/cm², anisole self-quenching can be neglected for all investigated number densities.

Temperature and pressure dependence in the absence of oxygen

Figure 40 shows the variation with temperature of anisole fluorescence spectra in 1 bar N_2 normalised to their respective peak intensities. At room temperature, emission extends from roughly 270 to 360 nm with a maximum close to 290 nm. Within the spectral resolution of about 3 nm no fine structure is observed, even at low temperatures, and the spectral shape does not change with increasing pressure. The peak maximum shifts by about 3 nm to the red per 100 K temperature increase and the signal in the long-wavelength tail becomes stronger resulting in an increased FWHM (cf., Figure 41). The spectral shift was defined as the shift of the 50% (relative to the peak) intensity point in

the long wavelength tail of the spectrum, since the shift of the peak position cannot be accurately determined because of variations in the relative peak maxima with increasing temperature. The spectrum at room temperature is in good agreement with the result of Hirasawa *et al.* for anisole vapour at room temperature upon 266 nm excitation [19] when comparing the peak position (292 nm) and the FWHM (32 nm) with our values of 292 nm and 30 nm, respectively.

At temperatures above 850 K the spectra change their shape which is attributed to pyrolysis (cf., Figure 40). One possible explanation is that at higher temperatures both anisole and its pyrolysis products in the probe volume are excited by the laser radiation and their respective fluorescence spectra overlap in the imaged wavelength region. The signal intensity of fluorescence from these pyrolysis products is low, in the same order of magnitude as the anisole signal at 775 K. It is assumed that the spectrum at 977 K is dominated by the presence of pyrolysis products in the probe volume after partial or complete decomposition of anisole, resulting in a significant increase in spectral red-shift and FWHM (cf., Figure 41), but the signal intensity stays constant at the mentioned low level. For detailed discussion about the thermal decomposition of anisole and its initial pyrolysis product, the phenoxy radical, see [170] and references therein.

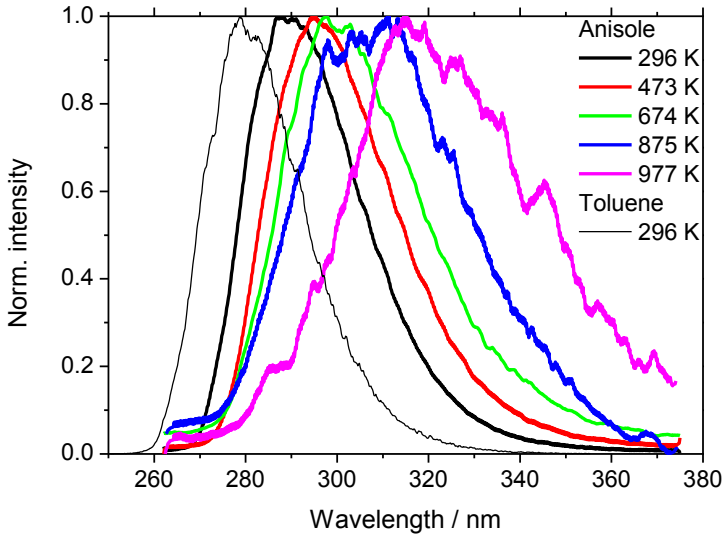

Figure 40: Peak-normalised fluorescence spectra of anisole at various temperatures in 1 bar N_2 with 5×10^{22} m^{-3} anisole. For comparison a toluene LIF spectrum (in 1 bar N_2 at 296 K) is also shown.

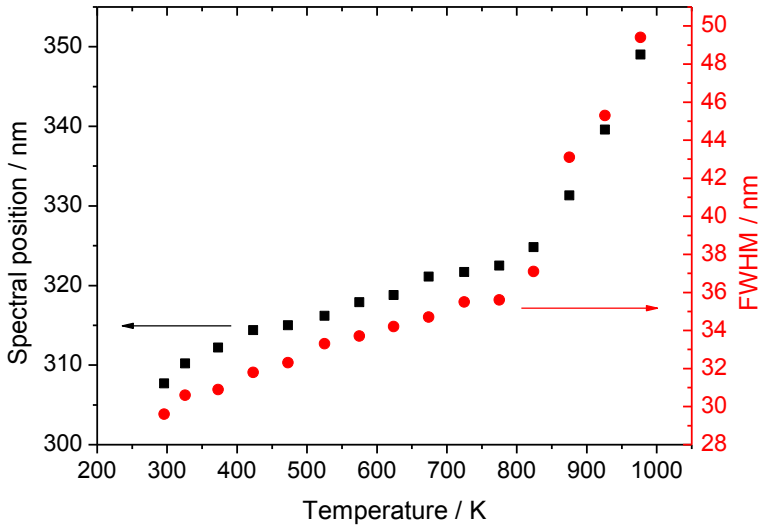

Figure 41: Spectral shift (black squares) and FWHM (red circles) of anisole fluorescence spectrum vs. temperature in 1 bar N_2. The spectral position is defined as the wavelength of the 50% intensity drop in the red tail of the spectrum, see text.

The present work has shown that with 266 nm excitation the fluorescence spectrum of anisole at room temperature is red-shifted by 10–15 nm with respect to that of toluene. This is attributed to the smaller energy gap between the S_0 and S_1 states defined by the size and the electron density of the aromatic π-system. Generally, when the size of the π-system increases in aromatic species, the fluorescence emission is red-shifted [7]. When changing from toluene to anisole, the number of aromatic rings does not change. However, on the one hand, the methoxy group is a strong electron donor and thus increases the electron density in the aromatic ring [80]. On the other hand the π-system is enlarged by the lone pairs of the methoxy group and thus the π–π* transition is shifted to lower energies [171]. Both effects will contribute to the observed spectral shift in comparison to the emission spectrum of toluene.

The results in Figure 40 suggest that anisole would be a suitable tracer for two-colour temperature imaging in typical LIF applications as demonstrated previously for toluene (e.g., [22]). When regarding the increased spectral shift with temperature compared to toluene the sensitivity is expected to be increased. Together with the increased signal strength new diagnostic strategies might open up.

Figure 42 shows effective fluorescence lifetimes of anisole as a function of temperature for several pressures in N_2. In the investigated temperature range the lifetime decreases from 13.3±0.5 ns at 296 K to 0.05±0.01 ns at 875 K, with an increasing slope at higher temperatures. In N_2 the influence of the total pressure is small at low temperature, but it increases with temperature up to around 600 K. In total, the pressure influence is lower than observed for toluene.

At room temperature, the effective fluorescence lifetime of vapour-phase anisole of 13.3 ns is almost pressure independent and thus fits well to the value for anisole dissolved in liquid cyclohexane, reported as 11.1 ns [80]. For anisole, a biexponential fluorescence decay was observed already at room temperature while for toluene a second lifetime component is observed only at temperatures above 500 K for the same excitation wavelength [58]. The fast decay component, however, has a small amplitude for all temperatures making meaningful data evaluation impossible.

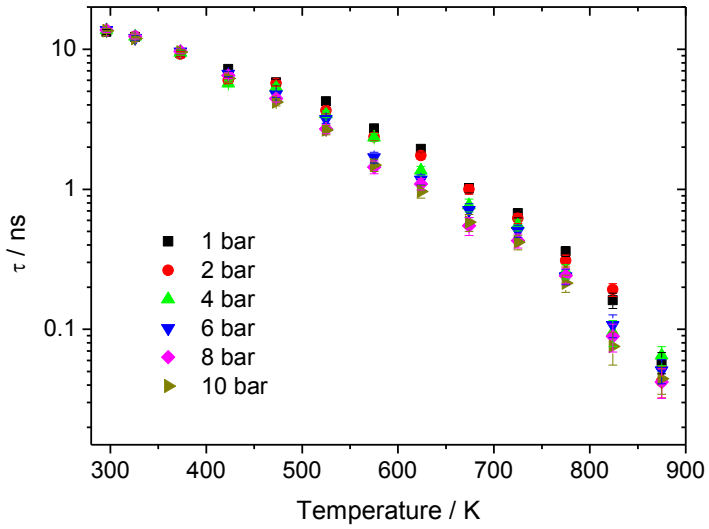

Figure 42: Effective fluorescence lifetimes of anisole in N_2 as a function of temperature for various pressures.

The decrease in fluorescence lifetime of anisole with increasing pressure (present but less pronounced than for toluene) is in contrast to the pressure effects known from, e.g., ketones [30, 88] and naphthalene ([71] and this work). This phenomenon can be explained by the fact that – similar as for toluene – with 266 nm photons anisole is excited close to the 0–0 band gap [31] (~1600 cm^{-1} at 300 K), which means that vibronic levels populated in the S_1 state after photon absorption are located below the thermalisation level. In this case, bath-gas collisions lead to a "destabilisation", such that population is transferred into higher lying vibrational levels of S_1, where faster IC and ISC processes reduce the probability for fluorescence emission, thus reducing the fluorescence quantum yield. In the literature (cf., chapter 3.2) this is interpreted as "photo-induced cooling" of the excited state vibrational distribution, followed by collisional heating via bath-gas collisions [65, 164]. This pressure destabilisation effect is also found for other aromatic species when excited near the vibrationless S_1–S_0 transition, e.g., anthracene excited at 365 nm [165]. In contrast to toluene the destabilisation effect in anisole is less pronounced, leading to a reduced pressure sensitivity of fluorescence intensities or lifetimes.

Oxygen quenching

In contrast to toluene, where the O_2 partial pressure does not influence the spectral shape after 266 nm excitation (e.g., [29, 31] and this work), Figure 43 shows a red shift of the anisole LIF spectra with increasing O_2 partial pressure. The FWHM is nearly unaffected by O_2. The red shift is large at low O_2 partial pressures and it saturates at around 100 mbar O_2 (cf. Figure 44). The overall red shift is about 5 nm at 296 K when changing from pure N_2 to air as bath gas. The spectral shift as defined in this work does not depend on temperature up to about 600 K. At higher temperatures the red-shift is less pronounced.

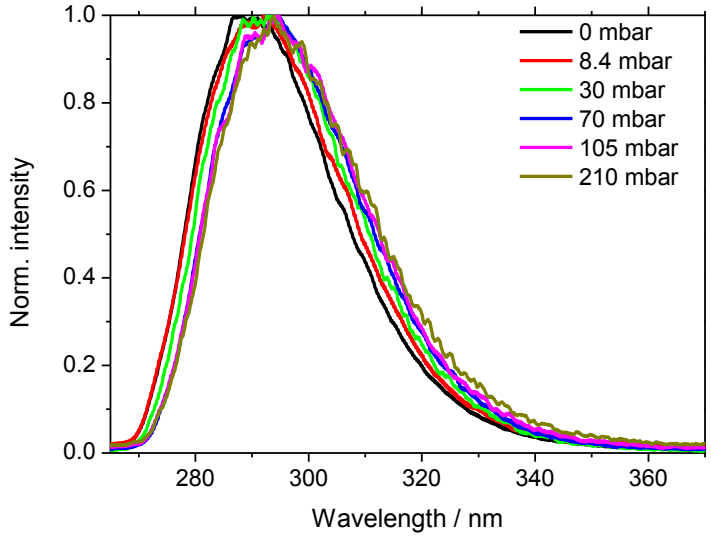

Figure 43: Peak-normalised fluorescence spectra of anisole diluted in N_2/O_2 mixtures for various O_2 partial pressures at 1 bar total pressure and 296 K.

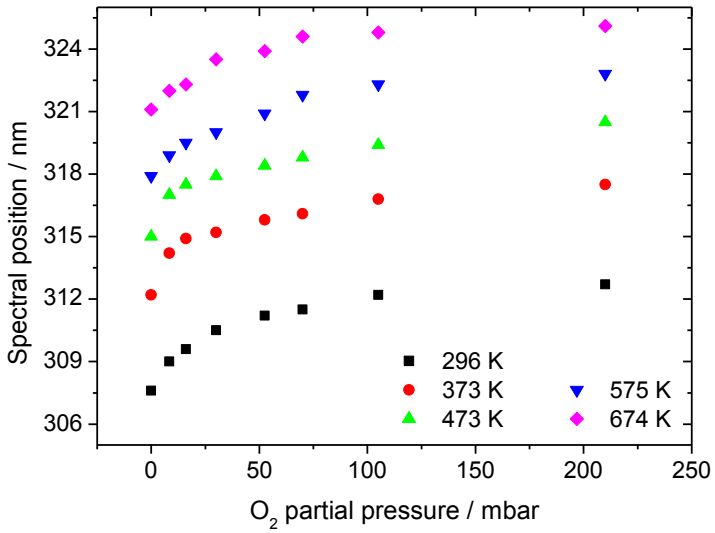

Figure 44: Spectral shift of anisole fluorescence spectrum vs. O_2 partial pressure for several temperatures at 1 bar total pressure. As in Figure 41, the spectral position is defined

as the wavelength of the 50% intensity drop in the long-wavelength tail of the fluorescence spectrum.

Molecular oxygen is a strong fluorescence quencher of the S_1 state in aromatic molecules and thus, also for anisole. Figure 45 shows how O_2 affects the effective fluorescence lifetime of anisole. At room temperature the fluorescence lifetime in air is reduced to 0.40±0.02 ns (compared to 13.3±0.5 ns in N_2). The effect of O_2 quenching decreases with increasing temperature, which is in line with the observations made for toluene and naphthalene (e.g., [20, 29, 31] and this work). In the presence of O_2, with increasing temperature the anisole fluorescence lifetime shows a weak increase at low temperatures due to the decreasing O_2 collision rates before the lifetime-reducing effect of increased temperature dominates (inset in Figure 45). At 775 K, the course of the lifetime with O_2 partial pressure differs from that at lower temperatures which is attributed to ignition of the mixture (the auto ignition temperature of anisole is about 750 K).

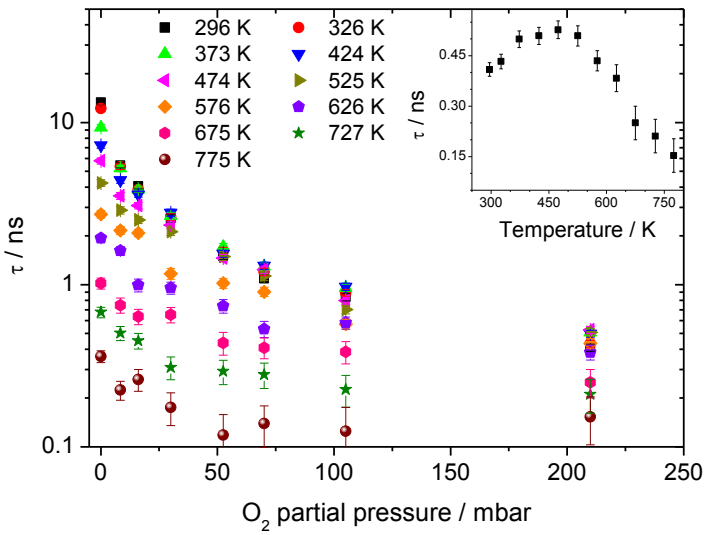

Figure 45: Effective fluorescence lifetimes of anisole diluted in N_2/O_2 mixtures as a function of O_2 partial pressure at 1 bar total pressure and for various temperatures. Inset: Fluorescence lifetimes of anisole as a function of temperature in air at 1 bar total pressure.

From the dependence of effective fluorescence lifetimes on the O_2 concentration (cf., Figure 46, left panel), temperature-dependent Stern-Volmer coefficients (cf., section 3) were derived and are presented in Figure 46 (right panel), together with those of toluene and naphthalene from this work and from Koban *et al.* [29] and Rossow [31] for toluene and from Orain *et al.* [71] and Kaiser and Long [20] for naphthalene. The comparison shows that the O_2 quenching is less effective by about one order of magnitude for anisole compared to naphthalene, but of the same order as that of toluene over the entire temperature range. On the other hand, the temperature sensitivity of the Stern-Volmer coefficient is almost the same as that of naphthalene but somewhat smaller than that of

toluene. This leads to the result that for 300–450 K toluene is more efficiently quenched by O_2 than anisole, whereas above 500 K this order is slightly reversed.

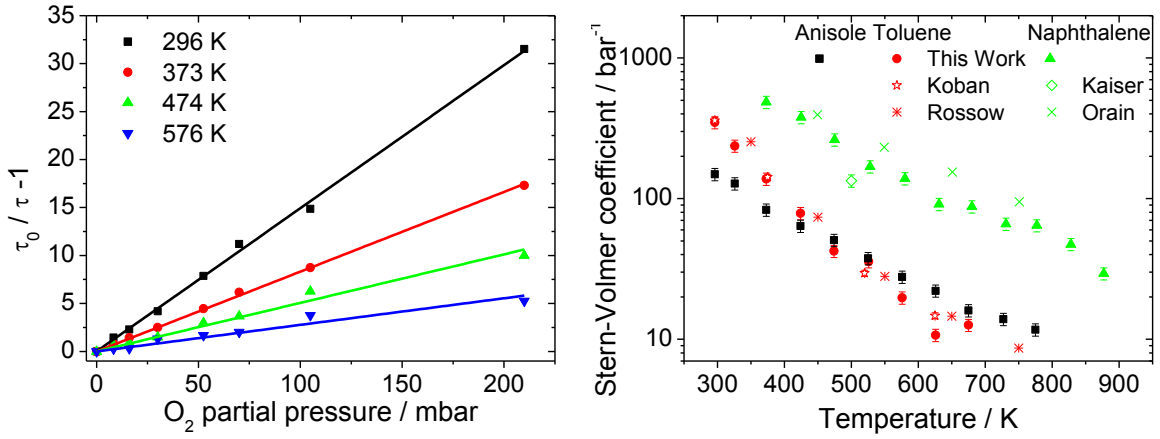

Figure 46: Stern-Volmer plots of anisole fluorescence quenched by O_2 for selected temperatures (left panel). Stern-Volmer coefficients (right panel) for anisole (black), toluene (red), and naphthalene (green) at various temperatures for 1 bar total pressure. Values for anisole of this work (solid black squares) are compared to results from this work and for toluene Koban *et al.* (red open stars [29]), and Rossow (red crosses [31]), and for naphthalene by Orain *et al.* (green crosses [71]), and Kaiser and Long (green open diamond [20]).

Additionally, after 266 nm excitation and in the presence of O_2, anisole behaves similar to toluene excited at 248 nm, i.e., a red-shift of the fluorescence spectrum occurs with increasing O_2 partial pressure [29]. Therefore, for constant temperature environments and for 266 nm excitation the sensitivity of anisole towards O_2 could be used for O_2-concentration measurements via two-colour LIF imaging, as was shown previously for toluene upon 248 nm excitation [54]. The sensitivity, however, would be slightly reduced compared with toluene due to the reduced red-shift, but the applicability of 266 nm excitation can be advantageous. Imaging of O_2 concentrations based on fluorescence lifetimes has been demonstrated for toluene [138]. Hence, it is easy to imagine that this procedure is adaptable for anisole to determine O_2 concentrations or temperatures.

Phenomenological model for anisole

For practical applications of tracer-LIF diagnostics under variable environmental conditions of pressure, temperature and O_2 partial pressure it is desirable to evaluate effective fluorescence quantum yields from a physical model or using analytical functions. Here, an empirical mathematical model was fitted to the obtained experimental fluorescence lifetime data. The model equation (eq. 32) consists of three terms (in square brackets) and calculates a relative fluorescence quantum yield, ϕ_{rel}, which equals unity at 1 bar in N_2 at 296 K. The first term describes the temperature dependence of the relative anisole fluorescence quantum yield at 1 bar in N_2. The second term represents the pressure de-

pendence in N_2 in the absence of O_2. The third term describes the effect of O_2 on the quantum yield with a Stern-Volmer relationship. This functional dependence therefore is of the same form as the one for naphthalene (see above).

$$\phi_{rel} = \left[A_1 + \left(\frac{A_2}{A_3 \sqrt{0.5\,\pi}} \right) \exp\left(-2 \left(\frac{T - A_4}{A_3} \right)^2 \right) \right] \cdot \left[B_1(T) \exp\left(-\frac{p_{tot}}{B_2(T)} \right) + B_3(T) \right] \cdot \left[\frac{1}{1 + k_{SV}(T) p_{O_2}} \right] \tag{32}$$

The respective parameters in the model function are listed in Table 7. Fluorescence lifetimes can be calculated by multiplying ϕ_{rel} with a constant factor of 13.3 ns, as shown in Table 7, last row.

Table 7: Fitting coefficients and polynomials used in the fit-expression (eq. 32) reproducing measured effective fluorescence lifetimes, i.e., the relative fluorescence quantum yield, of anisole, when excited with 266 nm radiation as a function of temperature, O_2 partial pressure, and total pressure. Temperature T is in K, total pressure p and O_2 partial pressure p_{O2} are in bar.

Parameter	Value / expression
A_1	-0.0196
A_2	1548
A_3	607.8
A_4	-58.79
$B_1(T)$	$-1.94 + 0.00777\,T - 5.70 \times 10^{-6} T^2$
$B_2(T)$	$-6.42 + 0.0471\,T - 4.26 \times 10^{-5} T^2$
$B_3(T)$	$2.64 \exp\left(-\frac{T}{261} \right) + 0.235$
$k_{SV}(T)$	$1180 \exp\left(-\frac{T}{140} \right) + 7.85$
τ_{eff}	$\phi_{rel} \times 13.3$ ns

The model is validated for environments with a O_2 partial pressure up to 210 mbar from room temperature to 750 K. For N_2 atmospheres at 1 bar the model is valid up to 850 K. For higher pressures of N_2 the range of validity is limited to 750 K because at higher temperatures calculated values differ by more than twice the error limits from the measured data.

Figure 47 shows the comparison between the fitting functions (lines) and experimental data (symbols) as a function of temperature for three pressures in N_2. Within the scatter

of the data the overall agreement is very good up to about 750 K for all pressures. For 1 bar even up to 850 K, while at higher temperature deviations occur.

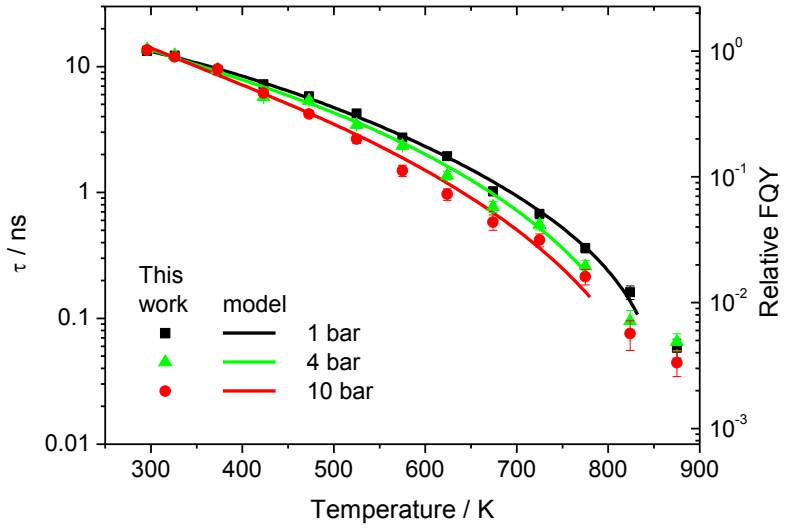

Figure 47: Measured effective fluorescence lifetimes (symbols) of anisole and predictions for relative quantum yield and fluorescence lifetimes by Eq. 32 (lines) as a function of temperature for three pressures in N_2.

Figure 48 depicts a similar comparison between experimental fluorescence lifetimes (symbols) and the model output (solid lines) for several temperatures as a function of O_2 partial pressure and for air as a function of temperature (inset in Figure 48). The agreement is satisfactory.

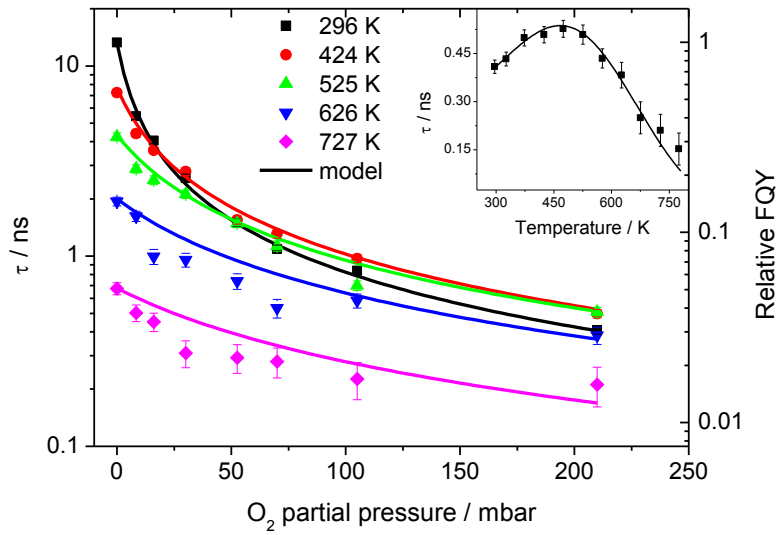

Figure 48: Measured effective fluorescence lifetimes (symbols) of anisole and predictions for relative quantum yield and fluorescence lifetimes by Eq. 32 (lines) as a function of O_2 partial pressure at various temperatures at 1 bar total pressure. Inset: Measured lifetimes vs. temperature in air at 1 bar compared to the model predictions.

It must be emphasised that the fitting model allows the prediction of fluorescence lifetimes and relative fluorescence quantum yields within a limited range of conditions relevant for typical tracer LIF applications. It will be subject of forthcoming work to set up a photo-physical model for anisole similar to the step-ladder model first introduced by Thurber *et al.* [28] for acetone. This would then take into account the vibrational level-dependent internal energy flow and relaxation processes after photo-excitation and would enable a better prediction of fluorescence intensities and lifetimes for temperature and pressure ranges as well as bath gas compositions of interest in future anisole LIF applications.

5.1.4 Acetone

Acetone fluorescence lifetimes were determined at 1 bar total pressure as a function of temperature in N_2 as bath gas (cf., Figure 49). The lifetime decreases with increasing temperature from 1.4±0.1 ns at 296 K down to 0.24±0.06 ns at 925 K. For temperatures below 500 K the measured lifetimes are in accord with data from Ossler *et al.* [107]. At temperatures above 950 K the acetone emission spectrum significantly changes its shape showing evidence of acetone pyrolysis. Chapter 5.2 will deal with this topic.

The measured lifetimes were compared to existing fluorescence models. The first photophysics model for acetone was described by Thurber [28]. After normalising the calculated fluorescence quantum yields from these models with the measured lifetime at room temperature, the model function is plotted in Figure 49 as solid line. The measured lifetime values are satisfactorily described by the model up to 500 K, however, they are significantly smaller at temperatures above 550 K. Thurber's model was later applied to 3-pentanone, and the most recent modification by Cheung and Hanson [85] was made for this 3-pentanone model. As the modelled and measured lifetime values differ significantly from each other it was one idea to check if an improved model might solve this discrepancy. Therefore, parameters for acetone from Thurber were used with these most recent modifications to model acetone fluorescence quantum yield (cf., Figure 49). Both model functions follow the same trend, but do not reflect the evolution of the measured fluorescence lifetime at temperature above 550 K.

One reason for these deviations might be that – as outlined in chapter 2.2.3 – acetone partly decomposes upon illumination at 266 nm. Especially with picosecond laser excitation and the corresponding high photon density this may enhance the decomposition and hence influence the fluorescence properties. Though the spectrum is not affected, the fluorescence lifetime might be shortened. In the case of the experiments of Ossler *et al.* [107] (cf., Figure 49) this effect could be overcompensated by the low temporal resolution of their detection system.

Satisfactory explanations for this discrepancy, however, are not available yet.

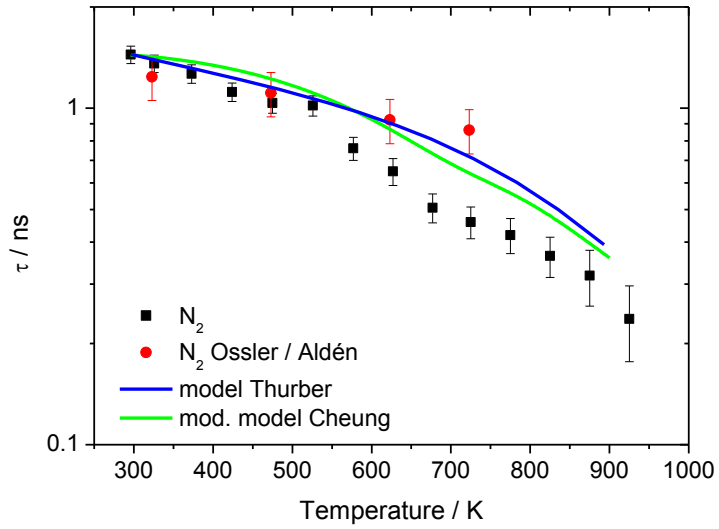

Figure 49: Effective fluorescence lifetimes of acetone as a function of temperature in 1 bar N_2 (solid symbols). Fluorescence lifetimes reported by Ossler *et al.* [107] are added as open symbols. Lines are lifetimes calculated from the original fluorescence yield model presented by Thurber *et al.* [28] and the modified model from Cheung and Hanson [85]. See text for details.

5.1.5 3-Pentanone

3-Pentanone fluorescence lifetimes were determined at 1 bar total pressure as a function of temperature in N_2, CO_2, and air as bath gases (cf., Figure 50). The lifetime decreases with increasing temperature from 2.6±0.1 ns at 296 K down to 0.15±0.02 ns at 925 K which indicates a higher sensitivity with respect to temperature than acetone. At this pressure the influence of the bath gas can be neglected within the error limits, which is in accord with previous data of the quantum yield [85, 172]. For temperatures below 500 K the measured lifetimes are in accord with literature values from Ossler *et al.* [107]. At temperatures above 975 K in N_2 and CO_2 the 3-pentanone fluorescence spectrum changes shape and new peaks appear indicating that 3-pentanone is partly or fully decomposed. Chapter 5.2 will deal with this topic. In air, the upper temperature limit is at 775 K due to mixture ignition under the experimental conditions of this thesis.

The latest version of the step-ladder fluorescence model presented by Cheung and Hanson [85] for modelling the quantum yield of 3-pentanone was applied to the present lifetime measurements. As shown in Figure 50 the measured lifetime values show satisfactory agreement with the model predictions. Model predictions for measurements in air are very slightly smaller than the ones in N_2 and thus not shown in Figure 50. The presented measurements correctly reflect this trend as they are in a similar way slightly smaller than the measured lifetimes in N_2.

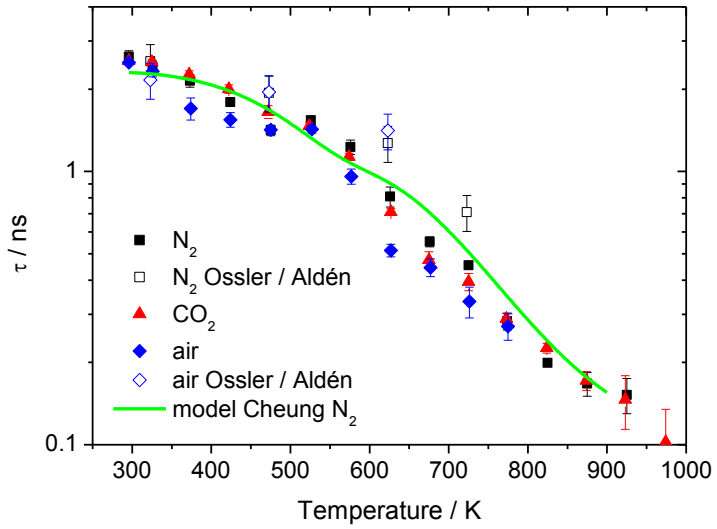

Figure 50: Effective fluorescence lifetimes of 3-pentanone as a function of temperature for different buffer gases at 1 bar total pressure (closed symbols). Fluorescence lifetimes reported by Ossler *et al.* [107] are added as open symbols. The line corresponds to lifetimes calculated for N_2 as bath gas from the fluorescence yield model presented by Cheung and Hanson [85].

5.2 Tracer pyrolysis

Previous investigations of tracer photophysics were mostly limited in temperature by the maximal achievable temperature of the apparatus and not by degradation of the tracer molecules themselves. The high achievable temperatures in the present setup together with the comparably long residence time in the hot zone in the range of a few seconds can cause significant tracer pyrolysis and thus LIF measurements on possibly formed intermediate species.

The diagnostic potential of these pyrolysis products has never been explored in literature. Measurements in this thesis will help to indicate whether pyrolysis products may be suitable indicators for tracer degradation, or intermediate stages of fuel decomposition. Both “markers” of reaction progress might, however, be strongly dependent on ambient conditions. It also should be kept in mind that the typical gas residence times in the cell are in the range of a few seconds which is much longer than in many high-temperature applications such like in IC engines.

5.2.1 Ketones

In the following, the pyrolysis of acetone will be discussed exemplarily. The pyrolysis kinetics of 3-pentanone take place along similar routes at slightly higher temperatures (about 20–30 K higher) and with a comparable product spectrum [173].

Fluorescence spectra were obtained in the cell at temperatures which will lead to appreciable tracer decomposition during the residence time within the heated zone. The residence time in the hot zone of the cell was varied by changing the flow rate of the carrier gas. Thus, deviations in the emission spectra with varying residence time allow to identify which emitting species is mainly formed at a certain temperature.

The recorded emission spectrum of acetone begins to change at 976 K. As displayed in Figure 51 the spectrum starts to deviate from the known spectral shape of acetone (cf., Figure 10) due to disturbances from pyrolysis products exhibiting blue-shifted components for the longest explored residence time of 6 s (black curve). Decreasing the residence time in the hot zone by increasing the volumetric flow rate clearly indicates that at this long residence time, pyrolysis reactions have occurred. For the short residence times of 3 and 2 s, the typical spectral signature of acetone is the only visible emission. The thermal decomposition of acetone has been widely explored. The most recent mechanism by Pichon *et al.* [174] was used to model the pyrolysis using CHEMKIN [175]. Following this mechanism the first visible pyrolysis product is assumed to be ketene ($H_2C=C=O$). Ketene shows absorption at 266 nm [176] and due to the carbonyl structure it is not unlikely that it also fluorescence the wavelength range of 280–380 nm (cf., Figure 51). Future work needs to verify if the emission observed here is really caused by ketene.

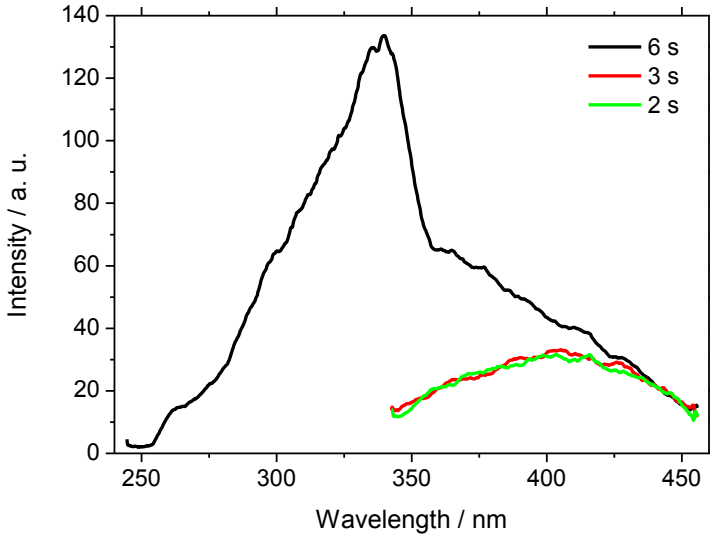

Figure 51: Emission spectra of acetone disturbed by the first visible pyrolysis product around 350 nm, probably ketene, after 266 nm excitation, at 976 K in 1 bar N_2 for three residence times in the hot zone of the cell.

For even higher temperatures (1026 K) the typical acetone emission spectrum completely disappears. Only the first detectable pyrolysis product (probably ketene) is visible with enlarged intensity compared to the measurement at 976 K. Again the emission intensity increases with increasing residence time in the hot zone of the cell meaning that this product is generated in-situ while acetone is flowing through the cell.

A further temperature increase to 1076 K yields a second detectable pyrolysis product, again more pronounced for longer residence times in the heated zone (cf., Figure 52) combined with a further increase in intensity compared to the lower temperatures. Following the mentioned mechanism by Pichon *et al.* [174] the second major pyrolysis product of acetone occurring at high temperatures is carbon monoxide CO. Absorption of CO, however, takes place in vacuum UV at wavelengths below 200 nm. Thus, two-photon absorption is normally used to excite CO. For diagnostic purposes, excitation wavelengths around 217 nm (e.g., [177]), 230 nm (e.g., [178]), or 280 nm (e.g., [179]) are typically used. Excitation at 266 nm would be a very unusual wavelength to excite carbon monoxide. Chan *et al.* [180], however, report absorption of CO molecules amongst others in the wavelength range 120–140 nm. Therefore two-photon absorption processes with 266 nm radiation could be possible, especially when – like in this thesis – a picosecond laser is used. Validation experiments with only CO in Ar as bath gas, however, yielded no visible fluorescence upon 266 nm excitation [181]. Thus, other species are supposed to cause the measured spectrum.

Another species formed under these conditions in significant concentration is the ethynyl radical (C_2H). Its absorption spectrum is located in the UV and suggests suitable absorption at 266 nm [182]. Studies dealing with ethynyl fluorescence are not available in literature. Radicals, however, are typically not stable enough to be present in sufficient concentrations over a few seconds. In addition, it must be emphasised that the residence time in a shock tube (~1 ms), where the mechanisms is derived from, is about three orders of magnitude smaller than the residence time in the cell of this thesis (few seconds). This may cause discrepancies between real and modelled species concentrations. Thus, the nature of this second pyrolysis product remains unknown. This species is most likely a product of secondary reaction (i.e., not a primary product of pyrolysis, but a reaction product formed from primary decomposition species). Future work, for example by analysis of the product gas composition with gas chromatography / mass spectrometry (GC/MS) must be done to clearly identify the pyrolysis products.

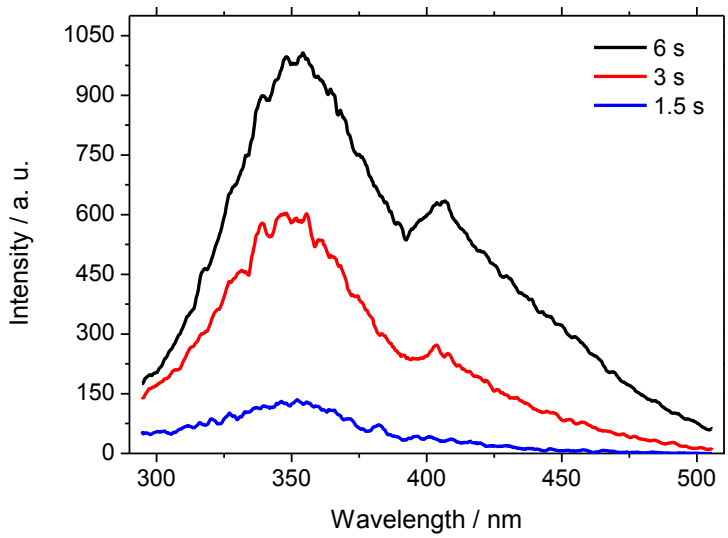

Figure 52: Emission spectra of the first pyrolysis product (probably ketene) around 350 nm and combined with beginning formation of the second pyrolysis product (or secondary reaction products) around 450 nm of acetone at 1076 K in 1 bar N_2 depending on the residence time in the hot zone of the cell.

When further increasing the gas temperature, the second spectral peak gets even more pronounced and the first product begins to disappear. For a temperature of 1202 K (cf., Figure 53) this effect is clearly visible as seen in the residence-time-dependent emission spectra. For residence times of 1.5 and 3 s the first pyrolysis product (which is assumed to be ketene) dominates the spectrum while at 6 s residence time the spectrum is dominated by the second product.

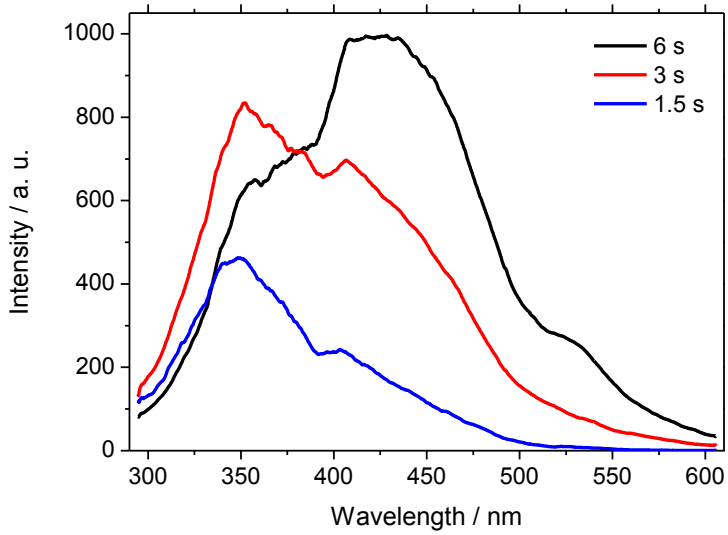

Figure 53: Emission spectra of the first (probably ketene) and the second pyrolysis product of acetone at 1202 K in 1 bar N_2 depending on the residence time in the hot zone of the cell.

5.2.2 Aromatics

In contrast to ketones, significant pyrolysis of toluene and naphthalene affects the fluorescence spectrum at much higher temperatures. At temperatures above 1200 K pyrolysis products first influence the emission spectrum and hinder the clear detection of the parent tracer molecule.

For anisole, however, the spectrum is only slightly affected (cf., section 5.1.3) und does not show any spectral changes with further increasing temperature. The intensity is reduced with temperature meaning anisole and its initial pyrolysis product, respectively, decompose. Secondary reaction products are not visible upon 266 nm excitation. Thus, anisole pyrolysis is not further investigated here.

Toluene

The mechanism of toluene pyrolysis has been a subject of investigation in several studies (cf., [183-184] and references therein). Although absorption spectra in the UV/Vis of several intermediates and products are known, none of these studies consider fluorescence emission of these species after 266 nm excitation. Very recently, however, Zabeti *et al.* started to measure LIF spectra of these pyrolysis products [181] in a shock tube. Measurements of this thesis using the presented cell arrangement allow an alternative approach to these pyrolysis species.

The mean residence time of the gas mixture in the heated section of the cell is in the range of a few seconds. Modelling the toluene pyrolysis using CHEMKIN [175] with the mechanism presented by Andrae *et al.* [183] and Zhang *et al.* [184] revealed that at temperatures higher than 950 K toluene begins to decompose on similar time scales as in the presented cell experiments. Although both mechanisms suggest toluene pyrolysis occurring already at temperatures around 1000 K, for the present conditions spectra are affected only above 1200 K (cf., Figure 54). At lower temperatures the concentration is assumed to be too low to detect fluorescence signals. At 1228 K and for residence times of 3 and 1.5 s “normal” toluene emission is visible with a peak around 320 nm with some additional spectral features at around 400 nm and longer wavelengths originating from decomposition product(s). At 6 s residence time the toluene signature is completely gone and the spectrum only originates from these pyrolysis product(s), which amongst others might be ascribed to benzyl radicals. For this long residence time enhanced laser stray light is visible, presumably due to soot particles.

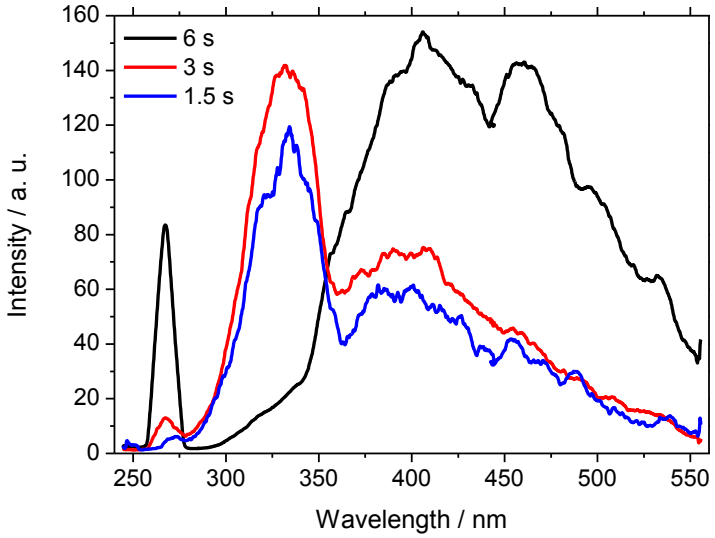

Figure 54: Emission spectra of toluene, its pyrolysis product(s), and (maybe) secondary reaction products at 1228 K in 1 bar N_2 depending on the residence time in the heated zone of the cell. The clearly visible laser stray light around 266 nm is due to particle formation.

Two major initial pyrolysis products of toluene are presented in literature: On the one hand the decomposition in phenyl and methyl radicals, on the other hand in benzyl and hydrogen radicals. While the latter one is preferentially formed at rather low temperatures, the formation of the first one is in favour at higher temperatures. Both benzyl and phenyl, however, show absorption at 266 nm [185-186]. Benzyl radicals are known to show fluorescence [187], excitation, however, was in the visible range of light.

Comparing the reaction times in the measurement cell of this thesis (about a few seconds) to those of a shock tube (typically ~1 ms) where the mechanisms are derived from there is concern if the mechanisms can easily be adapted to the presented cell measurements. Radicals are normally too unstable to be present in sufficient concentration over a few seconds. Secondary reaction products like, e.g., anthracene or fluorene (or a mixture of them) could also cause fluorescence. Thus, future work must verify which species causes the observed spectra.

Naphthalene

As it can be seen in Figure 55 for the present conditions naphthalene pyrolysis takes place at temperatures above 1200 K with products emitting fluorescence red-shifted compared to the parent species. Undecomposed naphthalene can be observed at the peak and the shoulder, respectively, around 340 nm. In addition it can be observed that two peaks emerge at longer wavelengths, one around 380 nm, and the other around 450 nm.

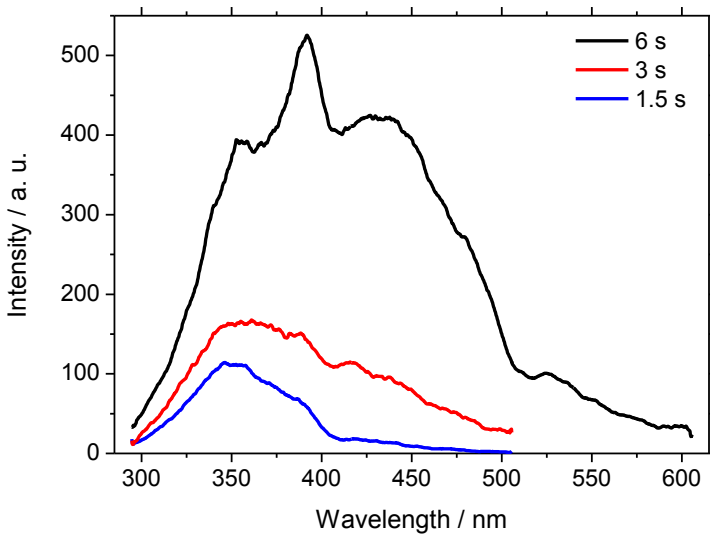

Figure 55: Fluorescence spectra of naphthalene and its pyrolysis products at 1228 K in 1 bar CO_2 depending on the residence time in the hot zone of the cell.

Naphthalene is an important intermediate in the soot formation process. The initial step of naphthalene pyrolysis is the H abstraction and the formation of the naphthyl radical [188]. Spectral properties of this species, however, are not known in literature. The naphthyl radical exhibits a similar molecular structure as the phenyl radical. Thus, it is not unlikely that naphthyl radicals also absorb UV light at 266 nm and show fluorescence which in this case is located from about 350 to 550 nm. The double-peak structure of the fluorescence spectrum may occur due a vibrational structure in the spectrum or due to the fact that in principle two different naphthyl radicals (α-naphthyl and β-naphthyl) are formed which may exhibit slightly different fluorescence spectra. In the same way as for toluene it is uncertain if radicals can in principle be detected with this experiment or if the emission is caused by (a mixture of) secondary reaction products like, e.g., pyrene or other higher polycyclic aromatic compounds.

5.3 Imaging applications: Injector experiments

The investigations in section 5.1 yielded in the conclusion that anisole as a new fluorescent tracer shows promising photophysical properties for typical LIF imaging studies. Applications of anisole as tracer for LIF imaging, however, are not available in literature yet. In previous studies, tracer comparisons were seldom performed. If done, they were only based on cell measurements and only on a qualitative way. Rossow compared several tracers at 450 K [31], whereas Hirasawa *et al.* compared several tracers at room temperature [19]. Comparing imaging experiments, however, are not available. As closure of this thesis, anisole was compared to the established tracers toluene, naphthalene, and acetone in a simple LIF imaging arrangement to characterise the imaging capabili-

ties of anisole relative to the other established tracers. All three aromatics were studied in both N_2 and air as bath gas. Acetone was studied in N_2 only because it is known that the influence of O_2 quenching is minor. This allowed to reduce the number of experiments which turned out to be important because the gaskets in the gas valve were affected by acetone. Results of interest are the signal per molecule, the signal per volume that can be reached with a bubbler system and possible deviations in flow structure because all investigated tracers show differences in boiling point and vapour pressure and hence might differ in gas transport properties.

As experimental configuration a transient gas jet impinging on a flat wall was investigated via tracer-LIF imaging. Originally, the experiment was built to investigate the jet impingement on the piston bowl frequently encountered in the leading vaporised fuel jet modern Diesel engines [189] under simplified geometric conditions. For this purpose a fast-acting Hoerbiger GV 50 gas valve was selected. As the injector is symmetric the jet is wilfully not centred onto the camera image, but shifted to the left to allow a larger aspect ratio and thus to better visualise the jet structures after colliding with the wall. The investigation was performed in collaboration with Martin Goschütz (IVG, University of Duisburg-Essen) which is gratefully acknowledged by the author of this thesis.

5.3.1 Experimental arrangement and data evaluation

The experimental arrangement is shown in Figure 56. Two mass-flow controllers (Bronkhorst) and a single-step bubbler system delivered the gas mixture of carrier gas and tracer for the injector stored in a 25 l vessel with an overpressure of about 16 mbar (measured with a pressure transducer). The original exit diameter of 30 mm of the gas valve is reduced by a convergent conical nozzle to about 10 mm, providing a uniform velocity profile. The injection time was held constantly at 65 ms. The jet is injected from the top into a housing of 250×250×400 mm^3 with an endplate 200 mm downstream of the injector. The housing can be flushed with the bath gas. Experiments were carried out in either pure N_2 (delivered by evaporated liquid N_2) or pure air (delivered by compressed and dried ambient air). The housing is equipped with two quartz windows (size: 200×200 mm^2) arranged at right angles for optical access. After passing through the region of interest, the laser beam is caught by a beam dump inside the housing.

The optical arrangement is a classical LIF imaging setup also depicted in Figure 56. The output of a nanosecond double-pulsed frequency-quadrupled Nd:YAG laser was formed to a light sheet of ~200 mm height and a thickness of 0.5 mm via two cylindrical lenses. The repetition rate was 12.5 Hz with a pulse width of 10 ns and. The double pulse laser was used with a 50 ns delay in between the two pulses to double the available laser energy without risking saturation. The total excitation energy was about 50 mJ corresponding to 20 mJ/cm^2 for the combined pulses which was below the saturation limit of all used tracers (cf., section 5.1). Fluorescence emission was collected perpendicular to

the laser sheet by a f = 45 mm $f_\#$ = 1.8 UV camera lens (Cerco) and imaged on an intensified 12 bit CCD camera (Imager Intense, LaVision). In front of the camera lens a long-pass filter (Semrock RazorEdge LP02-266RS-50) was mounted to suppress laser stray light. Laser, camera, and injector were synchronised with a timing board (PTU, LaVision) and a pulse delay generator (BNC 575). The gain factor of the intensifier was adjusted in a way that for each condition of tracer and bath gas the maximum intensity was below the saturation limit of the detector.

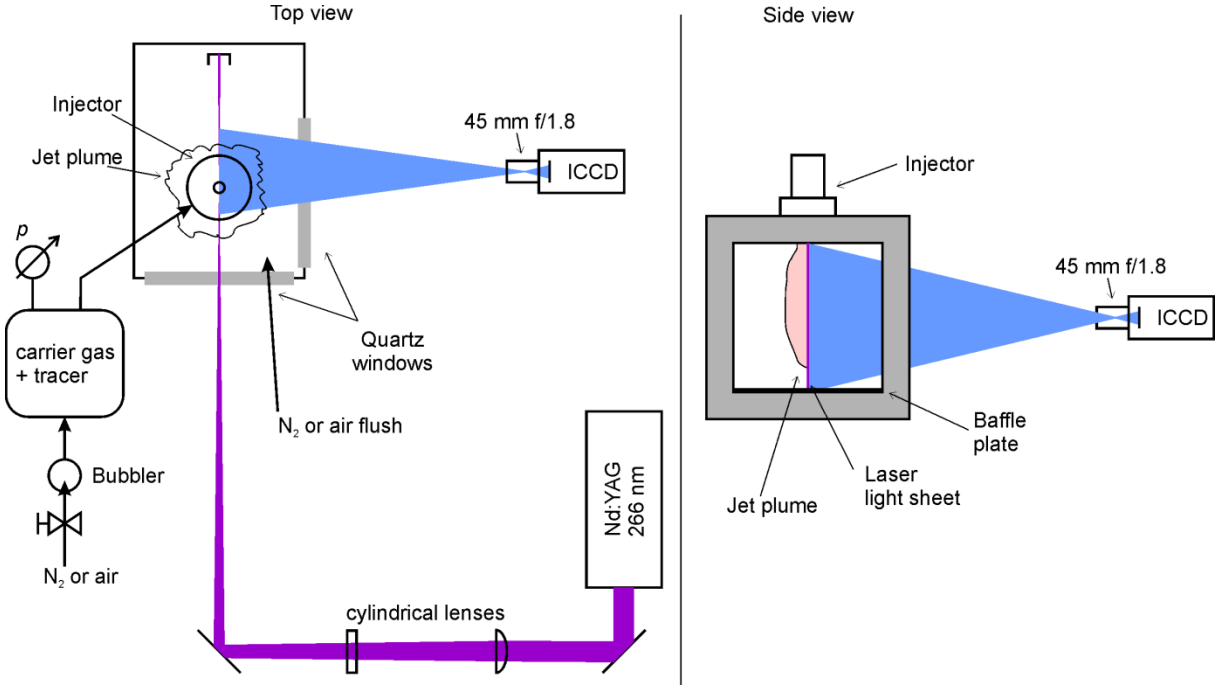

Figure 56: Experimental arrangement of the injector experiment. Left panel: Top view. Right panel: Side view through the laser entrance window. The laser light sheet formed by the cylindrical lenses was 200 mm high and 0.5 mm thick. The injector is wilfully not centred on the optic axis of the camera lens; for details see text. Both gas flows (carrier gas and flush) were either N_2 or air.

All investigated tracer substances were used without further purification. Toluene, anisole, and acetone were used as pure substances. Naphthalene, which is solid at room temperature, was dissolved in dodecane which was tested to show no fluorescence upon 266 nm radiation.

Each image was taken in a separate injection event. Thus differences in jet structure are unavoidable due to the turbulent nature of the jet. Two series of experiments were performed: Firstly, a time series, where the delay between the laser pulse and the injection was varied to yield information of the jet propagation and the collision with the wall. Secondly, a series of 50 images at one constant delay time was taken to characterise the fluctuations of the jet.

For each condition (each tracer, N_2 and air) a background image was recorded (average of 200 images) with the laser firing and pure bath gas inside the housing. Equally, for each condition the housing was filled homogeneously with the used tracer to record a flat

field with the spatial distribution of laser energy within the light sheet (average of 300 images). For each jet image, the background was subtracted and the intensity was corrected for spatial inhomogeneities using the respective flat field. Laser attenuation was below 10% across the observed flat field.

In additional measurements, a calibration curve for the used intensifier gain factors was determined to allow for a comparison of the measured signal intensities for all measurements. Measured signal intensities were corrected for the spectral sensitivity of the detection system by using manufactures' transmission and sensitivity curves for the used components, respectively (cf., Figure 57). The (relative) number density of each tracer was theoretically calculated by assuming that the gases contain the tracer at its respective vapour pressure in the calibration measurement. To verify this assumption, the evaporation rate was measured based on the time-dependent weight loss of the bubbler and the resulting tracer number density was calculated using the ideal gas law. These experimentally determined values were used to compare signal intensities for the various tracers on a per-molecule basis.

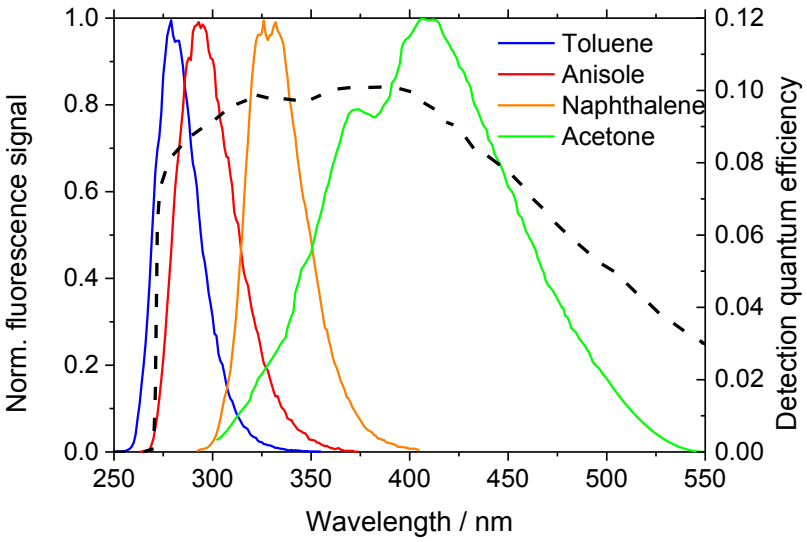

Figure 57: Peak-normalised fluorescence spectra (solid lines) of the tracers used here and spectral quantum efficiency (dotted line) of the detection system long-pass filter + UV camera lens + intensified camera.

5.3.2 Results

LIF images are shown in Figure 58 with anisole as tracer in N_2 bath gas for various delays after the start of injection (SOI). After SOI the gas flow needs some time to propagate towards the measurement volume. Thus, for the initial 6 ms after SOI only a small pre-pulsing forerun is visible, probably resulting from residuals from the previous injection. At 20 ms after SOI the main part of the gas jet becomes visible. In the following the

jet propagates (40 ms) until it impinges on the wall at the end of the measurement volume (60 ms). At 80 ms the injection has stopped, but there is still some wake jet visible originating from a small leak in the gas valve or rests of tracer vapour emanate from the convergent nozzle in front of the gas valve. The main jet, however, has impinged on the wall and spread over a large spatial area. Further images for delay times beyond 80 ms after SOI (not shown here) show a dispersion of the jet over a large spatial region with low tracer concentration and thus low signal intensity. In conclusion, the jet behaves like a typical turbulent free jet impinging on a wall.

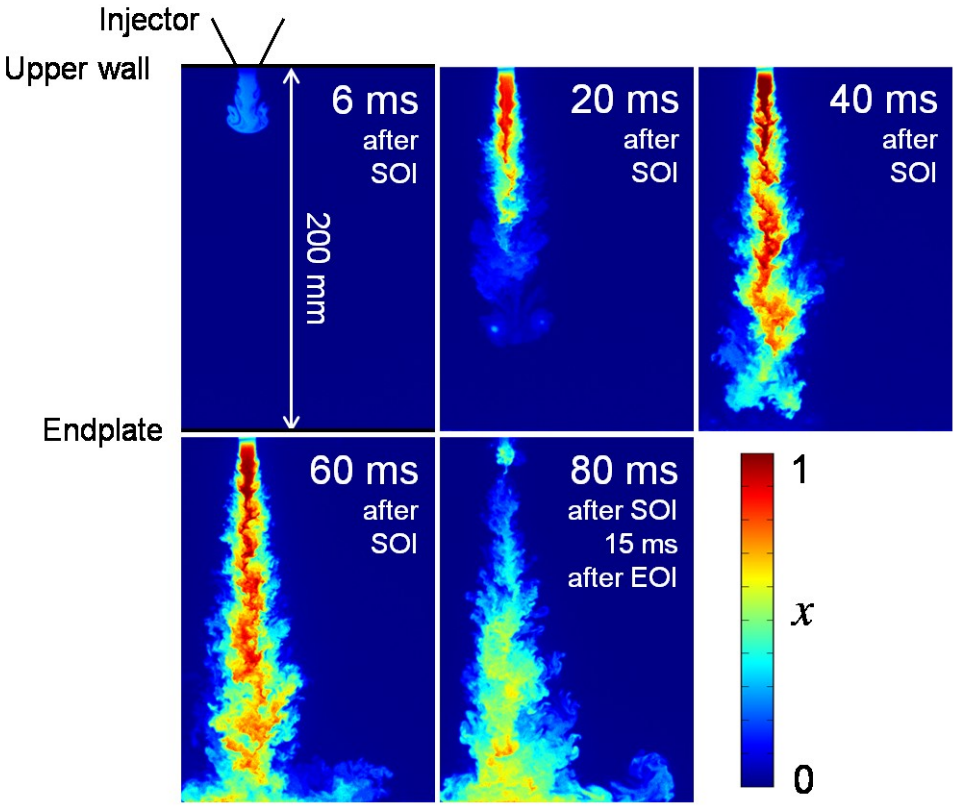

Figure 58: Anisole-LIF images of the impinging turbulent jet for different delays after start of injection (SOI) for N_2 as bath gas. Excitation energy was 25 mJ/cm² at 266 nm. EOI means End of Injection.

Figure 59 compares measurements with the four tracers in both N_2 and air as bath gas with the tracer concentration provided by the single-stage bubbler system (i.e., very different resulting tracer number densities for the different species, cf., Table 9). The intensity-normalised images each show a single realisation of the jet at 58 ms after SOI with a high-magnification inset to give a rough indication of the impact of noise on the image. For comparison of the absolute intensities, cf., Figure 60. Because of the stochastic nature of turbulent flows, Figure 59 cannot serve as a stringent comparison of the achievable measurement precision and spatial resolution. It does, however, provide results from a typical target application of LIF imaging, non-reacting turbulent mixing.

The main finding from Figure 59 is that at the coarse resolution provided by the scaled-down images in this thesis, all cases deliver images suitable for single-shot wide-field

visualisation, even naphthalene in air with its low vapour pressure and its efficient quenching by O_2. Thus, all four tracers are in principle suitable for imaging gas mixing-processes at temperatures significantly below the tracers' boiling points. Considering the wide range of physical and photo-physical properties, this is not a trivial result.

The magnified insets in Figure 59 are positioned to show a fixed-size region with high scalar gradients in the outer mixing layer of the jet. Here, differences between tracers are noticeable. The images from the aromatic tracers have better signal-to-noise ratio (SNR) in nitrogen than in air, particularly in the case of naphthalene. As expected, fluorescence from the aromatic tracers is much lower in air than in N_2 due to quenching by O_2. Anisole provides very strong signal even in air, confirming that it could be a tracer with high potential in LIF diagnostics. The often used ketone acetone shows a rather low signal which is due to its small absorption cross-section and its low fluorescence quantum yield. In air, however (not directly tested here) acetone becomes competitive due to its insensitivity to quenching by O_2. With respect to the other tracers, anisole shows very strong signal even in air, again confirming the results and discussions in section 5.1.3 that anisole should be a tracer with high diagnostics potential.

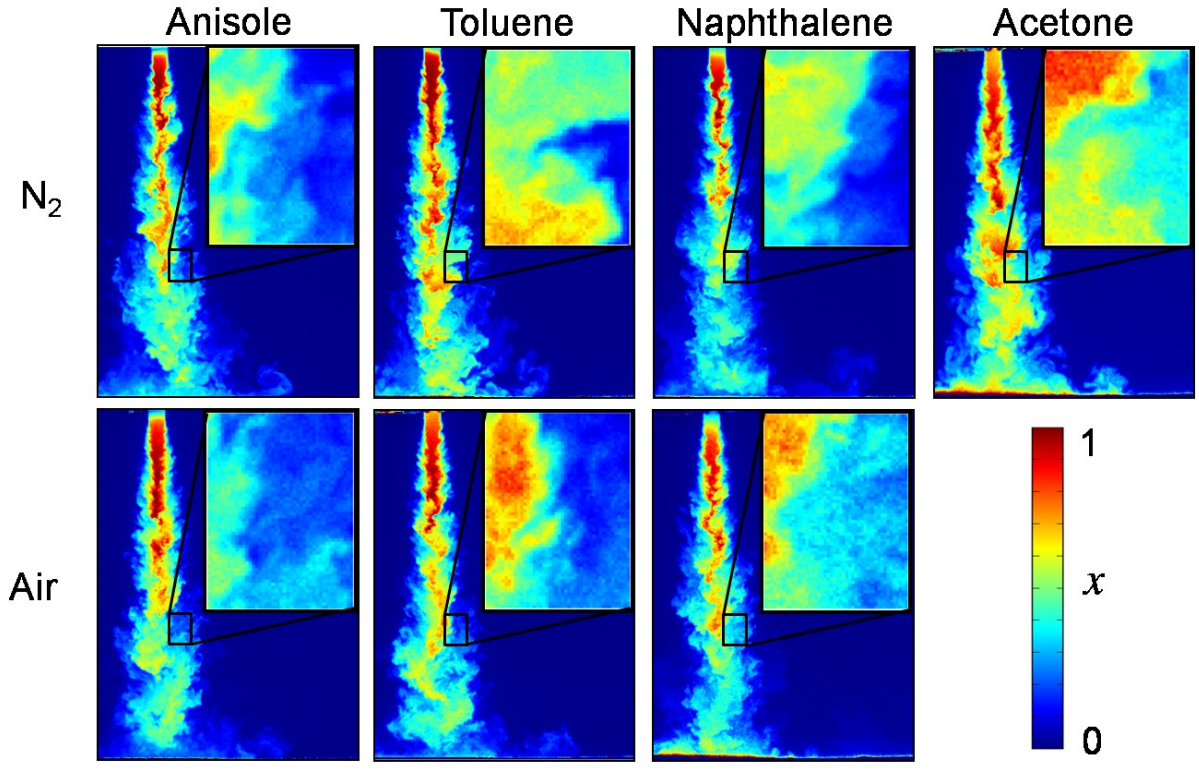

Figure 59: Instantaneous mixture fraction x from measurements with the four tracers in N_2 and air (acetone only in N_2) and tracer concentrations reached with a single-step bubbler system at room temperature. (50-shot averages for 58 ms after SOI).

The jet structure is consistently visualised by all tracers in both bath gases. Thus, all four tracers are in principle suitable for imaging gas mixing processes at temperatures significantly below the tracer's boiling points. When studying evaporating liquids, e.g.,

for in-cylinder fuel injection and evaporation, the influence of the vapour pressure may still be of interest.

The signal-to-noise level and hence the visual appearance of the images in Figure 59 is essentially the result of the corresponding LIF-signal level. Figure 60 and Table 8, respectively, compare the experimentally achieved LIF signal with the "theoretically" expected one for the same tracer number density. The experimental signal is determined as a spatial average over the imaged domain for more than 50 individual images captured at the same image timing (58 ms after SOI). This spatially-averaged ensemble mean was then corrected for image-intensifier gain and laser-pulse energy.

The theoretically expected signal was calculated based on the measured rates of evaporation and carrier-gas flow in the bubbler (cf., Table 9), multiplied with the fluorescence quantum yield ϕ([80, 93] and measurements in this thesis), the absorption cross-section σ([47, 71, 79, 90]), and the quantum efficiency of detection η (cf., Figure 57). The latter was determined by integrating the fluorescence spectrum weighted by the detection quantum efficiency at each wavelength. In other words, the calculation modelled the chain of fluorescence excitation and detection: tracer concentration, multiplied by probabilities of laser absorption, fluorescence emission, and photon detection. As the experimental setup is the same for all experiments, the (geometric) collection efficiency Ω was therefore not explicitly taken into account.

Figure 61 and Table 8, respectively, compare the measured total signal with the signal per molecule, i.e., the total signal divided by the experimentally achieved tracer number density (cf., Table 9). All experimental signal levels were normalised with respect to that of toluene in nitrogen; all theoretical signals to the theoretical one of that same tracer/bath-gas combination.

Table 8: Comparison of calculated and measured (relative) total signal (cf., Figure 60) together with the measured and calculated relative signal per molecule (cf., Figure 61) of the investigated tracers normalised to toluene in N_2. For acetone in air similar values are expected as in nitrogen.

	Calc. signal per volume		Measured signal per volume		Signal per molecule (meas.)		Signal per molecule (calc.)	
	N_2	Air	N_2	Air	N_2	Air	N_2	Air
Toluene	1	0.0143	1	0.0262	1	0.0262	1	0.0143
Anisole	6.7389	0.2042	1.6405	0.1781	11.51	0.952	32.73	0.9917
Naphth.	1.1869	0.0091	0.6617	0.0010	474.6	4.897	49.64	0.3818
Acetone	0.0041	---	0.0319	---	0.002	---	0.0002	---

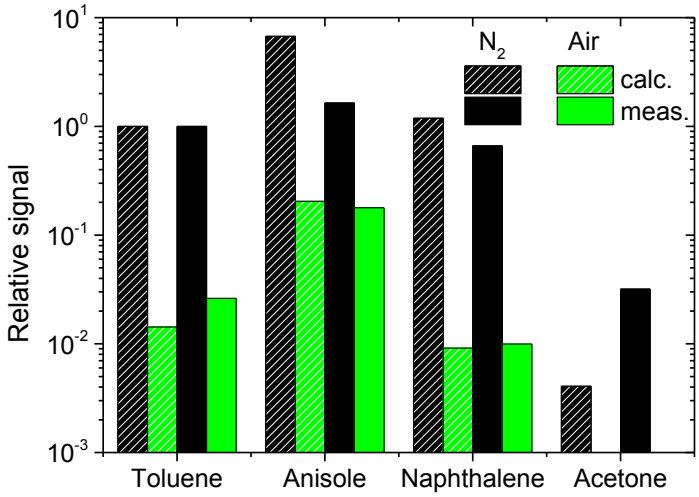

Figure 60: Comparison between measured and calculated signals per volume in N_2 and air (acetone only in N_2) relative to those of toluene in N_2. Note, the comparison is based on intensities obtained with a bubbler system, thus with strongly varying tracer number densities for the different tracers (cf., Table 9). Numerical values can be found in Table 8.

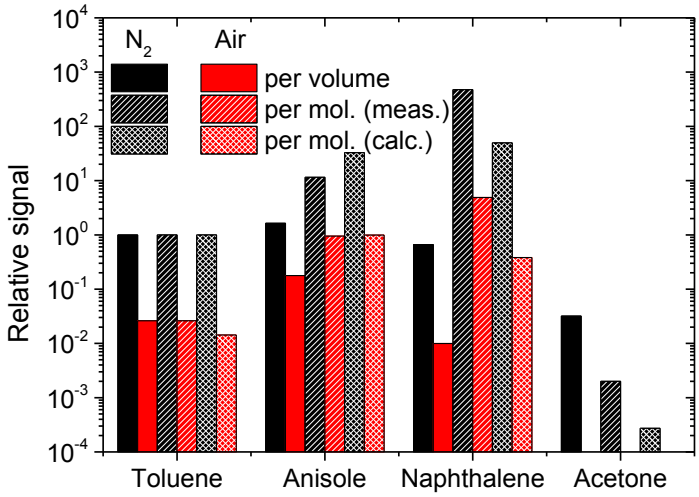

Figure 61: Comparison between the measured signal per volume together with the measured and calculated signal per molecule which is the total signal divided by the number density of molecules gained from Table 9. Numerical values can be found in Table 8.

When using a bubbler system people often assume that the resulting gas flow is saturated with the tracer at its respective vapour pressure. For the present experiment this assumption was checked by measuring the weight loss of the bubbler for a fixed operation time with a known carrier gas flow and the resulting tracer number densities were calculated based on the ideal gas law. The results presented in Table 9, however, show

strong deviation from saturation. Experimentally gained tracer number densities are about a factor of three below equilibrium. It must be emphasised that with an improved bubbler geometry or a multi-stage bubbler this discrepancy can be reduced. Note that in the case of the solution of naphthalene in dodecane the behaviour of the two-component system was not considered and equilibrium values were calculated based on pure naphthalene. The validity of this assumption must be checked in future experiments.

Table 9: Tracer number densities in the jet calculated by the ideal gas law using the assumption that the bath gas is saturated with the tracer at its respective vapour pressure (equilibrium) compared to the values determined from the measured evaporation rate of the respective tracer species. For naphthalene, values for pure naphthalene are used to determine the equilibrium value regardless of potential effects of the solvent dodecane.

	Number density / 10^{21} m^{-3}	
	Equilibrium	Experiment
Toluene	712	275
Anisole	88.1	46.7
Naphthalene	0.98	0.5
Acetone	6020	3440

Figure 60 shows that theoretically calculated and experimentally measured signal levels agree well in the case of air as bath and carrier gas, but less so in nitrogen. In the case of the aromatic tracers, quenching by oxygen from air contamination of the nitrogen in the vessel may contribute to the disagreement. Additionally, the theoretically calculated values are based on a chain of literature values, each with its own measurement uncertainty, which also may explain the discrepancies.

Another contribution to the disagreement may be the uncertainty in measuring the tracer evaporation rate, in particular in case of naphthalene and anisole, for which the weight-based evaporation measurement lasted several days before a sufficient quantity had been transported from the bubbler by the carrier-gas stream.

For acetone, phosphorescence is detected together with fluorescence, but the short intensifier gate (50 ns) should discriminate effectively against phosphorescence, which has a lifetime of ~200 µs. In fact, it may be concluded from Figure 60 and Figure 61 that predicting even the relative signal a priori is not simple highlighting the importance of comparative measurements.

The results are in good agreement with the qualitative results of Hirasawa *et al.* [19]. When comparing the results of this thesis to the results of Rossow [31], some discrepancies seem to occur, especially when comparing toluene and acetone. Besides the remarks

in the paragraphs above, one should keep in mind the differences in temperature and the fact that in the present case some parts of the toluene spectrum are cut off due to the straylight filter. This, however, represents the practical case rather than the comparison based on an integration of the entire spectra.

Based on actual quantity delivered into the jet's gas by the bubbler (cf., Table 9), anisole yields the best signal in both nitrogen and air. It is also remarkable how sensitive fluorescence of naphthalene in nitrogen is. Despite a concentration of only about 20 ppm in the jet gas, reasonable single-shot images could be obtained. With both anisole and naphthalene, the low necessary concentration can be advantageous in cases where high tracer concentrations may disturb thermodynamic or chemical properties of the fluid of interest.

The results from Figure 59, Figure 60, and Table 8 show that anisole provides the highest signal intensities in both N_2 and air as bath gas. When regarding the dependence of the fluorescence quantum yield on temperature and pressure this effect should increase at elevated temperatures (cf., section 5.1). Thus, the "new" tracer species anisole is considered to be an attractive candidate for the visualisation of gas flow mixing and – when extrapolation to this environmental conditions – also in, e.g., internal combustion engines. This finding again confirms the requirement of an extensive tracer screening before fixing on a specific tracer without a well-founded reason.

6. Conclusions and outlook

In the last decade, quantitative measurements with laser-induced fluorescence (LIF) of organic tracers have become possible and popular. An increasing amount of studies under well-defined environmental conditions provide information about fluorescence quantum yields that then allow to interpret signal intensities measured in practical applications. For ketones the database is large and sufficient for many applications. For aromatics, however, there are still lots of conditions of interest which have not been investigated yet. The fluorescence quantum yield is proportional to the fluorescence lifetime. Thus, measurements of the fluorescence lifetime provide information about the (relative) quantum yield independent on the tracer concentration.

In this work, fluorescence lifetimes and spectra of several organic tracers have been investigated after 266 nm excitation with a ps-Nd:YAG laser and detection with a streak camera system coupled to a spectrograph. Toluene has been studied in the 296–1200 K temperature range, in the 1–10 bar pressure range, and for varying bath gases of N_2, air, and CO_2. The fluorescence lifetime decreases exponentially in both N_2 and CO_2 with temperature from 46 ns at 296 K down to 0.05 ns at 1000 K. In contrast to the often used assumption that the fluorescence quantum yield of toluene is pressure-independent, it could be observed that total pressure of N_2 or CO_2 significantly decreases the fluorescence lifetime by up to 60%. This is in accord with recent unpublished work by Rossow [31]. As expected and concordant with literature, O_2 has a strong quenching influence on toluene fluorescence, e.g., the lifetime decreases from 46 ns without O_2 to 0.63 ns in air at 296 K with this effect diminishing with increasing temperature. The existing phenomenological fluorescence model of Koban *et al.* [29] was applied to the data. For 1 bar total pressure and for all bath gases good agreement was found. At higher pressures, significant deviations occurred. For N_2 and CO_2 as bath gases the model was improved to also represent this case.

Due to its higher boiling point and thus lower vapour pressure, naphthalene was investigated in the 373–1230 K temperature range, in the 1–10 bar pressure range, and for varying bath gases of N_2, air, and CO_2. The temperature dependence of the fluorescence lifetime in both N_2 and CO_2 is less pronounced than for toluene. Fluorescence lifetimes decrease from 104 ns at 373 K to 0.28 ns at 1123 K. In contrast to toluene increasing total pressure leads to an increase of the fluorescence lifetime by about 20%. The quenching efficiency of O_2 towards naphthalene is stronger (e.g., fluorescence lifetimes are reduced from 104 ns without O_2 to 1 ns in air at 373 K), but less temperature sensitive. For naphthalene phenomenological model functions were derived from the fluorescence lifetimes. Good agreement was found except in air at elevated pressures.

As a new tracer species, anisole was investigated in the 296–1000 K temperature range, in the 1–10 bar pressure range, and for N_2 and N_2/O_2 mixtures as bath gas. Spectral red-

shifts with increasing temperature and O_2 partial pressure were observed. In N_2 the fluorescence lifetime decreases from 13.3 ns at 296 K to 0.05 ns at 977 K. Increasing total pressure leads to a shorter fluorescence lifetime, but less pronounced as for toluene. The O_2 quenching efficiency has the same order of magnitude compared to toluene with a temperature sensitivity comparable to that of naphthalene. Similar phenomenological model functions as for naphthalene were derived and good agreement was found with experimental data. Deeper investigations of O_2 quenching at elevated pressures and the influence of different bath gases like CO_2 on the fluorescence of anisole must still be done. The development of a real photophysical model for anisole is a major task for the future based on the data provided in this thesis.

The ketone tracer species acetone and 3-pentanone were investigated in the 296–1000 K temperature range, at 1 bar total pressure, and for N_2 (both species), CO_2, and air (only 3-pentanone) as bath gas. The fluorescence lifetime decreases with increasing temperature, but the effect is less pronounced as for the aromatics. Within measurement uncertainty no differences between the fluorescence lifetimes in N_2, air, and CO_2 as bath gas could be observed. Existing fluorescence models were successfully applied to the data.

Due to the high achievable temperatures in the measurement cell, investigations concerning tracer pyrolysis were performed. When investigating ketones pyrolysis products begin to occur at around 1000 K. Two different fluorescing species could be observed: At temperatures between 1000 and 1200 K a product of decomposition processes is observed that is tentatively identified as ketene while at higher temperatures a second species occurs which could not yet be identified.

The aromatics toluene and naphthalene show visible pyrolysis species at temperatures above 1200 K. In both cases new fluorescence features occurred. These may result from benzyl or phenyl radicals in the case of toluene or from the naphthyl radical in the case of naphthalene, respectively. The long residence time inside the hot zone of the cell, however, could prevent the detection of radicals, so the measured fluorescence features may also belong to secondary reaction products. Anisole pyrolysis starts at temperatures of around 950 K, but no fluorescing pyrolysis species were detected. Future work is required to identify the fluorescing species formed through pyrolysis and secondary reactions. Diagnostics strategies using pyrolysis species of both aromatics and ketones have not been developed yet, the results of this thesis, however, suggest that this could be a promising option in the future.

As an application experiment, toluene, naphthalene, anisole, and acetone were compared in a gas jet with varying bath gases of N_2 and air. All tracers showed strong signal making them attractive as tracers for gas mixing diagnostics. Especially anisole proved to be very suitable because it showed the strongest total signal intensities in both N_2 and air as bath gas, about a factor of 50 stronger than toluene. The relative intensities are mostly in the expected order of magnitude when regarding the respective absorption cross-sections, fluorescence quantum yields, and O_2 quenching efficiencies. The meas-

urements presented here were carried out at room temperature. Measurements at elevated temperatures (and pressures) must be performed to fully characterise the applicability of the tracers.

This thesis delivers a large amount of reference data for quantitative diagnostics with aromatic tracers under engine-related conditions. Anisole is introduced as a new tracer species with improved diagnostics potential compared to toluene. This underlines the importance of a tracer screening to find the most suitable tracer for a specific application. Although phenomenological model functions are presented to predict signal intensities, it will be part of future work to build “real” photo-physical models, not only for a more precise prediction of signal intensities, but also for the deeper understanding of the underlying photophysical processes. The thermal stability of typical tracer molecules was investigated and new fluorescing species detected; it will be part of future work to clearly identify these species and to check if new diagnostics strategies based on these species open up.

References

1. R.K. Hanson, *Application of quantitative laser sensors to kinetics, propulsion and practical energy systems.* Proc. Combust. Inst. **33,** 1-40 (2011).

2. S. Roy, J. R. Gord, A. P. Patnaik, *Recent advances in coherent anti-Stokes Raman scattering spectroscopy: Fundamental developments and applications in reacting flows.* Prog. Energy Combust. Sci. **36,** 280-306 (2010).

3. A.C. Eckbreth, *Laser diagnostics for combustion temperature and species. - 2. ed. [compl. rev. and updated]*. 2nd ed. 1996, Amsterdam: Gordon & Breach.

4. J.B. Jeffries, K. Kohse-Höinghaus, ed. *Applied combustion diagnostics*. 2002, Taylor and Francis: New York.

5. R.K. Hanson, *Planar Laser-Induced Fluorescence Imaging.* J. Quant. Spectrosc. Radiat. Transfer. **40,** 343-362 (1988).

6. R.K. Hanson, J. M. Seitzman, P. H. Paul, *Planar Laser-Fluorescence Imaging of Combustion Gases.* Appl. Phys. B. **50,** 441-454 (1990).

7. C. Schulz, V. Sick, *Tracer-LIF diagnostics: quantitative measurement of fuel concentration, temperature and fuel/air ratio in practical combustion systems.* Progr. Energy Combust. Sci. **31,** 75-121 (2005).

8. W. Koban, *Photophysical characterization of toluene and 3-pentanone for quantitative imaging of fuel/air ratio and temperature in combustion systems*, in *dissertation thesis*. 2005: Ruperto-Carola University of Heidelberg, Germany.

9. J. Scholz, T. Wiersbinski, V. Beushausen, *Planar Fuel-Air-Ratio-LIF with Gasoline for Dynamic Mixture-Formation Investigations.* SAE technical paper series, 2007-01-0645 (2007).

10. J.V. Pastor, J. J. López, J. E. Juliá, J. V., Benajes, *Planar Laser-Induced Fluorescence fuel concentration measurements in isothermal Diesel sprays.* Opt. Exp. **10,** 309-323 (2002).

11. B. Williams, P. Ewart, X. Wang, R. Stone, H. Ma, H. Walmsley, R. Cracknell, R. Stevens, D. Richardson, H. Fu, S. Wallace, *Quantitative planar laser-induced fluorescence imaging of multi-component fuel/air mixing in a firing gasoline-direct-injection engine: Effects of residual exhaust gas on quantitative PLIF.* Combust. Flame. **157,** 1866-1878 (2010).

12. F. Rotter, J. Scholz, J. Grimsel, H. Wackerbarth, V. Beushausen, *Laser-induced fluorescence temperature determination in fuel-air mixtures without additional fluorescence tracers*. Appl. Phys. B. **101,** 909-913 (2010).

13. F. Ossler, T. Metz, M. Aldén, *Picosecond laser-induced fluorescence from gas-phase polycyclic aromatic hydrocarbons at elevated temperatures. I. Cell measurements.* Appl. Phys. B. **72,** 465-478 (2001).

14. F. Ossler, T. Metz, M. Aldén, *Picosecond laser-induced fluorescence from gas-phase polycyclic aromatic hydrocarbons at elevated temperatures. II. Flame-seeding measurements.* Appl. Phys. B. **72,** 479-489 (2001).

15. B.H. Cheung, R. K. Hanson, *CW laser-induced fluorescence of toluene for time-resolved imaging of gaseous flows.* Appl. Phys. B. **98,** 581-591 (2010).

16. J.E. Dec, W. Hwang, *Characterizing the development of thermal stratification in an HCCI engine using planar-imaging thermometry.* SAE technical paper series, 2009-01-0650 (2009).

17. R. Devillers, G. Bruneaux, C. Schulz, *Investigation of toluene LIF at high pressure and high temperature in an optical engine.* Appl. Phys. B. **96,** 735-739 (2009).

18. C. Gessenhardt, F. Zimmermann, C. Schulz, R. Reichle, C. Pruss, W. Osten, *Hybrid endoscopes for laser-based imaging diagnostics in IC engines.* SAE technical paper series, 2009-01-0655 (2009).

19. T. Hirasawa, T. Kaneba, Y. Kamata, K. Muraoka, Y. Nakamura, *Temperature Dependence of Intensities of Laser-Induced Fluorescences of Ethylbenzene and Naphthalene Seeded in Gas Flow at Atmospheric Pressure: Implications for Quantitative Visualization of Gas Temperature.* J. Visualization. **10,** 197-206 (2007).

20. S.A. Kaiser, M. B. Long, *Quantitative planar laser-induced fluorescence of naphthalenes as fuel tracers.* Proc. Combust. Inst. **30,** 1555-1563 (2005).

21. W. Koban, J. D. Koch, V. Sick, N. Wermuth, R. K. Hanson, C. Schulz, *Predicting LIF signal strength for toluene and 3-pentanone under engine-related temperature and pressure conditions.* Proc. Combust. Inst. **30,** 1545-1553 (2005).

22. M. Luong, R. Zhang, C. Schulz, V. Sick, *Toluene laser-induced fluorescence for in-cylinder temperature imaging in internal combustion engines.* Appl. Phys. B. **91,** 669-675 (2008).

23. M. Orain, F. Grisch, E. Joudanneau, B. Rossow, C. Guin, B. Trétout, *Simultaneous measurements of equivalence ratio and flame structure in multipoint injectors using PLIF.* C. R. Mecanique. **337,** 373-384 (2009).

24. C. Strozzi, J. Sotton, A. Mura, M. Bellenue, *Characterization of a two-dimensional temperature field within a rapid compression machine using a toluene planar laser-induced fluorescence imaging technique.* Meas. Sci. Technol. **20,** 125403 (2009).

25. C.A. Idicheria, L. M. Pickett, *Quantitative Mixing Measurements in a Vaporizing Diesel Spray by Rayleigh Imaging.* SAE technical paper series, 2007-01-0647 (2007).

26. C. Espey, J. E. Dec, T. A. Litzinger, D. A. Santavicca, *Planar Laser Rayleigh Scattering for Quantitative Vapor-Fuel Imaging in a Diesel Jet.* Combust. Flame. **109,** 65-86 (1997).

27. J.E. Dec, W. Hwang, M. Sjöberg, *An Investigation of Thermal Stratification in HCCI Engines using Chemiluminescence Imaging.* SAE technical paper series, 2006-01-1518 (2006).

28. M.C. Thurber, F. Grisch, B. J. Kirby, M. Votsmeier, R. K. Hanson, *Measurements and modeling of acetone laser-induced fluorescence with implications for temperature-imaging diagnostics.* Appl. Opt. **37,** 4963-4978 (1998).

29. W. Koban, J. D. Koch, R. K. Hanson, C. Schulz, *Oxygen quenching of toluene fluorescence at elevated temperatures.* Appl. Phys. B. **80,** 777-784 (2005).

30. J.D. Koch, *Fuel Tracer Photophysics for Quantitative Planar Laser-Induced Fluorescence*, in *dissertation thesis*. 2005: Stanford University, California, USA.

31. B. Rossow, *Photophysical processes of organic fluorescent molecules and kerosene - application to combustion engines*, in *dissertation thesis*. 2011, Institut des Sciences Moléculaires d'Orsay, Université Paris-Sud 11: Paris.

32. J.E. Dec, J. O. Keller, *High speed thermometry using two-line atomic fluorescence.* Proc. Combust. Inst. **21,** 1737-1745 (1986).

33. C.F. Kaminski, J. Engström, M. Aldén, *Quasi-instantaneous two-dimensional temperature measurements in a spark ignition engine using 2-line atomic fluorescence.* Proc. Combust. Inst. **27,** 85-93 (1998).

34. G.P. Smith, C. Park, J. Schneiderman, J. Luque, *C_2 Swan band laser-induced fluorescence and chemiluminescence in low-pressure hydrocarbon flames.* Combust. Flame. **141,** 66-77 (2005).

35. M. Tanahashi, S. Taka, M. Shimura, T. Miyauchi, *CH double-pulsed PLIF measurement in turbulent premixed flame.* Exp. Fluids. **45,** 323-332 (2008).

36. M. Tanahashi, S. Murakami, G.-M. Choi, Y. Fukuchi, T. Miyauchi, *Simultaneous CH-OH PLIF and stereoscopic PIV measurements of turbulent premixed flames.* Proc. Combust. Inst. **30,** 1665-1672 (2005).

37. J.T. Kashdan, J.-F. Papagni, *LIF Imaging of Auto-ignition and Combustion in a Direct Injection Diesel-fuelled HCCI Engine.* SAE technical paper series, 2005-01-3739 (2005).

38. W.G. Bessler, C. Schulz, T. Lee, J. B. Jeffries, R. K. Hanson, *Strategies for laser-induced fluorescence detection of nitric oxide in high-pressure flames: III. Comparison of A-X strategies.* Appl. Opt. **42,** 4922-4936 (2003).

39. B.K. McMillin, J. L. Palmer, R. K. Hanson, *Temporally resolved, two-line fluorescence imaging of NO temperature in a transverse jet in a supersonic cross flow.* Appl. Opt. **32,** 7532-7545 (1993).

40. W.G. Bessler, C. Schulz, *Quantitative multi-line NO-LIF temperature imaging.* Appl. Phys. B. **78,** 519-533 (2004).

41. K. Greenough, A. Duncan, *The fluorescence of sulfur dioxide.* J. Am. Chem. Soc. **83,** 555-560 (1961).

42. S.J. Strickler, D. Howell, *Luminescence and radiation transitions in sulfur dioxide gas.* J. Chem. Phys. **49,** 1947-1951 (1968).

43. V. Sick, *Exhaust-gas imaging via planar laser-induced fluorescence of sulfur dioxide.* Appl. Phys. B. **74,** 461-463 (2002).

44. B. Hiller, R. K. Hanson, *Properties of the iodine molecule relevant to laser-induced fluorescence experiment in gaseous flows.* Exp. Fluids. **10,** 1-11 (1990).

45. J. Savard, *Comparative spectrum analysis of o-, m- and p-isomerides of certain benzene derivatives.* Ann. Chim. **10,** 287-350 (1929).

46. A.M. Bass, *Fluorescence Studies of Some Simple Benzene Derivatives in the Near Ultraviolet. II. Toluene and Benzonitrile.* J. Chem. Phys. **18,** 1403-1410 (1950).

47. W. Koban, J. D. Koch, R. K. Hanson, C. Schulz, *Absorption and fluorescence of toluene vapor at elevated temperatures.* Phys. Chem. Chem. Phys. **6,** 2940-2945 (2004).

48. C.S. Burton, W. A. Noyes, *Electronic Energy Relaxation in Toluene Vapor.* J. Chem. Phys. **49,** 1705-1714 (1968).

49. B.H. Cheung, *Tracer-based planar laser-induced fluorescence diagnostics: Quantitative photophysics and time-resolved imaging*, in *dissertation thesis*. 2011, Stanford University: California, USA.

50. J. Yoo, D. Mitchell, D. F. Davidson, R. K. Hanson, *Planar laser-induced fluorescence imaging in shock tube flows.* Exp. Fluids. **49,** 751-759 (2010).

51. J. Reboux, D. Puechberty, F. Dionnet, *A New Approach of Planar Laser Induced Fluorescence Applied to Fuel/Air Ratio Measurement in the Compression Stroke of an Optical S.I. Engine.* SAE technical paper series, 941988 (1994).

52. W. Koban, C. Schulz, *Toluene laser-induced fluorescence (LIF) under engine-related pressures, temperatures and oxygen mole fractions.* SAE technical paper series, 2005-01-2091 (2005).

53. W. Koban, J. D. Koch, R. K. Hanson, C. Schulz, *Toluene LIF at elevated temperatures: implications for fuel/air ratio measurements.* Appl. Phys. B. **80,** 147-150 (2005).

54. K. Mohri, M. Luong, G. Vanhove, T. Dreier, C. Schulz, *Imaging of the oxygen distribution in an isothermal turbulent free jet using two-color toluene LIF imaging.* Appl. Phys. B. **103,** 707-715 (2011).

55. F.P. Zimmermann, W. Koban, C. M. Roth, D.-P. Herten, C. Schulz, *Fluorescence lifetime of gas-phase toluene at elevated temperatures.* Chem. Phys. Lett. **426,** 248-251 (2006).

56. G.M. Breuer, E. K.C. Lee, *Fluorescence Decay Times and non-Radiative Decay Rates of the First Excited Singlet States of Methylated and Fluorinated Benzenes.* Chem. Phys. Lett. **14,** 404-406 (1972).

57. C.G. Hickman, J. R. Gascooke, W. D. Lawrance, *The S_1–$S_0(^1B_2$–$^1A_1)$ transition of jet-cooled toluene: Excitation and dispersed fluorescence spectra, fluorescence*

lifetimes, and intramolecular vibrational energy redistribution. J. Chem. Phys. **104,** 4887-4901 (1996).

58. M. Jacon, C. Lardeux, R. Lopez-Delgado, A. Tramer, *On the "Third Decay Channel" and Vibrational Redistribution Problems in Benzene Derivatives.* Chem. Phys. **24,** 145-157 (1977).

59. E.H. Kincaid, V. Worah, M. D. Schuh, *Collision-induced state-to-state flow of vibrational energy in S_1 toluene.* J. Chem. Phys. **94,** 4842-4851 (1991).

60. A. Ehn, B. Kaldvee, J. Bood, M. Aldén, *Development of a temporal filtering technique for suppression of interferences in applied laser-induced fluorescence diagnostics.* Appl. Opt. **48,** 2373-2387 (2009).

61. E. Friesen, C. Gessenhardt, S. Kaiser, T. Dreier, C. Schulz. *In-cylinder temperature measurements via fiber-based toluene-LIF time-correlated single-photon counting*. in *LACSEA2012*. 2012. San Diego, CA, USA.

62. E. Friesen, C. Gessenhardt, S. A. Kaiser, T. Dreier, C. Schulz, *In-cylinder temperature measurements via time-correlated single-photon counting of toluene-LIF through a fiber-based sensor.* Opt. Lett., (submitted).

63. M. Orain, P. Baranger, B. Rossow, F. Grisch, *Fluorescence spectroscopy of 1,2,4-trimethylbenzene at high temperatures and pressures: application to temperature measurements.* Appl. Phys. B. **100,** 945-952 (2010).

64. P. Baranger, M. Orain, F. Grisch, *Fluorescence Spectroscopy of Kerosene Vapour: Application to Gas Turbines.* AIAA paper, 2005-828 (2005).

65. Y. He, E. Pollak, *Theory of fluorescence decay of naphthalene: Was photoinduced cooling observed experimentally?* J. Chem. Phys. **116,** 6088-6101 (2002).

66. J.C. Hsieh, C.-S. Huang, E. C. Lim, *Radiationless singlet deactivation in isolated large molecules. I Naphthalene, naphthol, and naphthylamine.* J. Chem. Phys. **60,** 4345-4353 (1974).

67. A. Reimann, *Über die Photolumineszenz des Benzols und einiger Derivate in verschiedenen Aggregat- und Lösungszuständen.* Ann. Phys. **80,** 43-70 (1926).

68. R.E. Smalley, *Dynamics of Electronically Excited States.* Annu. Rev. Phys. Chem. **34,** 129-153 (1983).

69. M. Stockburger, H. Gattermann, W. Klusmann, *Spectroscopic studies on naphthalene in the vapor phase. II. Fluorescence quantum yields from single vibronic levels in the first excited singlet state - behavior of higher excited singlet states.* J. Chem. Phys. **63,** 4529-4540 (1975).

70. E. Wiedemann, G. C. Schmidt, *Ueber Lichtemission organischer Substanzen im gasförmigen, flüssigen und festen Zustand.* Ann. Phys. **56,** 18-26 (1895).

71. M. Orain, P. Baranger, B. Rossow, F. Grisch, *Fluorescence spectroscopy of naphthalene at high temperatures and pressures: implications for fuel-concentration measurements.* Appl. Phys. B. **102,** 163-172 (2011).

72. J. Ferguson, L. W. Reeves, W.G. Schneider, *Vapor absorption spectra and oscillator strengths of naphthalene, anthracene, and pyrene.* Can. J. of Chemistry. **35,** 1117-1136 (1957).

73. T. Ni, L. A. Melton, *Two-Dimensional Gas-Phase Temperature Measurements Using Fluorescence Lifetime Imaging.* Appl. Spectr. **50,** 1112-1116 (1996).

74. M. Kühni, C. Morin, P. Guibert, *Fluoranthene laser-induced fluorescence at elevated temperatures and pressures: implications for temperature-imaging diagnostics.* Appl. Phys. B. **102,** 659-671 (2011).

75. T.Q. Ni, L. A. Melton, *Fuel Equivalence Ratio Imaging for Methane Jets.* Appl. Spectr. **47,** 773-781 (1993).

76. K.-M. Bark, R. K. Forcé, *Fluorescence properties of fluoranthene as a function of temperature and environment.* Spectrochim. Acta A. **49,** 1605-1611 (1993).

77. T. Ni, L. A. Melton, *Fluorescence Lifetime Imaging: An Approach for Fuel Equivalence Ratio Imaging.* Appl. Spectr. **45,** 938-943 (1991).

78. J.K. Marsh, *Studies in Fluorescence Spectra. Part II. Phenol and Phenolic Ether Vapours.* J. Chem. Soc. Trans. **125,** 418-423 (1924).

79. T. Etzkorn, B. Klotz, S. Sörensen, I. V. Patroescu, I. Barnes, K. H. Becker, U. Platt, *Gas-phase absorption cross sections of 24 monocyclic aromatic hydrocarbons in UV and IR spectral range.* Atmos. Environ. **33,** 525-540 (1999).

80. N. Nijegorodov, R. Mabbs, D. P. Winkoun, *Influence of weak and strong donor groups on the fluorescence parameters and the intersystem crossing rate constant.* Spectrochim. Acta A. **59,** 595-606 (2003).

81. G.H. Damon, F. Daniels, *The Photolysis of Gaseous Acetone and the Influence of Water.* J. Am. Chem. Soc. **55,** 2363-2375 (1933).

82. M.S. Matheson, J. W. Zabor, *Fluorescence of Carbonyl Compounds in the Gas Phase.* J. Chem. Phys. **7,** 536-538 (1939).

83. A. Lozano, B. Yip, R. K. Hanson, *Acetone: a tracer for concentration measurements in gaseous flows by planar laser-induced fluorescence.* Exp. Fluids. **13,** 369-376 (1992).

84. H. Neij, B. Johansson, M. Aldén, *Development and Demonstration of 2D-LIF for Studies of Mixture Preparation in SI Engines.* Combust. Flame. **99,** 449-457 (1994).

85. B.H. Cheung, R. K. Hanson, *3-pentanone fluorescence yield measurements and modeling at elevated temperatures and pressures.* Appl. Phys. B. **106,** 755-768 (2012).

86. F. Grossmann, P. B. Monkhouse, M. Ridder, V. Sick, J. Wolfrum, *Temperature and pressure dependences of the laser-induced fluorescence of gas-phase acetone and 3-pentanone.* Appl. Phys. B. **62,** 249-253 (1996).

87. J.D. Koch, R. K. Hanson, *Temperature and excitation wavelength dependencies of 3-pentanone absorption and fluorescence for PLIF applications.* Appl. Phys. B. **76,** 319-324 (2003).

88. V. Modica, C. Morin, P. Guibert, *3-Pentanone LIF at elevated temperatures and pressures: measurement and modeling.* Appl. Phys. B. **87,** 193-204 (2007).

89. M.C. Thurber, R. K. Hanson, *Pressure and composition dependence of acetone laser-induced fluorescence with excitation at 248, 266, and 308 nm.* Appl. Phys. B. **69,** 229-240 (1999).

90. J.D. Koch, J. Gronki, R. K. Hanson, *Measurements of near-UV absorption spectra of acetone and 3-pentanone at high temperatures.* J. Quant. Spectrosc. Radiat. Transfer. **109,** 2037-2044 (2008).

91. D.A. Rothamer, J. A. Snyder, R. K. Hanson, R. R. Steeper, *Optimization of a tracer-based PLIF diagnostic for simultaneous imaging of EGR and temperature in IC engines.* Appl. Phys. B. **99,** 371-384 (2010).

92. W.A. Noyes Jr., G. B. Porter, J. E. Jolley, *The primary photochemical process in simple ketones.* Chem. Rev. **56,** 49-94 (1955).

93. J.D. Koch, R. K. Hanson, W. Koban, C. Schulz, *Rayleigh-calibrated fluorescence quantum yield measurements of acetone and 3-pentanone.* Appl. Opt. **43,** 5901-5910 (2004).

94. H. Zuckermann, B. Schmitz, Y. Haas, *Acetone Photophysics in Seeded Supersonic Molecular Beams.* J. Phys. Chem. **93,** 4083-4091 (1989).

95. G.D. Greenblatt, S. Ruhman, Y. Haas, *Fluorescence decay kinetics of acetone vapour at low pressures.* Chem. Phys. Lett. **112,** 200-206 (1984).

96. R.F. Borkman, D. R. Kearns, *Electronic-Relaxation Processes in Acetone.* J. Chem. Phys. **44,** 945-949 (1966).

97. V. Khamaganov, R. Karunanandan, A. Rodriguez, J. N. Crowley, *Photolysis of $CH_3C(O)CH_3$ (248 nm, 266 nm), $CH_3C(O)C_2H_5$ (248 nm) and $CH_3C(O)Br$ (248 nm): pressure dependent quantum yields of CH_3 formation.* Phys. Chem. Chem. Phys. **9,** 4098-4113 (2007).

98. Y. Haas, *Photochemical α-cleavage of ketones: revisiting acetone.* Photochem. Photobiol. Sci. **3,** 6-16 (2004).

99. R.G.W. Norrish, H. G. Crone, O. D. Saltmarsh, *Primary photochemical reactions. Part V. The spectroscopy and photochemical decomposition of acetone.* J. Chem. Soc., 1456-1460 (1934).

100. S.W. North, D. A. Blank, J. D. Gezelter, C. A. Longfellow, Y. T. Lee, *Evidence for stepwise dissociation dynamics in acetone at 248 and 193 nm.* J. Chem. Phys. **102,** 4447-4460 (1995).

101. R.E. Hunt, W. A. Noyes Jr., *Photochemical Studies. XXXIX. A Further Study on the Fluorescence of Acetone.* J. Am. Chem. Soc. **70,** 467-476 (1948).

102. M.A. Blitz, D. E. Heard, M. J. Pilling, *Study of Acetone Photodissociation over the Wavelength Range 248-330 nm: Evidence of a Mechanism Involving Both the Singlet and Triplet Excited States.* J. Phys. Chem. A. **110,** 6742-6756 (2006).

103. A. Braeuer, F. Beyrau, A. Leipertz, *Laser-induced fluorescence of ketones at elevated temperatures for pressures up to 20 bars by using a 248 nm excitation laser wavelength: experiments and model improvements.* Appl. Opt. **45,** 4982-4989 (2006).

104. M. Loeffler, F. Beyrau, A. Leipertz, *Acetone laser-induced fluorescence behavior for the simultaneous quantification of temperature and residual gas distribution in fired spark-ignition engines.* Appl. Opt. **49,** 37-49 (2010).

105. M. Orain, B. Rossow, F. Grisch. *Spectroscopic studies of ketones and mono-aromatics: implication for equivalence ratio measurements in two-phase flows with multi-component fuels*. in *14th In. Symp. on Applications of Laser Techniques to Fluid Mechanics*. 2008. Lisbon, Portugal.

106. W.M. Nau, J. C. Scaiano, *Oxygen quenching of excited aliphatic ketones and diketones.* J. Phys. Chem. **100,** 11360-11367 (1996).

107. F. Ossler, M. Aldén, *Measurement of picosecond laser induced fluorescence from gas phase 3-pentanone and acetone: Implications to combustion diagnostics.* Appl. Phys. B. **64,** 493-502 (1997).

108. A.M. Halpern, W. R. Ware, *Excited Singlet State Radiative and Nonradiative Transition Probabilities for Acetone, Acetone-d_6, and Hexafluoroacetone in the Gas Phase, in Solution, and in the Neat Liquid.* J. Chem. Phys. **54,** 1271-1276 (1971).

109. H. Hu, M. M. Koochesfahani, *A novel method for instantaneous, quantitative measurement of molcular mixing in gaseous flows.* Exp. Fluids. **33,** 202-209 (2002).

110. P. Guibert, V. Modica, C. Morin, *Influence of pressure, temperature and gas phase composition on biacetyl laser-induced fluorescence.* Exp. Fluids. **40,** 245-256 (2006).

111. J.D. Smith, V. Sick, *Crank-angle resolved imaging of biacetyl laser-induced fluorescence in an optical internal combustion engine.* Appl. Phys. B. **81,** 579-584 (2005).

112. J.D. Smith, V. Sick, *Quantitative, dynamic fuel distribution measurements in combustion-related devices using laser-induced fluorescence imaging of biacetyl in iso-octane.* Proc. Combust. Inst. **31,** 747-755 (2007).

113. B. Peterson, D. L. Reuss, V. Sick, *High-speed imaging analysis of misfires in a spray-guided direct injection engine.* Proc. Combust. Inst. **33,** 3089-3096 (2011).

114. C. Schulz, J. Gronki, S. Andersson, *Multi-Species Laser-Based Imaging Measurements in a Diesel Spray.* SAE technical paper series, 2004-01-1917 (2004).

115. C.G. Freeman, M. J. McEwan, R. F. C. Claridge, L.- F. Phillips, *Fluorescence of aliphatic amines.* Chem. Phys. Lett. **8,** 77-78 (1971).

116. I. Düwel, W. Koban, F. P. Zimmermann, T. Dreier, C. Schulz, *Spectroscopic characterization of the fluorobenzene/DEMA tracer system for laser-induced exciplex fluorescence for the quantitative study of evaporating fuel sprays.* Appl. Phys. B. **97,** 909-918 (2009).

117. Ö. Andersson, H. Neij, J. Bood, B. Axelsson, M. Aldén, *Optical Characterization of Dimethyl Ether (DME) for Laser-based Combustion Diagnostics.* Combust. Sci. and Tech. **137,** 299-322 (1998).

118. V.M. Salazar, S. A. Kaiser, F. Helter, *Optimizing Precision and Accuracy of Quantitative PLIF of Acetone as a Tracer for Hydrogen Fuel.* SAE technical paper series, 2009-01-1534 (2009).

119. M. Luong, W. Koban, C. Schulz, *Novel strategies for imaging temperature distribution using Toluene LIF.* J. Phys.: Conf. Series. **45,** 155-161 (2006).

120. C. Hecht, A. Abdali, T. Dreier, C. Schulz, *Gas-temperature imaging in a microwave-plasma nanoparticle-synthesis reactor using multi-line NO-LIF thermometry.* Z. physik. Chem. **225,** 1225-1235 (2011).

121. H. Kronemayer, P. Ifeacho, C. Hecht, T. Dreier, H. Wiggers, C. Schulz, *Gas-temperature imaging in a low-pressure flame reactor for nano-particle synthesis with multi-line NO-LIF thermometry.* Appl. Phys. B. **88,** 373-377 (2007).

122. D.S. Baer, R. K. Hanson, M. E. Newfield, N. K. J. M. Gopaul, *Multiplexed diode-laser sensor system for simultaneous H_2O, O_2, and temperature measurements.* Opt. Lett. **19,** 1900-1902 (1994).

123. V. Ebert, J. Wolfrum, *Absorption spectroscopy*, in *Optical Measurement Techniques and Applications*, F. Mayringer, Editor. 1994: Berlin. p. 273-312.

124. M.G. Allen, *Diode laser absorption sensors for gas-dynamic and combustion flows.* Meas. Sci. Technol. **9,** 545-562 (1998).

125. F.-Y. Zhang, T. Fujiwara, K. Komurasaki, *Diode-laser tomography for arcjet plume reconstruction.* Appl. Opt. **40,** 957-964 (2001).

126. H. Yang, *Tunable diode-laser absorption-based sensors for the detection of water vapor concentration, film thickness and temperature*, in *dissertation thesis*. 2012, University of Duisburg-Essen: Duisburg, Germany.

127. T. Landenfeld, A. Kremer, E. P. Hassel, J. Janicka, T. Schäfer, J. Kazenwadel, C. Schulz, J. Wolfrum, *Laser-diagnostic and numerical study of strongly swirling natural gas flames.* Proc. Combust. Inst. **27,** 1023-1029 (1998).

128. J.N. Forkey, N. D. Finkelstein, W. R. Lempert, R. B. Miles, *Demonstration and Characterization of Filtered Rayleigh Scattering for Planar Velocity Measurements.* AIAA Journal. **34,** 442-448 (1996).

129. D. Greszik, H. Yang, T. Dreier, C. Schulz, *Measurement of water film thickness by laser-induced fluorescence and Raman imaging.* Appl. Phys. B. **102,** 123-132 (2011).

130. F. Fuest, R. S. Barlow, D. Geyer, F. Seffrin, A. Dreizler, *A hybrid method for data evaluation in 1-D Raman spectroscopy.* Proc. Combust. Inst. **33,** 815-822 (2011).

131. A.C. Eckbreth, *CARS Thermometry in Practical Combustors.* Combust. Flame. **39,** 133-147 (1980).

132. S. Hildenbrand, S. Staudacher, D. Brüggemann, F. Beyrau, M. C. Weikl, T. Seeger, A. Leipertz, *Numerical and experimental study of the vaporization cooling in gasoline direct injection sprays.* Proc. Combust. Inst. **31,** 3067-3073 (2007).

133. S.R. Engel, A. F. Koegler, Y. Gao, D. Kilian, M. Voigt, T. Seeger, W. Peukert, A. Leipertz, *Gas phase temperature measurements in the liquid and particle regime of a flame spray pyrolysis process using O_2-based pure rotational coherent anti-Stokes Raman scattering*. Appl. Opt. **51,** 6063-6075 (2012).

134. W. Koban, J. Schorr, C. Schulz, *Oxygen-distribution imaging with a novel two-tracer laser-induced fluorescence technique.* Appl. Phys. B. **74,** 111-114 (2002).

135. D. Frieden, V. Sick, J. Gronki, C. Schulz, *Quantitative oxygen imaging in an engine.* Appl. Phys. B. **75,** 137-141 (2002).

136. R. Reichle, C. Pruss, C. Gessenhardt, C. Schulz, W. Osten, *Diffractive/refractive (hybrid) UV-imaging system for minimally invasive metrology: design, performance, and application experiments.* Appl. Opt. **51,** 1982-1996 (2012).

137. G. Tea, *Development and exploitation of fluorescence tracer technique for simultaneous temperature, fuel and oxygen concentration measurements in IC engines*, in *dissertation thesis*. 2012, University of Duisburg-Essen: Duisburg, Germany.

138. A. Ehn, O. Johansson, A. Arvidsson, M. Aldén, J. Bood, *Single-laser shot fluorescence lifetime imaging on the nanosecond timescale using a dual image and modeling algorithm.* Opt. Exp. **20,** 3043-3056 (2012).

139. J.R. Lakowicz, *Principles of Fluorescence Spectroscopy*. 3rd ed. 2006, New York: Springer Science + Business Media, LLC.

140. P.W. Atkins, J. de Paula, *Physikalische Chemie*. 2006, Weinheim: Wiley-VCH.

141. J. Gilbert, A. Baggot, *Essentials of molecular photochemistry*. 1991, Oxford: Blackwell.

142. N.J. Turro, *Modern molecular photochemistry*. 1978, Menlo Park: Benjamin / Cummings.

143. J.B. Birks, *Photophysics of aromatic molecules*. 1970, London: Wiley-Interscience.

144. T. Förster, *Zwischenmolekulare Energiewanderung und Fluoreszenz.* Ann. Phys. **6,** 55-75 (1948).

145. D.L. Dexter, *A Theory of Sensitized Luminescence in Solids.* J. Chem. Phys. **21,** 836-850 (1953).

146. J.B. Birks, *Energy transfer is organic systems.* J. Phys. B. **3,** 417-424 (1970).

147. R.G. Brown, D. Phillips, *Quenching of the first excited singlet state of substituted benzenes by molecular oxygen.* Trans. Farad. Soc. II. **70,** 630-636 (1974).

148. K. Kikuchi, C. Sato, M. Watabe, H. Ikeda, Y. Takahashi, T. Miyashi, *New aspects on fluorescence quenching by molecular oxygen.* J. Am. Chem. Soc. **115,** 5180-5184 (1993).

149. O. Stern, M. Volmer, *Über die Abklingungszeit der Fluoreszenz.* Physik. Z. **20,** 183-188 (1919).

150. K.F. Freed, D. F. Heller, *Pressure dependence of electronic relaxation: A stochastic model.* J. Chem. Phys. **61,** 3942-3953 (1974).

151. D.J. Wilson, B. Noble, B. Lee, *Pressure Dependence of Fluorescence Spectra.* J. Chem. Phys. **34,** 1392-1396 (1961).

152. L.S. Yuen, J. E. Peters, R. P. Lucht, *Pressure dependence of laser-induced fluorescence from acetone.* Appl. Opt. **36,** 3271-3277 (1997).

153. D.A. Rothamer, *Developement and Application of Infrared and Tracer-Based Planar Laser-Induced Fluorescence Imaging Diagnostics*, in *dissertation thesis*. 2007, Stanford University, Department of Mechanical Engineering: Stanford, California, USA.

154. J.R. Barker, L. M. Yoder, K. D. King, *Vibrational Energy Transfer Modeling of Nonequilibrium Polyatomic Reaction Systems.* J. Phys. Chem. A. **105,** 796-809 (2001).

155. J. Troe, *Theory of thermal unimolecular reactions at low pressures. II. Strong collision rate constants. Applications.* J. Chem. Phys. **66,** 4758-4775 (1977).

156. A. Fateev, S. Clausen, *In situ Temperature Measurements by UV-Absorption Spectroscopy.* Int. J. Thermophys. **30,** 265-275 (2009).

157. D. Lüdtke, *Quantifizierung von NO-Molekülen unter Hochdruckbedingungen mittels rotationsaufgelöster laserinduzierter Fluoreszenz*, in *diploma thesis*. 1996, Universität Bielefeld, Lehrstuhl für Angewandte Laserphysik: Bielefeld, Germany.

158. L. Deng, *Numerical Investigation of the Gas Phase Transport and the Conjugate Heat Transfer inside a High Pressure Flow Cell*, in *master thesis*. 2010, Universität Duisburg-Essen, Chair of Mechanic and Robotic: Duisburg, Germany.

159. G. Kurutas, *Modellierung und Strömungssimulation einer Hochdruckmesszelle*, in *diploma thesis*. 2008, University of Duisburg-Essen: Duisburg, Germany.

160. Ekspla, *PL2143 Series Laser Manual*. 2006, Vilnius, Lithuania.

161. H. Photonics. 2011; Available from: http://sales.hamamatsu.com/assets/pdf/parts_C/e_C5680.pdf.

162. T.B. Settersten, A. Dreizler, R. L. Farrow, *Temperature- and species-dependent quenching of CO B probed by twophoton laser-induced fluorescence using a picosecond laser.* J. Chem. Phys. **117,** 3173-3179 (2002).

163. T.B. Settersten, B. D. Patterson, J. A. Gray, *Temperature- and species-dependent quenching of NO $A^2\,S^+$ (v'=0) probed by two-photon laser-induced fluorescence using a picosecond laser.* J. Chem. Phys. **124,** 234308 (2006).

164. H. Wadi, E. Pollak, *Theory of laser cooling of polyatomic molecules in an electronically excited state.* J. Chem. Phys. **110,** 11890-11905 (1999).

165. L.A. Barkova, V. V. Gruzinskii, M. N. Kaputerko, *Quenching and stabilization of the fluorescence of anthracene vapor by xenon.* J. Appl. Spectr. **47,** 786-789 (1987).

166. C.E. Otis, J. L. Knee, P. M. Johnson, *The identification of channel three in isolated benzene.* J. Chem. Phys. **78,** 2091-2092 (1983).

167. F. Ossler, T. Metz, M. Aldén, *Picosecond laser-induced fluorescence from gas-phase polycyclic aromatic hydrocarbons at elevated temperatures. I. Cell measurements.* Appl. Phys. B. **72,** 465 (2001).

168. G.S. Beddard, G. R. Fleming, O. L. J. Gijzeman, G. Porter, *Vibrational energy dependence of radiationless conversion in aromatic vapours.* Proc. R. Soc. Lond. A. **340,** 519-533 (1974).

169. S.F. Fischer, A. L. Stanford, E. C. Lim, *Excess energy dependence of radiationless transitions in naphthalene vapor: Competition between internal conversion and intersystem crossing.* J. Chem. Phys. **61,** 582-593 (1974).

170. A.M. Scheer, C. Mukarakate, D. J. Robichaud, G. B. Ellison, M. R. Nimlos, *Radical Chemistry in the Thermal Decomposition of Anisole and Deuterated Anisoles: An Investigation of Aromatic Growth.* J. Phys. Chem. A. **114,** 9043-9056 (2010).

171. M. Hesse, H. Meier, B. Zeeh, *Spektroskopische Methoden in der organsischen Chemie*. Vol. 7th edition. 2005, Stuttgart, Germany: Thieme.

172. B.H. Cheung, R. K. Hanson, *Determination of fluorescence and non-radiative de-excitation rates of excited 3-pentanone at low pressures.* Appl. Phys. B. **106,** 741-753 (2012).

173. K.-Y. Lam, W. Ren, Z. Hong, D. F. Davidson, R. K. Hanson, *Shock tube measurements of 3-pentanone pyrolysis and oxidation.* Combust. Flame. **159,** 3251-3263 (2012).

174. S. Pichon, G. Black, N. Chaumeix, M. Yahyaoui, J. M. Simmie, H. J. Curran, R. Donohue, *The combustion chemistry of a fuel tracer: Measured flame speeds and ignition delays and a detailed chemical kinetic model for the oxidation of acetone.* Combust. Flame. **156,** 494-504 (2009).

175. R.J. Kee, F.M. Rupley, J.A. Miller, M.E. Coltrin, J.F. Grcar, E. Meeks, H.K. Moffat, A.E. Lutz, G. Dixon-Lewis, M.D. Smooke, J. Warnatz, G.H. Evans, R.S. Larson, R.E. Mitchell, L.R. Petzold, W.C. Reynolds, M. Caracotsios, W.E. Stewart, P. Glarborg, C. Wang, O. Adigun, *CHEMKIN Collection, Release 3.6*. 2000, Reaction Design, Inc.: San Diego, CA.

176. R.G.W. Norrish, H. G. Crone, O. D. Saltmarsh, *Primary Photochemical Processes. Part III. The Absorption Spectrum and Photochemical Decomposition of Keten.* J. Chem. Soc., 1533-1539 (1933).

177. S. Linow, A. Dreizler, J. Janicka, E. P.Hassel, *Comparison of two-photon excitation schemes for CO detection in flames.* Appl. Phys. B. **71,** 689-696 (2000).

178. J.M. Seitzman, J. Haumann, R. K. Hanson, *Quantitative two-photon LIF imaging of carbon monoxide in combustion gases.* Appl. Opt. **26,** 2892-2899 (1987).

179. M. Mosburger, V. Sick, *Single laser detection of CO and OH via laser-induced fluorescence.* Appl. Phys. B. **99,** 1-6 (2010).

180. W.F. Chan, G. Cooper, C. E. Brion, *Absolute optical osciallator strengths for discrete and continuum photoabsorption of carbon monoxide (7-200 eV) and transition moments for the $X\ ^1S^+$ --> $A\ ^1P$ system.* Chem. Phys. **170,** 123-138 (1993).

181. S. Zabeti. personal communication.

182. A. Fahr, *Ultraviolet absorption spectrum and cross-sections of ethynyl (C_2H) radicals.* J. Mol. Spectrosc. **217,** 249-254 (2003).

183. J.C.G. Andrae, T. Brinck, G. T. Kalghatgi, *HCCI experiments with toluene reference fuels modeled by a semidetailed chemical kinetic model.* Combust. Flame. **155,** 696-712 (2008).

184. L. Zhang, C. Jianghuai, Z. Taichang, F. Qi, *Kinetic modeling study of toluene pyrolysis at low pressure.* Combust. Flame. **157,** 1686-1697 (2010).

185. T.J. Wallington, H. Egsgaard, O. J. Nielsen, J. Platz, J. Sehested, T. Stein, *UV-visible spectrum of the phenyl radical and kinetics of its reaction with NO in the gas phase.* Chem. Phys. Lett. **290,** 363-370 (1998).

186. F. Markert, P. Pagsberg, *UV spectra and kinetics of radicals produced in the gas phase reactions of Cl, F and OH with toluene.* Chem. Phys. Lett. **209,** 445-454 (1993).

187. T. Okamura, T. R. Charlton, B. A. Thrush, *Laser-induced fluorescence of benzyl radicals in the gas phase.* Chem. Phys. Lett. **88,** 369-371 (1982).

188. O.S.L. Bruinsma, P. J. J. Tromp, H. J. J. de Sauvage Nolting, J. A. Moulijn, *Gas phase pyrolysis of coal-related aromatic compounds in a coiled tube flow reactor 2. Heterocyclic compounds, their benzo and dibenzo derivatives.* Fuel. **67,** 334-340 (1988).

189. S.A. Kaiser, M. N. Thuong, M. Goschütz, I. Wlokas, A. Kempf, *Experiments and computation of a transient impinging turbulent jet*, in *34th International Symposium on Combustion*. 2012: Warsaw, Poland.

List of own publications

Peer-reviewed publications

1. S. Faust, T. Dreier, C. Schulz, *Temperature and bath gas composition dependence of effective fluorescence lifetimes of toluene excited at 266 nm*, Chem. Phys. **383**(1-3), 6-11 (2011).

2. S. Faust, G. Tea, T. Dreier, C. Schulz, *Temperature, pressure, and bath gas composition dependence of fluorescence spectra and fluorescence lifetimes of toluene and naphthalene*, Appl. Phys. B **110**, 81-93 (2013).

3. S. Faust, T. Dreier, C. Schulz, *Photo-physical properties of anisole: temperature, pressure, and bath gas composition dependence of fluorescence spectra and lifetimes*, Appl. Phys. B, in press.

Conference contributions

1. S. Faust, T. Dreier, C. Schulz, *Temperatur- und Puffergasabhängigkeit der effektiven Fluoreszenzlebensdauer von Toluol nach Anregung mit 266 nm*, 110. Bunsentagung, Berlin, Germany, 2011, poster

2. S. Faust, G. Tea, T. Dreier, C. Schulz, *Toluene and naphthalene effective fluorescence lifetimes as a function of environmental conditions: Implication for model development*, Gordon Conference on Laser Diagnostics in Combustion, Waterville Valley, USA, 2011, poster

3. G. Tea, S. Faust, G. Bruneaux, J. Kashdan, T. Dreier, C. Schulz, *Fluorescence tracer techniques for simultaneous temperature and equivalence ratio imaging in Diesel jets*, Gordon Conference on Laser Diagnostics in Combustion, Waterville Valley, USA, 2011, poster

4. S. Faust, T. Dreier, C. Schulz, *Effective fluorescence lifetimes of organic fuel tracers for combustion relevant environmental conditions*, 34th International Symposium on Combustion, Warsaw, Poland, 2012, poster

5. T. Benzler, S. Faust, T. Dreier, C. Schulz, *Low-pressure effective fluorescence lifetimes of single- and two-ring aromatics and their implication for model development*, 112. Bunsentagung, Karlsruhe, Germany, 2013, talk

6. S. Faust, M. Goschütz, S.A. Kaiser, T. Dreier, C. Schulz, *A comparison of different organic tracers for LIF imaging in gases: Photophysical properties and their im-*

pact on use in quantitative scalar imaging, 6th European Combustion Meeting, Lund, Sweden, 2013, conference paper and poster

List of abbreviations

CCD	Charge-coupled device
ϕ	Fluorescence quantum yield
ϕ_{fl}	Fluorescence quantum yield
ϕ_{rel}	Relative fluorescence quantum yield
FARLIF	Fuel/air-ratio LIF
h	Planck's constant
$\hbar$	Reduced Planck's constant ($h/2\pi$)
η	Detection efficiency
I	Intensity
I_{Laser}	Intensity of the incident laser beam
I_{LIF}	Intensity of the detected LIF signal
IC	Internal conversion
IC	Internal combustion
ISC	Intersystem crossing
k	Rate
k_{fl}	Fluorescence rate
k_{IC}	Rate of internal conversion
k_{ISC}	Rate of intersystem crossing
k_{nr}	Non-radiative rate
k_q	Quenching rate coefficient
k_{SV}	Stern-Volmer coefficient
k_{tot}	Total depopulation rate
λ	Wavelength
LIF	Laser-induced fluorescence
M	Transition dipole moment
MCP	Multi-channel plate
n	Number density (in m^{-3}) of molecules in the gas phase
p	total pressure
p_{O2}	O_2 partial pressure

σ	Absorption cross section (in cm^2)
S_{fl}	Fluorescence Signal
T	Temperature (K)
τ	Fluorescence lifetime
τ_{eff}	Effective fluorescence lifetime
τ_{rad}	Radiative lifetime
UV	Ultra violet region of light, $\lambda < 400$ nm
UV/Vis	Ultra violet / visible region of light, $\lambda < 700$ nm
VR	Vibrational relaxation
Ω	Detection angle

Acknowledgement

First I want to acknowledge Prof. Christof Schulz to give me the opportunity of doing my PhD thesis in his group. Thanks for insightful suggestions and ideas.

I want especially thank Dr. Thomas Dreier for all the guidance in the lab, for all his helpful scientific hints, for his patience, and for innumerable corrections while reading manuscripts for journal articles, conference abstracts, and posters. Thanks for the critical proof of my thesis.

Further I want to acknowledge my (current and former) colleagues of the diagnostics group: Thorsten Benzler, Omid Feroughi, Eugen Friesen, Daniel Greszik, Christian Hecht, Martin Leschowski, Jan Menser, Markus Röder, Hendrik Thering, Benjamin Witzel, Huinan Yang. Thanks for the nice working atmosphere and the fruitful discussions in many scientific and non-scientific problems. Thanks to Gabrielle Tea from IFPEN, Paris, for the prosperous collaboration when investigating naphthalene and the scientific exchange. Thanks to Martin Goschütz from the engine group for the good collaboration when testing the tracers in the injector experiment. Additional thanks to Dr. Mustapha Fikri and Siavash Zabeti from the kinetics group for their help and collaboration when exploring tracer pyrolysis.

Special thanks to Ludger Jerig, for his great engagement in doing lots of construction work for my cell(s), for his helpful hints how to survive in the university bureaucracy. Thanks to all the technical and administrative staff: Jörg Albrecht, Beate Endres, Barbara Graf, Dieter Hermanns, Birgit Nelius, Barbara Nota, Natascha Schlösser. Thank you for continuous help during my work.

Further thanks to the whole Schulz group, for the convenient atmosphere, for the nice celebrations and outings.

Additional thanks to the workshops of the university for their excellent work. Especially the mechanical workshop in Duisburg with Ulrich Visser as head and the electrical workshop of Ingo Kietzmann. Thanks for all the parts you produced for my experiment, thanks for Harald Landmann and Markus Loretan for doing so much helpful work in the lab for months. I also thank the optical workshop in Essen (Martin Jerman) for all the mirrors, windows etc. they produced for me.

Last but not least very many thanks to my girlfriend Sandra, for her love and support, for all the understanding during my work, especially when writing my thesis. Special thanks to the rest of my family, my parents and my brother, for their confidence in me, their continuous moral support.